

Hans Anders Faraasen

Power Electronic Converters for Efficient Operation of the Modular HVDC Generator for Offshore Wind Power

Comparison of DC-bus voltage balancing, IGBT
module losses and performance gains with the 3L-
NPC converter

Master's thesis in Energy and the Environment

Supervisor: Gilbert Bergna-Diaz

June 2020

Hans Anders Faraasen

Power Electronic Converters for Efficient Operation of the Modular HVDC Generator for Offshore Wind Power

Comparison of DC-bus voltage balancing, IGBT module losses and performance gains with the 3L-NPC converter

Master's thesis in Energy and the Environment
Supervisor: Gilbert Bergna-Diaz
June 2020

Norwegian University of Science and Technology
Faculty of Information Technology and Electrical Engineering
Department of Electric Power Engineering



Norwegian University of
Science and Technology

Summary

Offshore wind power is projected to have an exponential growth in the coming decades as the world needs affordable low-carbon and renewable energy resources. The modular High Voltage Direct Current (ModHVDC) generator is a new design for generator and electrical drive train, that proposes a transformer-less concept with a single conversion step to achieve 100 kV HVDC potential. By segmenting the stator of a permanent magnet synchronous generator, the machine forms multiple equivalent three-phase generators. Connecting these stator segments to series-connected power converters enables HVDC in a single conversion step. Thus, this technology aims at extending the use of HVDC in offshore wind power grids.

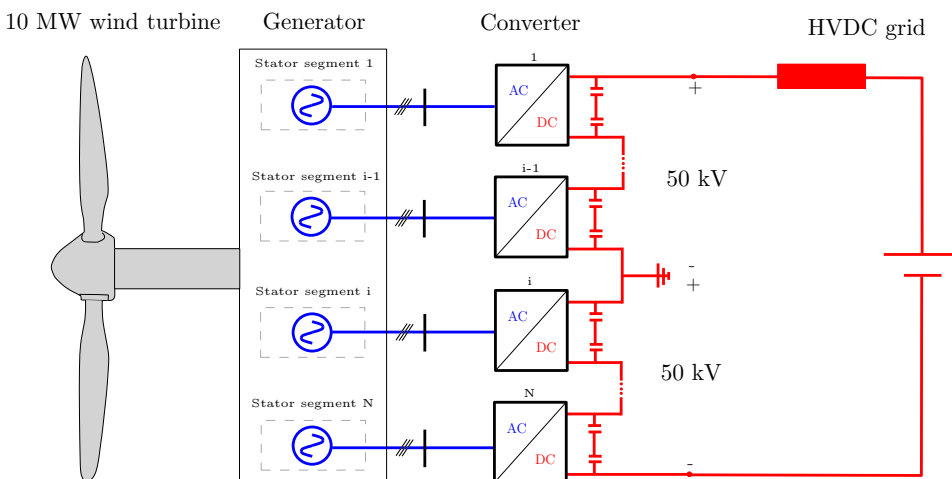


Figure 1: ModHVDC generator concept in this thesis.

This master thesis emphasizes the power electronic converters related to the ModHVDC machine. Special technical challenges arise due to the stator segmentation and multiple power converters. Adequate control methods are required for high performance and reliable operation. Additionally, the 100 kV DC-potential necessitates dedicated converters for safe and efficient operation. Research for energy-efficient and high performing power electronic converters was the focus for this thesis, where power converter performance, semiconductor losses and DC-bus voltage control methods was studied. The intention was to use the results for future lab-scale realization of the ModHVDC generator to increase the technical readiness level of the technology.

A comparison between a three-level neutral point clamp converter (3L-NPC) and a conventional two-level voltage source converter (2L-VSC) was carried out in terms of their performance. More precisely, performance was measured by studying the state variables

behaviour, voltage and current waveform, power quality, losses and efficiency for both converters when the wind turbine was subjected to various wind speeds. This was conducted in Simulink, where simulation setup, results and a summary are presented in chapter 5. The results showed that even though a stable operation was achieved with both converters, the 3L-NPC showed better power quality, reduced DC-link current ripple, lower losses and higher efficiency than the 2L-VSC. Based on the results, the 3L-NPC converter was concluded to be a suitable converter for use and future research for the ModHVDC generator.

Semiconductor losses with a 3.3, 4.5 and 6.5 kV industrially available IGBT module were calculated in chapter 4 by the use of analytical calculation loss models. The purpose of the study was to compare benefits of using multiple lower voltage rated modules or fewer higher voltage rated modules with both converters. The results showed that the 3.3 kV IGBT module had the lowest losses. Additionally, the calculation supported the simulation results as the 3L-NPC converter was more efficient than the 2L-VSC.

DC-bus voltage control methods were studied in chapter 3 and concerns balancing the DC-bus voltages of all converters. Both the challenge and potential solutions for control strategies were presented. Eighth generator/converter modules were assigned with normal distributed parameters for simulating a natural voltage variation between modules in a full-scale application. The results show that the alternatives for having identical DC-bus voltages are either accepting overloading of some modules or lower the power output of each module to the module with lowest output power. For this specific case, the former led to a current overloading of 0.048 pu (8 A), while the latter resulted in a power reduction of 4.5 %, which could accumulate to 1.3 GWh/year for a 10 MW offshore wind turbine.

Sammendrag

Offshore vindkraft spås å ha en eksponentiell vekst de neste tiårene da verden trenger kostnadseffektiv og fornybar energi. Den modulære HVDC (ModHVDC) generatoren er et nytt design for å oppnå 100 kV HVDC i ett omformingssteg uten transformatorer. Ved å segmentere statoren til en permanentmagnetgenerator blir hvert statorsegment å regne som en trefase generator. Ved å koble segmentene til seriekoblede kraftomformere muliggjøres HVDC i ett omformingssteg. Dermed tar teknologies sikte på å utvide bruken av HVDC i offshore vindkraft.

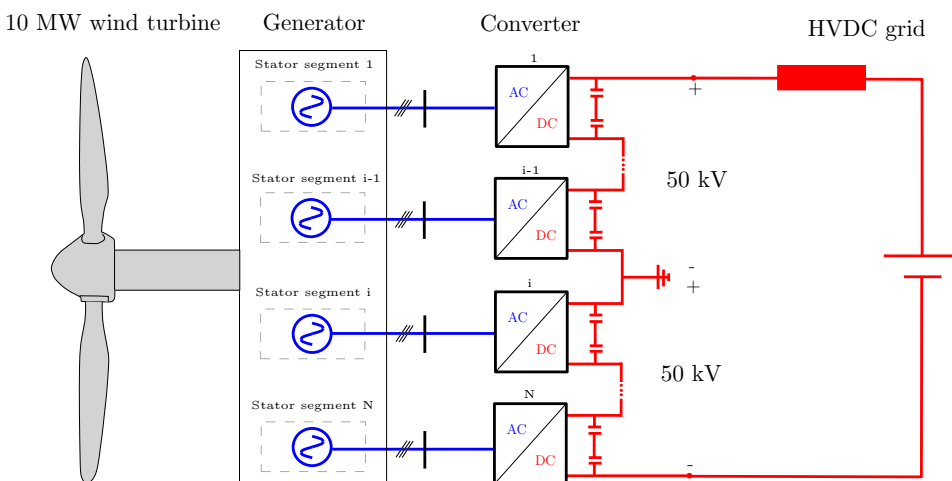


Figure 2: ModHVDC generator konseptet i denne oppgaven.

I oppgaven har teknologien vært konseptualisert i en 10 MW vindturbin. Kraftomformer(en) har vært fokusområdet i vindturbinssystemet. To forskjellige omformeres ytelse i applikasjonen har vært sammenlignet, tap tilknyttet halvlederne i omformerne og kontrollmetoder av omformerne har vært studert. De neste tre avsnittene oppsummerer metode og resultat tilhørende hvert punkt.

Ytelse ble studert ved å sammenligne en “three-level neutral point clamped” (3L-NPC) omformer og en “two-level voltage source converter” (2L-VSC). Ytelse ble målt ved å studere tilstandsvariablene i systemet, kurvene til spenning og strøm og kraftkvaliteten i tillegg til tap og effektivitet for begge omformere for en rekke forskjellige vindhastigheter. Dette ble gjennomført i simuleringsprogrammet Simulink hvor tilhørende oppsett og resultater gis i kapittel 5. Resultatene viste at systemet var stabilt for begge omformerne. 3L-NPC-omformerer viste bedre kraftkvalitet, redusert variasjon i DC-link strøm, lavere tap og høyere effektivitet sammenlignet med 2L-VSC-omformerer. Basert på resultatene

ble det konkludert med at 3L-NPC-omformerer utkonkurrerer sin motpart og det er anbefalt at førstnevnte omformer brukes i videre studier eller praktiske forsøk i istedenfor sistnevnte.

Tap i 3.3, 4.5 og 6.5 kV industrielt tilgjengelige IGBT moduler ble beregnet i kapittel 4 ved bruk av analytiske beregningsmodeller. Formålet var å studere og sammenligne forskjellene mellom å bruke flere 3.3 kV moduler, få 6.5 kV moduler eller et kompromiss ved å bruke 4.5 kV moduler. Resultatene viste at 3.3 kV modulen hadde de laveste tapene. Alle modulene ble evaluert i begge omformerne og resultatene viste at 3L-NPC-omformerer var mer effektiv enn sin motpart i alle tilfeller, hvilket simuleringsresultatet i kapittel 5 støtter.

Kontroll av DC-busspenningene med tilhørende utfordringer og løsninger ble presentert i kapittel 3. En casestudie med åtte generator/omformer moduler med normalfordelte parametere ble brukt som utgangspunkt for å studere kontrollmetodene. Resultatene viser at man enten må akseptere overbelastning av moduler eller senke effekten fra noen moduler for å ha identiske DC-busspenninger. Overbelastning medførte at én modul ble belastet med 0.048 pu (8 A) over nominell verdi, mens kraftreduksjonen var på 4.5 %, hvilket kan tilsvare 1.3 GWh/år for en 10 MW offshore vindturbin.

Preface

This master thesis concludes my six year long journey in academia. An investment in education, which contains three years in Bergen, one year as technical student at CERN in Switzerland and two years in Trondheim. I am very proud of completing this journey and grateful for all the ways it has enriched me.

The research project I have been a part of for the last year, has allowed me to study what I wanted for my master thesis; power electronic converters, permanent magnet synchronous generators and wind turbines as a system. I would like to thank my co-supervisor Pål Keim Olsen for inviting me to be a part of this project in fall semester 2019 and for guidance. I would also like to thank my supervisor Gilbert Bergna-Diaz. Already in May 2019 Gilbert prepared me for this dissertation and have guided me since. To Gilbert, thank you for your support, your positive attitude, the rewarding technical discussions and all the time you have guided me. I do not take all the hours for granted, I was more than lucky with my supervisor.

A constant in my life for the last seven years and the person that led me to finding my inner motivation for starting this journey is my girlfriend Hanna. To you, without your love, support, the great life we share and your mysterious ways of making me wanting to be the best version of myself, this would never be possible. From the bottom of my heart, thank you.

The 30th of May was the happiest day of my life, as I became a farther to my first born daughter. I cannot wait to shift all my focus from power electronic converters, semiconductors and academic methods to this wonderful child. I dedicate this thesis my girls, Hanna and Ellinor.

Hans Anders Faraasen
Trondheim, 5th of June 2020

Table of Contents

Summary	i
Sammendrag	iii
Preface	v
Table of Contents	ix
List of Tables	xi
List of Figures	xiv
1 Introduction	1
1.1 Offshore wind power	1
1.1.1 State of the industry and outlook on its future	1
1.1.2 Required innovations	1
1.1.3 Offshore wind farm connection technologies	2
1.2 The modular HVDC generator	3
1.2.1 The concept and its advantages in offshore wind power	3
1.2.2 ModHVDC generator in previous research	4
1.3 Research motivation	5
1.4 Research objectives and question	7
1.5 Limitation of scope	8
1.6 Thesis layout	9
2 Theoretical background and system modeling	10
2.1 The 2L-VSC	10
2.2 The 3L-NPC converter	12
2.2.1 DC capacitor voltage balancing	14
2.3 Description of ModHVDC generator	14
2.3.1 Modeling of a segmented PMSG	15

2.3.2	Simulation model in Simulink	19
2.4	Description of ModHVDC converter system	19
2.4.1	Required series-connection of semiconductors	20
2.5	Wind turbine model	21
2.5.1	Turbine rotor model	23
2.5.2	Maximum power point tracking	23
2.6	Wind speed model	24
2.7	Control system	26
2.8	HVDC grid	28
3	DC-bus voltage controller analysis	29
3.1	Steady state analysis	29
3.2	DC-bus voltage controller regulation capability and challenges	30
3.3	Case study	32
3.3.1	Voltage distribution without balancing current	33
3.3.2	Balancing current with no constraint and no power derating	33
3.3.3	Balancing current with constraints and power derating	34
3.3.4	Comparison of annual energy output	35
3.4	Outcome of case study	36
4	Converter and IGBT module loss calculation	38
4.1	Introduction	38
4.2	Method	39
4.2.1	Power devices	39
4.2.2	Series-connection	40
4.2.3	Converter switching frequency	40
4.2.4	IGBT and diode junction temperatures	40
4.2.5	Turbine operation	40
4.2.6	Measurement parameters	41
4.2.7	Analytical models	41
4.3	Results	44
4.3.1	2L-VSC	44
4.3.2	3L-NPC	46
4.4	Outcome of calculation	49
5	System simulation	50
5.1	Simulation setup	50
5.2	Simulation results	52
5.2.1	Comparison of state variables	52
5.2.2	Waveform comparison	53
5.2.3	Comparison of power quality	56
5.2.4	Converter loss comparison	57
5.2.5	DC-bus voltage controller strategies	60
5.3	Summary of simulation results	62

6	Discussion	64
6.1	Selection of power converters	64
6.2	DC-bus voltage controller analysis	65
6.3	Converter and IGBT module loss calculation	65
6.4	System simulation	66
7	Conclusion	68
8	Future work	70
A	Appendix	77
A.1	Per unit system	77
A.1.1	Base values	77
A.1.2	Per unit values	78
A.2	Chapter 2	79
A.2.1	PMSG	79
A.2.2	PMSG voltage equations in per unit	85
A.2.3	Segmented PMSG Simulink model	85
A.2.4	Tuning of controllers	93
A.3	Chapter 4	96
A.3.1	Analytical calculation models	96
A.3.2	Total losses and system efficiency with 16 segments	98
A.4	Chapter 5	99
A.4.1	Simulation setup	99
A.4.2	Simulation model	100
A.4.3	Comparison of analytical and simulation model results	106
A.4.4	Results	108

List of Tables

2.1	Possible states, voltages and device conduction.	12
2.2	Possible states, voltages and device conduction.	12
2.3	Wind model characteristics.	25
2.4	Wind speed distribution.	25
3.1	Parameter nominal/expected per unit values and standard deviation.	32
3.2	Module parametrization with normal-distributed parameters.	33
3.3	Voltage distribution at various wind speeds when using normal distributed parameters.	33
3.4	Balancing current in per unit for achieving symmetrical voltage distribution.	34
3.5	Balancing currents for achieving symmetrical voltage distribution at rated wind speed and above.	35
3.6	Power reduction to achieve symmetrical voltages.	35
3.7	Energy reduction to achieve symmetrical voltages.	36
4.1	Studied IGBT modules.	39
4.2	Required series-connection of devices with 8 segments ($N = 8$) and 1 redundant modules ($z = 1$).	40
4.3	Required series-connection of devices with 16 segments ($N = 16$) and 2 redundant modules ($z = 2$).	40
4.4	Junction temperatures in 2L-VSC loss analysis.	40
4.5	Junction temperatures in 3L-NPC converter loss analysis.	40
4.6	IGBT and diode percentage contribution to total switching losses.	44
4.7	Conduction losses percentage distribution.	46
4.8	Converter system efficiency η tabular results.	46
4.9	Device switching loss relative contribution to total switching losses.	47
4.10	Conduction losses percentage distribution.	47
4.11	Converter system efficiency η tabular results.	49
5.1	DC-link current ripple $\Delta i_{dc-link}$ in per unit for all wind speeds and both converters.	56

5.2	Total losses and efficiency with both converters.	58
5.3	Constants for approximation of total losses as a function of wind speed and associated coefficient of determination (R^2).	59
5.4	Resulting converter weighted average efficiency.	60
5.5	Mean of DC-link power in time interval $50 \leq t \leq 60$	62
A.1	Per unit system: AC quantities	77
A.2	Per unit system: DC quantities	78
A.3	Per unit system: Mechanical quantities	78
A.4	Difference in dq-axis current from Simulink's PMSM to segmented PMSG.	92
A.5	Current controller PI-controller constants.	94
A.6	Speed controller PI-controller constants.	94
A.7	DC-bus voltage controller PI-controller constants.	95
A.8	Table of symbols.	96
A.9	Input data to analytical models.	97
A.10	IGBT module specific input data to analytical model.	97
A.11	IGBT modules series-connection and device voltage for $N = 8$ segments.	98
A.12	IGBT modules series-connection and device voltage for $N = 16$ segments.	98
A.13	Resulting efficiency with 16 segments.	98
A.14	Wind turbine model parameters.	99
A.15	Generator segment parameters.	99
A.16	Converter parameters.	99
A.17	HVDC grid parameters.	99
A.18	Mechanical time constant.	100
A.19	Simulation and solver parameters.	100
A.20	Expected voltages for various wind speeds with $psi_1 = 1.05$ and $psi_2 = 0.95$	100
A.21	IGBT module 5SNG 0250P330300 input data to analytical model.	106
A.22	Comparison of switching and conduction losses with the analytical and simulation model when using a 2L-VSC.	107
A.23	Comparison of total losses and efficiency with the analytical and simulation model when using a 2L-VSC.	107
A.24	Comparison of switching losses with the analytical and simulation model when using a 3L-NPC converter.	107
A.25	Comparison of conduction losses with the analytical and simulation model when using a 3L-NPC converter.	107
A.26	Comparison of total losses and efficiency with the analytical and simulation model when using a 3L-NPC converter.	108
A.27	Data input for calculation of average efficiency.	108

List of Figures

1	ModHVDC generator concept in this thesis.	i
2	ModHVDC generator konseptet i denne oppgaven.	iii
1.1	HVAC internally in windfarm and to onshore grid.	2
1.2	HVAC internally in windfarm and HVDC to onshore grid.	3
1.3	Possible offshore wind farm configuration with the use of the ModHVDC generator.	4
1.4	Principle sketch of the ModHVDC generator concept.	4
1.5	ModHVDC in previous research [1].	5
2.1	Main blocks in system.	10
2.2	The 2L-VSC topology.	11
2.3	SPWM modulation of a 2L-VSC converter.	11
2.4	Conduction pattern in a phase-leg for a 2L-VSC.	11
2.5	The 3L-NPC converter topology.	12
2.6	Conduction pattern in a phase-leg for a 3L-NPC converter.	13
2.7	Modulation of a 3L-NPC converter.	13
2.8	ModHVDC generator exemplified by a four-segmented machine with associated converters.	15
2.9	ModHVDC screening strategy [1, Fig. 3.2].	15
2.10	Wind turbine with and without gearbox in drivetrain [2].	17
2.11	ModHVDC and converter system topology.	20
2.12	Series-connection of semiconductors exemplified in a 2L-VSC.	20
2.13	The four operational regions of a wind turbine. Inspired by [3].	22
2.14	Principle sketch of the implemented TSR MPPT-strategy.	24
2.15	Discretized wind speed distribution.	25
2.16	Control system.	26
2.17	Current controller structure.	27
2.18	Speed controller structure.	27
2.19	DC-bus voltage balancing controller structure.	28
2.20	SPWM and capacitor voltage balancing controller structure.	28

2.21	HVDC grid model.	28
3.1	Feasible region of balancing current.	31
3.2	Balancing currents as a function of wind speed.	34
4.1	Classification of IGBT modules losses. Green boxes indicates considered losses, red indicate neglected losses.	38
4.2	Hierarchy of power losses in an IGBT module.	39
4.3	linearization of typical on-state output characteristic of IGBT and typical diode forward characteristic of ABB 5SNA 0400J650100 IGBT [4].	43
4.4	IGBT $P_{sw(T)}$ (left figure) and diode $P_{sw(D)}$ (right figure) switching losses for the IGBT modules as a function of frequency.	45
4.5	IGBT $P_{con(T)}$ and diode $P_{con(D)}$ conduction losses for the three modules.	45
4.6	Total power losses $P_{tot,2L}$ (left figure) and efficiency η (right figure) as a function of switching frequency.	46
4.7	Switching losses for the various devices as a function of switching frequency.	47
4.8	Conduction losses for the various devices.	48
4.9	Total power losses $P_{tot,3L}$ (left figure) and efficiency η (right figure) as a function of switching frequency.	48
5.1	Simulation setup.	50
5.2	Wind speed input.	51
5.3	State variables with 3L-NPC converter.	52
5.4	State variables with 2L-VSC.	53
5.5	Steady state phase current i_{abc} with the 3L-NPC converter.	54
5.6	Steady state phase current i_{abc} with the 2L-VSC.	54
5.7	Steady state line-to-line voltage v_{ab} with the 3L-NPC converter.	55
5.8	Steady state line-to-line voltage v_{ab} with the 2L-VSC.	55
5.9	DC-link voltage and current for both converters. Full simulation course.	56
5.10	THD in phase current and line-to-line voltage for both converters and various wind speeds.	57
5.11	Switching and conduction losses in the 3L-NPC converter and 2L-VSC.	57
5.12	Semiconductor junction temperatures for both converters.	58
5.13	Efficiency as a function of wind speed for both converters.	59
5.14	The AC-side input power, converter efficiency and the discretized wind speed distribution in turbine operation region 2 and 3.	60
5.15	Q-axis currents, DC-bus voltages and DC-link power for three DC-bus voltage controller strategies.	61
A.1	Left: surface mounted magnets. Right: built-in magnets [5].	79
A.2	Illustration of a round rotor PMSM showing the dq axis in a rotating reference frame	80
A.3	Park transform. Stationary abc-reference frame converted to synchronously rotating dq-reference frame. Inspired by [6, p. 143].	82
A.4	Electrical model block.	86
A.5	Content of electrical model.	86

A.6	Dynamics block and content.	87
A.7	PMSG segment physical model that is connected to the power converter. .	87
A.8	Mechanical model block.	87
A.9	Mechanical model block.	88
A.10	Current references.	89
A.11	q-axis current for custom made PMSG compared to Simulink's original model of a PMSM.	90
A.12	d-axis current for custom made PMSG compared to Simulink's original model of a PMSM.	91
A.13	Shaft speed ω_r for custom made PMSG compared to Simulink's original model of a PMSM.	92
A.14	Current controller, PWM and plant response.	93
A.15	Speed controller system for tuning.	94
A.16	Simulation model implemented in phase-leg A of a 3L-NPC converter. . .	101
A.17	IGBT module-model block content.	102
A.18	Internal content of the loss calculation unit.	103
A.19	Semiconductor junction temperatures for both converters.	103
A.20	Thermal equivalent circuit.	104
A.22	Heat sink block.	104
A.21	Semiconductor junction temperatures for both converters.	105
A.23	Heat sink block.	105

Nomenclature

Acronyms

2L-VSC	Two-level Voltage Source Converter
3L-ANPC	Three-level Active Neutral Point Clamped
3L-NPC	Three-level Neutral Point Clamped
HVAC	High Voltage Alternating Current
HVDC	High Voltage Direct Current
IEA	International Energy Agency
IGBT	Insulated Gate Bipolar Transistor
IGCT	Insulated Gate Commutated Thyristor
MMC	Modular Multilevel Converter
ModHVDC	Modular High Voltage Direct Current
MPPT	Maximum Power Point Tracking
PMSG	Permanent Magnet Synchronous Generator
PMSM	Permanent Magnet Synchronous Motor
pu	Per Unit
SDS	Sustainable Development Scenario
SPWM	Sinusoidal Pulse Width Modulation
THD	Total Harmonic Distortion
TSR	Tip Speed Ratio
VSC	Voltage Source Converter

Introduction

1.1 Offshore wind power

1.1.1 State of the industry and outlook on its future

The global energy sector is not on track to meet the energy-related requirements of United Nations sustainable development goals. This relates to universal access to energy, health impact of air pollution and climate changes. For the sector to be sustainable, the International Energy Agency (IEA) Sustainable Development Scenario (SDS) proposes a pathway for the energy sector and policy makers for a sustainable and clean energy sector in the coming decades [7].

Offshore wind power is in the SDS predicted to contribute to global energy marked decarbonisation and be the leading source of electricity in Europe [8, p. 3]. The SDS highlights that the global energy market needs an exponential growth in offshore wind capacity. It is predicted that global offshore wind capacity will increase from 23 GW in 2018 to 560 GW in 2040. This will lead to a 5% share of global electricity supply [8, p. 27]. The cumulative investments of that vision equates to roughly \$60 billion of annual investments per year on average [8, p. 29].

However, present stated policies are not as ambitious as the requirements set by the SDS [9]. Additional technical and political efforts are required to further accelerate offshore wind power. Cost reductions, technology improvements and rapid deployment are some of the factors addressed by the IEA [9]. The next chapter is dedicated to exploring one of the technical innovation gaps that IEA addresses.

1.1.2 Required innovations

One of the three innovations gaps that IEA addresses is “reducing cost and risk of transmission and distribution of electricity from offshore wind” [10]. Reducing the volume of

High Voltage Alternating Current (HVAC) infrastructure and introduce High Voltage Direct Current (HVDC) technology both internally in wind farms¹ and from offshore wind farms to onshore grid is of priority to fill this gap. The importance is further reinforced by the trend of moving towards deeper waters and further from shore [8, p. 75], where HVDC is seen as an enabling technology [10]. Additionally, the development of wind power generator ratings beyond 10 MW will decrease future turbine share of capital [9]. The importance reducing the cost related to energy transmission and wind farm internal cabling becomes more important.

1.1.3 Offshore wind farm connection technologies

The innovation gaps highlights the importance of HVDC in future offshore wind power grids. In this chapter, a brief introduction to two typical transmission technologies are presented.

Various types of network configurations and technologies exist for connecting an offshore wind farm to onshore grid. Distinctive features between the typical and proposed configurations are series or parallel connection of wind turbines and HVAC or HVDC internally in wind farm and connection from offshore wind farm to onshore grid [11, p. 768]. Parallel connection of wind turbines are at present most widely use [11, p. 769]. The use of HVAC or HVDC for power transfer depends on multiple factors, but the transmission distance can be decisive. AC transmission has a cost advantage over short distances, while HVDC are preferred for transmission links of roughly 100 km or longer [8, Fig. 17].

HVAC internally in wind farm and to onshore grid

Figure 1.1 shows an example of HVAC for both internal wind farm interconnection and transmission to shore. The output of the power converters are connected to a step-up transformer. The output of the transformer are fed further by cable to an wind farm substation. This collection point has another step-up transformer to achieve a suitable voltage level for larger power transfer over longer distance. The power is transmitted to the onshore grid by a submarine cable [11, Ch. IX.B].

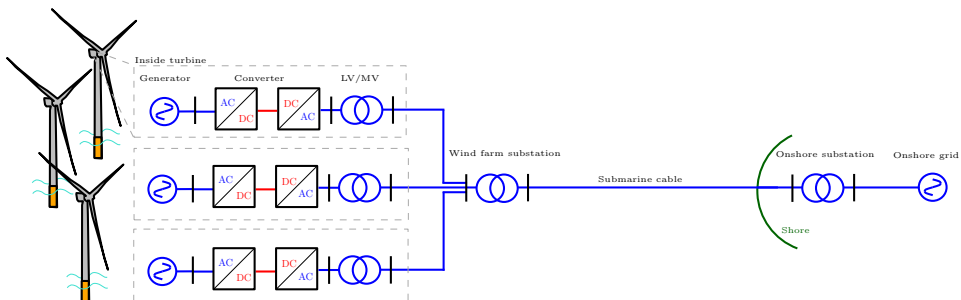


Figure 1.1: HVAC internally in windfarm and to onshore grid.

¹Group(s) of wind turbines

HVAC internally in wind farm and HVDC to onshore grid

In Figure 1.2 HVDC is used in the transmission link to the onshore grid. The wind farm substation is now an AC/DC rectifier station, where the incoming AC voltage is stepped up and rectified. The power onshore substation inverts power back to AC and supply power to the grid.

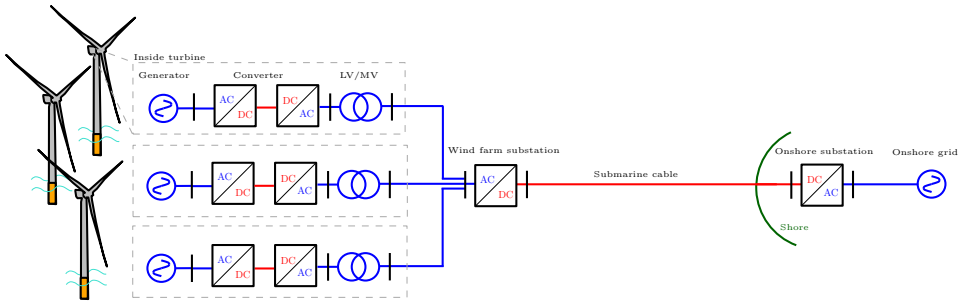


Figure 1.2: HVAC internally in windfarm and HVDC to onshore grid.

Both the onshore and offshore converter station are large high voltage and high power converters. Numerous technologies for these converters exist, but the Modular Multilevel Converters (MMC) Voltage Source Converter (VSC) are popular. As an example, the Dutch-German transmission system operator TenneT uses the MMC for HVDC-transmission in many of their projects such as the BorWin Gamma platform [12, Tab. 7.1]. This converter has a voltage rating of 320 kV and a power rating of 800 MW.

1.2 The modular HVDC generator

1.2.1 The concept and its advantages in offshore wind power

Common for the configurations seen in Figure 1.1 and Figure 1.2 are multiple AC/DC and voltage conversion stages. The modular HVDC (ModHVDC) generator is a new design for generator and electrical drive train, that proposes a transformer-less concept with a single conversion stage to achieve HVDC potential in wind turbine terminals. This can be an enabling technology for extending the use of HVDC in offshore wind power and hence it addresses the innovation gap in chapter 1.1.2. Figure 1.3 shows an example of how such an HVDC network configuration might be.

The claimed advantages of the ModHVDC generator are reduction of offshore HVAC infrastructure, conversion stages and components. This can again augment reliability and efficiency and ultimately reduce the cost of offshore wind power [13],[14],[15]. For realizing HVDC in a single transformer-less conversion step, a stator segmented permanent magnet synchronous generator (PMSG) is proposed [13]. Each stator segment can be regarded as an equivalent three-phase generator. A power converter is dedicated to each segment and the converters are series-connected on the DC-side for facilitating HVDC in

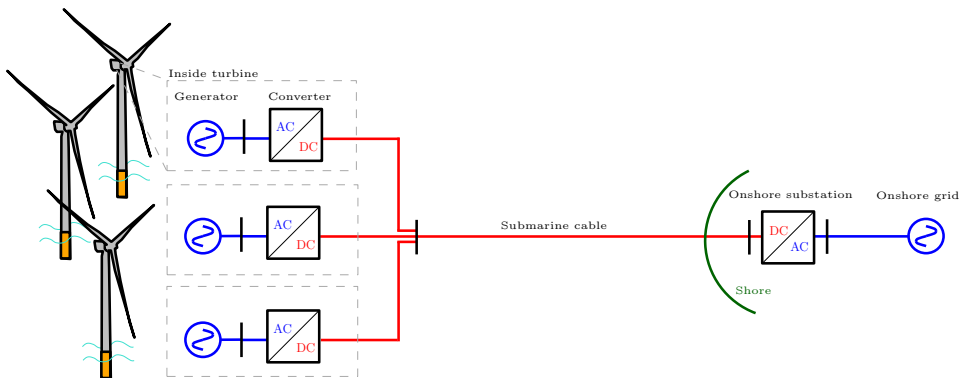


Figure 1.3: Possible offshore wind farm configuration with the use of the ModHVDC generator.

a single conversion step. DC-side ground is placed in the middle of the DC-link. Figure 1.4 show the principal configuration for N number of generator/converters.

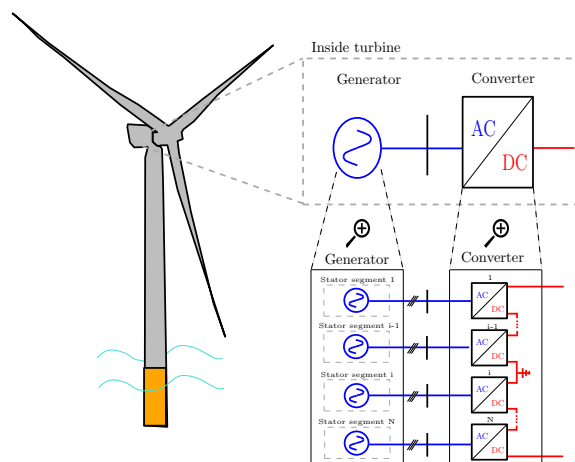


Figure 1.4: Principle sketch of the ModHVDC generator concept.

1.2.2 ModHVDC generator in previous research

The generator has previously been conceptualized in a doctoral thesis from 2012 [1] as a 10 MW offshore wind turbine with a direct drive² mechanical system and a nine-segment generator/converter configuration that outputs 100 kV DC on the DC-link. Figure 1.5 illustrate that system.

Each generator segment had a rated voltage and current at roughly 6.5 kV and 100 A. The power converter was the conventional two-level voltage source converter (2L-VSC).

²Gear-less mechanical coupling of turbine rotor and generator shaft.

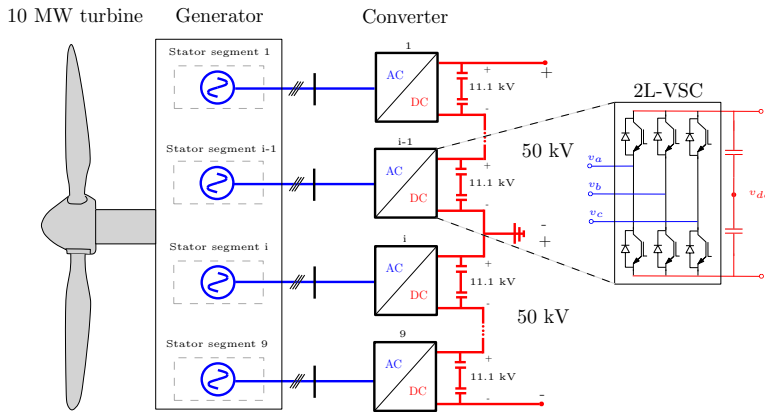


Figure 1.5: ModHVDC in previous research [1].

The thesis provided a detailed system description, a control system synthesis and presented both simulation results and experimental results that proved the concept of the ModHVDC generator. This thesis was an important foundation for the specialization project conducted fall-semester 2019.

In the specialization project [16], two quantitative analyses and one qualitative analysis were conducted. The two quantitative analyses was a platform to obtain a fundamental system understanding. The first was a study of a conventional single segment PMSG and a single 2L-VSC in a 1.25 MW wind turbine application. The second was a four-segment generator/converter model where the machine was simplified to a stiff AC grid source equivalent. The goal was to study AC and DC voltage distributions in the system. In the qualitative analysis, a power converter review was conducted. The review gave insight to what type of converter topology could be suitable for this offshore wind power application. Power electronic converter topology and control was the focus of the specialization project and will be further studied in this thesis.

1.3 Research motivation

Common for both works presented in chapter 1.2.2 is the 2L-VSC. The benefits of using multilevel converters in an application like the ModHVDC generator was explored in the specialization project converter review. The fundamental motivation for using multilevel converters in this application is related to the 100 kV HVDC potential. By using a multilevel converter instead of the 2L-VSC, a reduction of semiconductor voltage stress, reduced need for series-connection of semiconductors, higher converter efficiency and improved power quality might be achieved [17]. However its can come with a cost of more complex circuitry and more advanced control [18, Tab. 1].

The considered multilevel converters in [16] was a five-level MMC and the three-level neutral point clamped (3L-NPC) converter. Additionally, the Vienna rectifier was investi-

gated as an alternative three-level converter. The MMC was considered to be too complex and was not recommended for future research in this thesis. The simplicity offered by the Vienna rectifier was tempting for future research and therefor recommended. However, in hindsight the analysis is considered to be limited and the benefits of the 3L-NPC converter were underestimated. In addition to the former mentioned benefits, an important motivational factor for studying the 3L-NPC converter relates to an industrial aspect and feasibility for future laboratory implementation. The 3L-NPC converter is the most commercialized multilevel converter and is predicted to still be widely used as a high power medium voltage converter in future wind power industry [19, Ch. 8.1]. It might be a realistic converter to be used in e.g. a lab-scale set-up and later stages in the ModHVDC research project. Therefore, the scientific contribution of a 3L-NPC converter performance in this application is seen as more valuable than compared to the Vienna rectifier, which is not well known in wind power industry [18]. In short, the motivation for studying the 3L-NPC converter is the combination of multilevel converter benefits, low circuit and control complexity in addition to wide industrial use and availability.

One of the recommended topics for future research in [1, Ch. 7.2] was a converter loss analysis and investigation of AC and DC-side ratings to converters and semiconductors. The latter was addressed in the specialization project report by calculating required series-connection of semiconductors in a converter for various system configurations [16, Ch. 4]. This is coupled with a loss analysis since the losses relates to number semiconductor devices, AC-side current, DC-side voltage and type of semiconductor also influence losses. It was suggested in [16] as future work to investigate losses in two ways.

1. Compare losses for a chosen converter and benchmark results to a 2L-VSC
2. Compare losses of various voltage rated Insulated Gate Bipolar Transistor (IGBT) modules

Comparing losses in various converters can be one of the indicators to answering the question of what is a suitable converter for the ModHVDC generator concept. Using the 2L-VSC as a reference is justified because of the use in previous research and its wide industrial use. Series-connection of IGBT modules might be required due to the 100 kV DC. Comparing various voltage rated IGBT modules might give insight to what is most beneficial in terms of losses; series-connecting multiple lower voltage rated modules or using fewer higher voltage rated modules. This open question is investigated in this thesis. The combination of these two loss analyses can be valuable for future system design of power converter.

Another design aspect of the ModHVDC generator that is linked to losses and system efficiency relates to a control method. The series-connection of power converters require a DC-bus voltage controller for controlling the DC-bus voltages of each converter. One control strategy is to keep all bus voltages equal, but that might imply output power reduction in some generator/converter modules. This is not desirable as it might compromise claimed benefits of high system efficiency. This was to some extend researched in [1], but will be researched again in this thesis as more research is needed. This relates to e.g.

possible voltage deviations and use of a wind speed distribution function to generalize differences in energy output with various control strategies.

In a summary, this thesis will extend the previous research by studying the ModHVDC system with a 3L-NPC converter, where its performance is benchmarked to a 2L-VSC. Additionally, a loss comparison between converters, semiconductors and DC-bus voltage control methods will be conducted.

1.4 Research objectives and question

This thesis emphasizes the power electronics converter and converter control aspect of the ModHVDC generator in an offshore wind turbine. There are multiple research objectives:

1. Develop a simulation model in Simulink environment that models wind speed, a wind turbine, the ModHVDC generator with multiple stator segments, power converter, associated control system and HVDC grid.
2. Investigate various DC-bus voltage control methods and associated effects on generator/converter modules and turbine energy output.
3. Perform a loss calculation of the 3L-NPC converter and 2L-VSC. Three different IGBT modules are used in both converters for comparison. Select a suitable module for use in the simulation model and further research.
4. Conduct a performance analysis in the simulation model to observe how the 3L-NPC converter perform for various wind speeds in this application. Benchmark the results to the 2L-VSC.

Objective one is a planned extension of the specialization project. To the best of the authors knowledge, a Simulink model of the stator segmented machine is not available. A custom made model will be developed, validated and used for relevant purposes. The simulation model is essential for conducting the performance analysis, validate analytical results and provide results that indicate stable and safe ModHVDC operation with the 3L-NPC converter.

In the second objective, DC-bus voltage control methods will be addressed. An analysis of the challenge, possible solutions and the effect of these solutions will be presented and compared.

Objective three is performed as a calculation of converter and semiconductor losses. The two converters and three IGBT modules gives six combinations. Analytical loss models are used to estimate power losses for all combinations. Comparison of the six alternatives are performed and based on the results, a suitable IGBT module is chosen for further use in the simulation model. Here, losses will also be evaluated, but differently than in this objective, as wind speed range are extended and converter switching frequency kept constant.

The fourth research objective is related to the performance of the 3L-NPC converter compared to a 2L-VSC. Performance will be measured by studying system state variables, voltage and current waveforms, power quality of AC-side voltage and current in addition to converter losses and efficiency - all for various wind speeds. Analysing and evaluating the state variables is used as an indicator of system stability and proof of concept. The power quality of AC-side current and line-to-line voltage is of interest for potential future inclusion of filters and is a relevant performance indicator. Converter losses and efficiency is an important performance indicator for securing high system efficiency.

Based on the research objectives, two research questions are consequently formed. The first research questions relates to the 3L-NPC converter. The converter is extensively used in wind power industry and might offer many benefits to this application. The converter is considered to offer a suitable trade-off between the technical advantages of multilevel converters and the increased complexity of such converters. The research question can be formulated as:

How does the 3L-NPC converter compare to a conventional 2L-VSC in terms of performance in the ModHVDC application and is it a suitable converter?

The second research question relates to the control method:

What are the alternatives for balancing the DC-bus voltages and what are their consequence?

1.5 Limitation of scope

The research objectives shows that the system in question consist of multiple blocks, each a wide and complex field of research. In order to limit the extend of the thesis, certain limitations must be set.

The following list show the limitations.

- The work is limited to a single wind turbine.
- All analyses will be conducted for normal operation with no faults and a balanced network.
- The wind speed is ideal and deterministic, i.e. no wind gust and stochastic behaviour will be studied.
- Turbine operation is constrained to turbine operational region 2 in the simulation model. If operation in region 3 is evaluated, it is treated identical to turbine operation at rated wind speed.
- The thesis limits selection of semiconductors to industrially available IGBT module packages from ABB.
- Modulation strategies for both converters are limited to conventional sinusoidal pulse width modulation (SPWM).

-
- All loss/efficiency calculations are limited to the losses related to semiconductors and control methods.
 - Evaluation of power quality is limited to harmonic content of AC-side line-to-line voltage and current.

1.6 Thesis layout

The following chapter descriptions presents the layout of this thesis.

Chapter 1: Introduction to offshore wind power, ModHVDC generator, ModHVDC previous research, motivation for research in this thesis, research objectives and questions.

Chapter 2: Theoretical background and introduction to system modelling. This includes wind speed modelling, wind turbine model, ModHVDC generator and converter system introduction, modeling of segmented PMSG, introduction to 2L-VSC and 3L-NPC converter in addition to an HVDC grid model.

Chapter 3: Analysis of DC-bus voltage controller strategies. Linked to research objective two.

Chapter 4: Calculation of losses with the six converter-IGBT module combinations. Relates to research objective three.

Chapter 5: Simulation chapter dedicated to performance evaluation of 3L-NPC converter and 2L-VSC in ModHVDC application. The chapter is dedicated for research objective four.

Chapter 6: Discussion of used methods and obtained results.

Chapter 7: Conclusion to research objectives and questions

Chapter 8: Proposed future work that can extend this thesis.

Appendix: Required attachments that is excluded from the other chapters for compactness.

Theoretical background and system modeling

The system in question is presented in a block diagram in Figure 2.1. The following sub-chapters will block-by-block explain the theoretical background and modeling of these blocks.

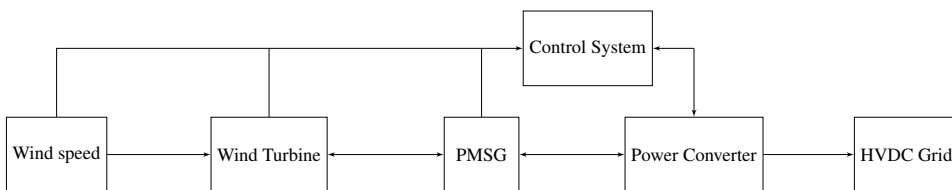


Figure 2.1: Main blocks in system.

2.1 The 2L-VSC

The 2L-VSC is a fully controllable converter, well established in multiple applications. The converter topology can be seen in Figure 2.2.

The converter consist of six IGBTs and anti-parallel diodes. Two identical capacitors splits the DC-bus voltage and forms a neutral-point N. The term “two-level” relates to the operation of the converter and number of possible states. This converter can take on two states as given in Table 4.4. The table uses the notation for phase a, but are valid for all three phases.

Figure 2.3 show SPWM modulation technique of a 2L-VSC. There are two control signals, the triangular signal v_{tri} and the control signal v_{ctrl} . If the control signal is greater than

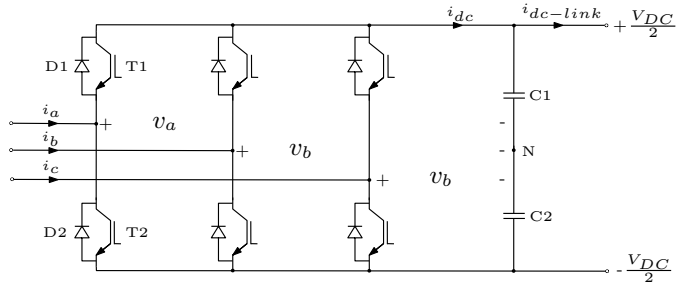


Figure 2.2: The 2L-VSC topology.

the triangular signal, the state is 1, else -1. The relationship between the amplitude of the control signals are known as the modulation amplitude index m_a [20, Ch. 8].

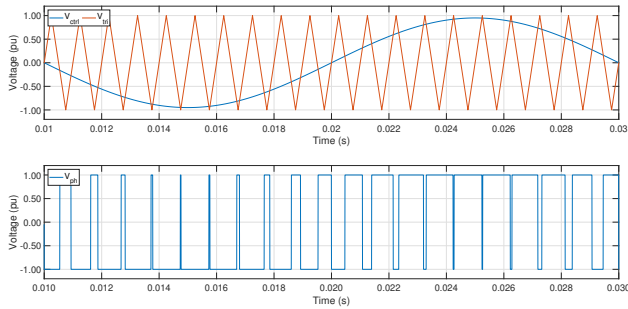


Figure 2.3: SPWM modulation of a 2L-VSC converter.

The conduction pattern depends on state and current direction. The devices T1-D2 and T2-D1 forms pairs that conducts depending on current direction. Which of the devices within the pair that conducts depends on the state. Figure 2.4 illustrate the conduction pattern for the 2L-VSC when using rectifier references.

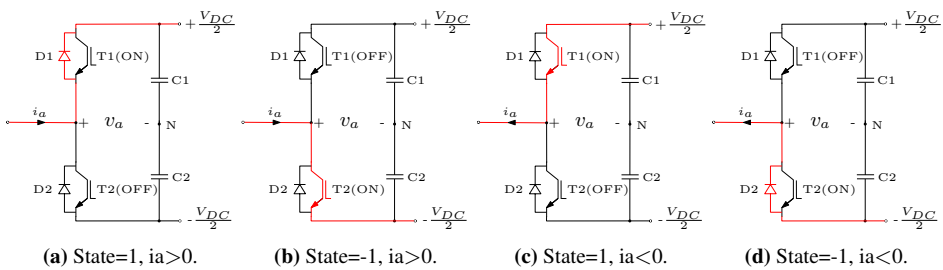


Figure 2.4: Conduction pattern in a phase-leg for a 2L-VSC.

Table 2.1: Possible states, voltages and device conduction.

State	V_a	T1	T2
1	$V_{dc}/2$	on	off
-1	$-V_{dc}/2$	off	on

2.2 The 3L-NPC converter

The 3L-NPC converter was first derived presented in 1981 [21] and extends the 2L-VSC by having an extra set of IGBTs and addition of clamping diodes. The converter topology is presented in Figure 2.5.

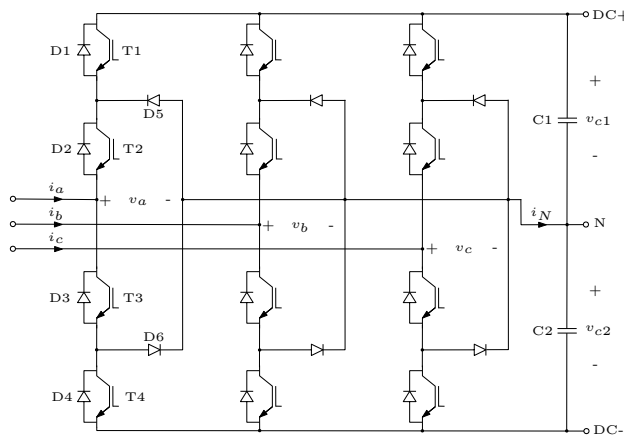


Figure 2.5: The 3L-NPC converter topology.

The clamping diodes are used to clamp the phase voltages to the neutral point. The voltage that the semiconductors are subjected to are reduced to half, compared to the 2L-VSC, due to the clamping diodes.

Table 2.2 show the three possible states, switching combination and voltage at phase a in the converter.

Table 2.2: Possible states, voltages and device conduction.

State	V_a	T1	T2	T3	T4
1	$V_{dc}/2$	on	on	off	off
0	0	off	on	on	off
-1	$V_{dc}/2$	off	off	on	on

The conduction pattern for the 3L-NPC converter are shown in Figure 2.6. Which device conducts the phase current depends on the state and the current direction.

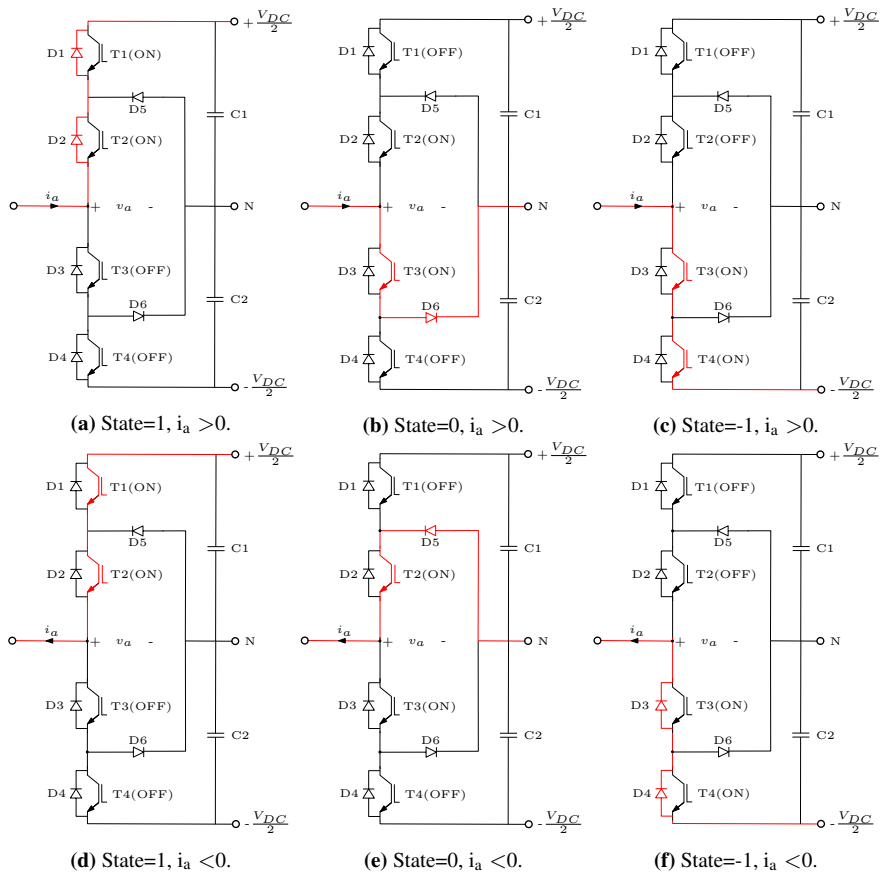


Figure 2.6: Conduction pattern in a phase-leg for a 3L-NPC converter.

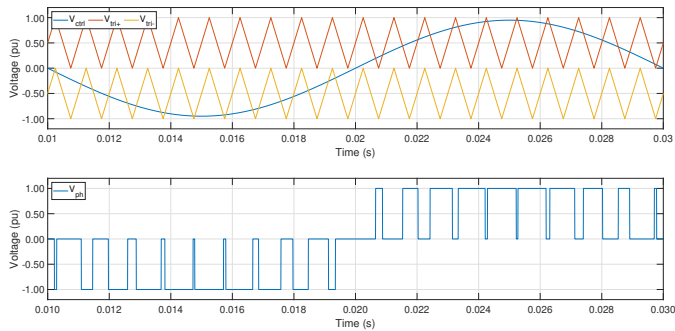


Figure 2.7: Modulation of a 3L-NPC converter.

Figure 2.7 show basic SPWM modulation of a 3L-NPC converter. The modulation resem-

bles the 2L-VSC modulation, but an extra triangular signal is added. The upper triangular signal goes from 0 to 1 and the lower from 0 to -1. The top switch T1 is “on” if the control signal is greater than the positive triangular signal. Switch T2 is on if the control signal is greater than the lower triangular signal. T3 are inverse of T1 and T4 inverse of T2.

2.2.1 DC capacitor voltage balancing

The switching of the semiconductors in the 3L-NPC converter lead to drift in the capacitor voltages [18]. If this is not controlled, one capacitor may take the full DC-bus voltage while the other is 0 V. This will lead to e.g. the upper or lower IGBTs and diodes being subjected to the full DC-bus voltage and semiconductor breakdown might occur. This is addressed as the main technical challenge of the 3L-NPC converter [22].

The problem relates to the charging/discharging of the capacitors and the average neutral point current. This current is again related to the phase currents i_{abc} and state 0 duty cycle for each phase d_{abc0} [23]. If this current is over time not zero, the voltages will drift.

The challenge can be overcome by adequate control strategies or by external hardware [18]. A great amount of works exist for control strategies such as [22],[23]. A control strategy will be used to control the voltages in this thesis, see chapter 2.7.

2.3 Description of ModHVDC generator

The ModHVDC technology enables transformerless wind turbines by segmenting the stator of a PMSG and series-connecting multiple power converters to facilitate HVDC in turbine terminals. Figure 2.8 presents an example of a ModHVDC generator/converter system with a four-segmented machine. The stator consist of four segments that are separated by an insulation material marked with blue lines. Within each segment the a-phase winding of all segments are highlighted. The result is four equivalent three-phase generators when including all three phase windings.

In previous research [1], the stator design was conducted with iron-less material. The material influences magnetic coupling between different segments and each segment was modelled as magnetically independent. Experimental validation with a prototype machine concluded that magnetic coupling between stator segments was negligible [1, Ch. 6.2.1]. The same numerical values for dq-axis inductance and resistance as in [1, Tab. 3.1] are used.

In Figure 2.8, the weak gray lines indicate the screening technology of the ModHVDC generator. This is further elaborated in Figure 2.9. Each isolated segment is clamped to the mid-point of the corresponding power converter DC-bus mid-point. The voltage-stress of each generator/converter module consists of an isolated AC-component and a DC-component dependant on the electrical distance from power converter to DC-link ground [16].

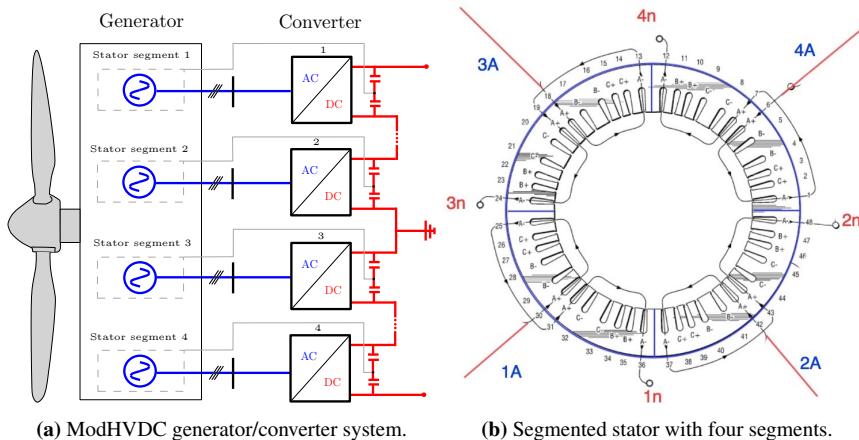


Figure 2.8: ModHVDC generator exemplified by a four-segmented machine with associated converters.

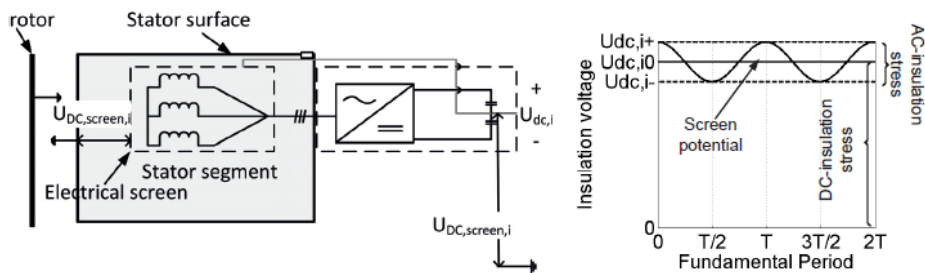


Figure 2.9: ModHVDC screening strategy [1, Fig. 3.2].

2.3.1 Modeling of a segmented PMSG

A mathematical description of a conventional PMSG with surface mounted magnets (round rotor construction) is presented in chapter A.2.1 and forms the basis for this modelling chapter. Round rotor PMSG and direct drive are common for wind turbines [5] and is therefore chosen for machine modeling. The rotor construction leads to an isotropic machine, i.e. equal dq axis inductance.

Representation in abc-reference frame

In this chapter, the modeling of a segmented machine with a general N number of segments is presented. Generator terminal voltage \vec{V}_{abc} is the starting point of the modeling.

$$\vec{V}_{abc} = -\mathbf{R}_s \vec{I}_{abc} + \frac{d\vec{\Psi}_{abc}}{dt} \quad (2.1)$$

The voltage depends on stator resistance R_s , stator current \vec{I}_{abc} and rate of change of total

stator side flux linkage $\vec{\Psi}_{abc}$. Stator resistance R_s are assumed to be equal for all phases. An arbitrary segment i individual resistance are given by $R_{s,i}$. The resistance matrix can be expressed as:

$$\mathbf{R}_s = \begin{bmatrix} R_{s,1} & 0 & 0 & \dots & 0 & 0 & 0 \\ 0 & R_{s,1} & 0 & \dots & 0 & 0 & 0 \\ 0 & 0 & R_{s,1} & \dots & 0 & 0 & 0 \\ \vdots & \vdots & \vdots & \ddots & \vdots & \vdots & \vdots \\ 0 & 0 & 0 & \dots & R_{s,N} & 0 & 0 \\ 0 & 0 & 0 & \dots & 0 & R_{s,N} & 0 \\ 0 & 0 & 0 & \dots & 0 & 0 & R_{s,N} \end{bmatrix} \quad (2.2)$$

The total stator-side flux linkage can be expressed as:

$$\vec{\Psi}_{abc} = -\mathbf{L}_{abc}^s \vec{I}_{abc} + \vec{\Psi}_{abc}^r \quad (2.3)$$

The stator-side inductance matrix \mathbf{L}_{abc}^s is an $N \times N$ -matrix. Due to magnetic independent segments, mutual inductance are zero. The non-zero elements in the matrix are identical to the stator inductance matrix in equation (A.8).

$$\mathbf{L}_{abc}^s = \begin{bmatrix} L_{a_1 a_1} & L_{a_1 b_1} & L_{a_1 c_1} & \dots & 0 & 0 & 0 \\ L_{b_1 a_1} & L_{b_1 b_1} & L_{b_1 c_1} & \dots & 0 & 0 & 0 \\ L_{c_1 a_1} & L_{c_1 b_1} & L_{c_1 c_1} & \dots & 0 & 0 & 0 \\ \vdots & \vdots & \vdots & \ddots & \vdots & \vdots & \vdots \\ 0 & 0 & 0 & \dots & L_{a_N a_N} & L_{a_N b_N} & L_{a_N c_N} \\ 0 & 0 & 0 & \dots & L_{b_N a_N} & L_{b_N b_N} & L_{b_N c_N} \\ 0 & 0 & 0 & \dots & L_{c_N a_N} & L_{c_N b_N} & L_{c_N c_N} \end{bmatrix} \quad (2.4)$$

The last term in equation (2.3) relates to rotor-side flux linkage contribution to stator-side total flux linkage and hence induced voltage in stator [1, p. 26]. All segments phases are referenced to the same electrical rotor position θ_r and equally phase-shifted. The model accounts for differences in flux linkage contribution from rotor to each stator segment i by the constant $\Psi_{m,i}$.

$$\vec{\Psi}_{abc}^r = \begin{bmatrix} \Psi_{m,1} \cos(\theta_r) \\ \Psi_{m,1} \cos(\theta_r - \frac{2}{3}\pi) \\ \Psi_{m,1} \cos(\theta_r + \frac{2}{3}\pi) \\ \vdots \\ \Psi_{m,N} \cos(\theta_r) \\ \Psi_{m,N} \cos(\theta_r - \frac{2}{3}\pi) \\ \Psi_{m,N} \cos(\theta_r + \frac{2}{3}\pi) \end{bmatrix} \quad (2.5)$$

Representation in dq-reference frame

By using the method of transformation as presented in chapter A.2.1, the dq-components of the segmented machine are:

$$V_{d,i} = -R_{s,N}I_{d,N} + \frac{d\Psi_{d,N}}{dt} - \Omega_r \frac{d\Psi_{q,N}}{dt} \quad (2.6)$$

$$V_{q,i} = -R_{s,N}I_{q,N} + \frac{d\Psi_{q,N}}{dt} + \Omega_r \frac{d\Psi_{d,N}}{dt} \quad (2.7)$$

The round rotor construction gives equal dq-axis inductance and is expressed by $L_{d,i} = L_{q,i} = L_{s,i}$. By expanding the expression for flux linkage, the final expression for electrical modeling of a stator-segmented PMSG expressed by dq-components and SI-units are obtained.

$$V_{d,i} = -R_{s,i}I_{d,i} - L_{s,i} \frac{dI_{d,i}}{dt} + \Omega_r L_{s,i} I_{q,i} \quad (2.8)$$

$$V_{q,i} = -R_{s,i}I_{q,i} - L_{s,i} \frac{dI_{q,i}}{dt} - \Omega_r L_{s,i} I_{d,i} + \Omega_r \Psi_{m,i} \quad (2.9)$$

The developed electrical torque expressed by dq-components are given by equation (2.10). The equation is valid for a round rotor machine. The symbol P_p is number of pole pairs and $k_{T,i}$ is the torque constant of each segment[24].

$$T_{e,i} = \frac{3}{2} P_p \Psi_{m,i} I_{q,i} = k_{T,i} I_{q,i} \quad (2.10)$$

Mechanical system

The mechanical direct drive system couples the wind turbine rotor directly to generator rotor shaft, so generator and turbine shaft share rotational speed. Figure 2.10 shows the difference between a geared and direct drive wind turbine.

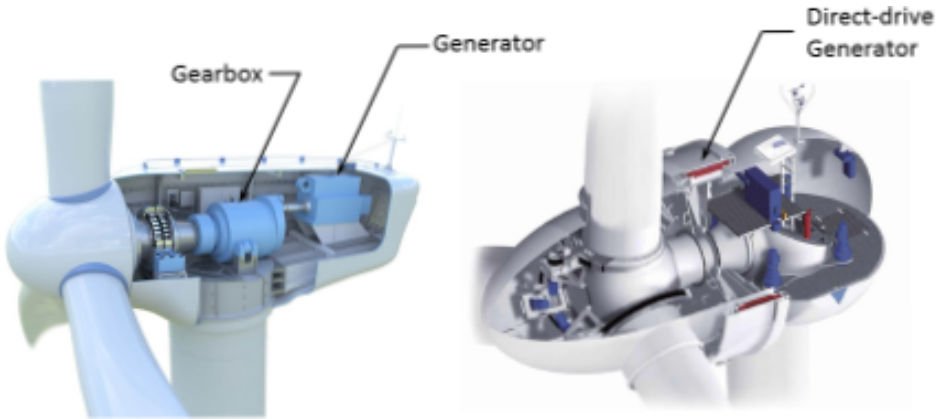


Figure 2.10: Wind turbine with and without gearbox in drivetrain [2].

The shaft speed is affected by the difference in electrical torque and mechanical torque T_m , where the electrical torque is a sum of developed torque in all segments $\sum_{i=1}^N T_{e,i}$. The chosen model treats the shaft as loss-less and infinitely stiff. Equation (2.11) presents

drivetrain dynamics in SI-units and equation (2.12) in per unit [25, p. 485]. The equations show that the generator/converter modules are mechanical coupled by common shaft speed.

$$J \frac{d\Omega_{r,m}}{dt} = T_m - \sum_{i=1}^N T_{e,i} \quad (2.11)$$

$$T_m \frac{d\omega_r}{dt} = \tau_m - \sum_{i=1}^N \tau_{e,i} \quad (2.12)$$

The symbol J represent total mechanical inertia of turbine (J_T) and generator (J_G). This is used in the per unit expression to calculate T_m , which is the mechanical time constant of the system. The symbols $\Omega_{b,m}$ and S_b are base value quantities found in chapter A.1.2.

$$T_m = \frac{J\Omega_{b,m}^2}{S_b} = \frac{(J_G + J_T)\Omega_{b,m}^2}{S_b} \quad (2.13)$$

Summary

A summary of exclusively the dq-components in per unit are presented in this chapter. The equations represents an arbitrary segment i . Transformation of these equation from SI-units to per unit are found in appendix chapter A.2.2. Per unit base values are seen in appendix chapter A.1.

Voltage

$$v_{d,i} = -r_{s,i}i_{d,i} - \frac{l_{s,i}}{\Omega_b} \frac{di_{d,i}}{dt} + \omega_r l_{s,i}i_{q,i} \quad (2.14)$$

$$v_{q,i} = -r_{s,i}i_{q,i} - \frac{l_{s,i}}{\Omega_b} \frac{di_{q,i}}{dt} - \omega_r l_{s,i}i_{d,i} + \omega_r \psi_{m,i} \quad (2.15)$$

Flux linkage

$$\psi_{d,i} = l_{s,i}i_{d,i} + \psi_{m,i} \quad (2.16)$$

$$\psi_{q,i} = l_{s,i}i_{q,i} \quad (2.17)$$

Power

$$p_i = v_{q,i}i_{q,i} + v_{d,i}i_{d,i} \quad (2.18)$$

$$q_i = v_{q,i}i_{d,i} - v_{d,i}i_{q,i} \quad (2.19)$$

Electromechanical torque

$$\tau_{e,i} = \psi_{m,i}i_{q,i} \quad (2.20)$$

Mechanical system

$$T_m \frac{d\omega_r}{dt} = \tau_m - \sum_{i=1}^N \tau_{e,i} \quad (2.21)$$

2.3.2 Simulation model in Simulink

Simulink does not provide a built-in model of a segmented PMSG and development of a custom made model was required. Description and validation of the model is presented in the appendix chapter A.2.3. A summary of the model and validation process is given in the following lines.

The model can be broken down into an electrical and a mechanical model. The electrical concerns the dynamics seen in equation (2.8) and (2.9). The model inputs are rotor speed Ω_r , rotor electrical angle θ_r and voltage V_{abc} . Outputs are torque T_e obtained by equation (2.10) and current I_{abc} . The current is the signal input to the physical modelling port current sources that are connected to the AC side of the converter. The torque is an input to the mechanical model. This model concerns the mechanical dynamics seen in equation (2.11). The input is the mechanical turbine torque T_m and the summed electrical torque $\sum_{i=1}^N T_{e,i}$. Output is rotor speed and electrical angle. The model is modular by being able to extend the number of segments by the number of electrical models.

Validation was conducted by comparing steady state and dynamic behaviour of the proposed model to Simulink's library model of a permanent magnet synchronous motor (PMSM) [26]. As this is a conventional PMSM, only a single-segment version of the proposed model was tested. It is assumed that if a model of a single segment machine is valid, then multiple segments are valid based on the modularity. The results showed negligible deviation between the proposed and reference model. The developed model of a segmented PMSG is valid for use in this thesis.

2.4 Description of ModHVDC converter system

The power converter interfaces a PMSG stator segment to the HVDC-link as seen in Figure 2.11. Series-connecting N number of power converters means that the HVDC-link voltage $v_{dc,tot}$ of roughly 100 kV is ideally divided equally to the converters DC-bus voltages $v_{dc,i}$.

$$v_{dc,i} = \frac{v_{dc,tot}}{N} \quad (2.22)$$

Another consequence of the series-connection is that the DC-side current of all converters must be equal in steady state, i.e. converter DC-bus current $i_{dc,i}$ equals DC-link current $i_{dc-link}$. Any difference are compensated by charging/discharging the DC-bus capacitors. This characteristics couples the generator/converter modules electrically.

$$\frac{c}{\Omega_b} \frac{dv_{dc,i}}{dt} = i_{dc,i} - i_{dc-link} \quad (2.23)$$

Equation (2.22) show that the power converter in this application is subjected to a considerable DC-bus voltage. The semiconductors in the converters will also be affected by this voltage and series-connection of devices might be required.

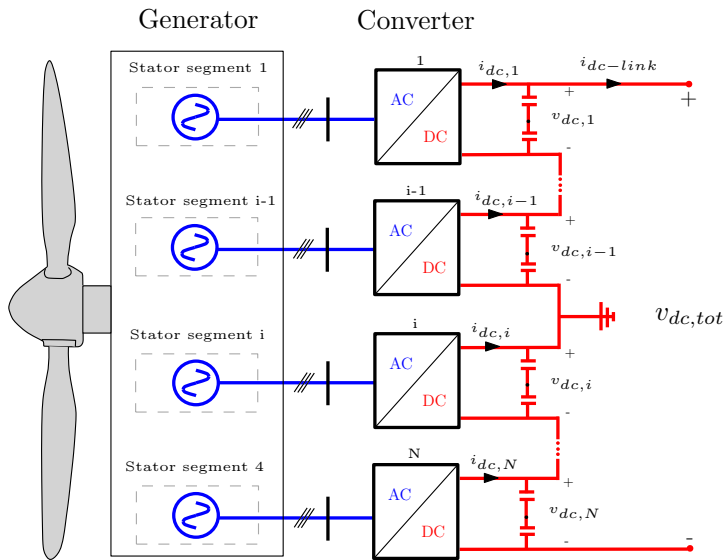


Figure 2.11: ModHVDC and converter system topology.

2.4.1 Required series-connection of semiconductors

Required series-connection of IGBTs and diodes for two and three-level converters for various number of segments was one of the result form the specialization project [16, Ch. 4]. This will now be revisited and improvements to the analytical expressions are performed [16, Eq. 4.1-4.4]. Figure 2.12 illustrate the series-connection in question.

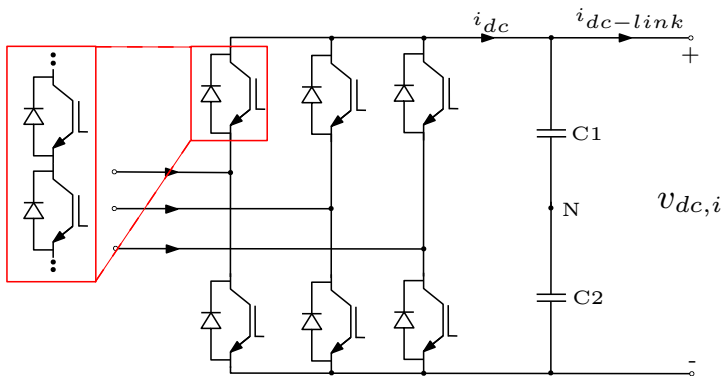


Figure 2.12: Series-connection of semiconductors exemplified in a 2L-VSC.

The voltage stress and number of series-connected devices are different for two and three-level converters. This can lead to differences in converter efficiency, but is dependant on the semiconductors [27]. Industrially IGBT modules are available for various voltage

levels V_{CES} , from 1.7 kV up to 6.5 kV for application-relevant modules [28]. A safety margin must be included when used in practice, such that utilization of the full rating of the modules is not possible. Safety margins y in the range 50 % and 60 % are typical values [29]. Equation (2.24) translates the DC-bus voltage to correspond to V_{CES} voltages by including the safety factor.

$$V_{dr} = V_{dc} \cdot \left(1 + \frac{y}{100}\right) \quad (2.24)$$

The DC-voltage V_{dc} depends on converter levels, number of converter segments N and redundant¹ modules z . Equation (2.25) expresses the voltage for a two-level converter and equation (2.26) for a three-level converter, where $V_{dc,tot}$ equals 100 kV.

$$V_{dc,2L} = \frac{V_{dc,tot}}{N - z} \quad (2.25)$$

$$V_{dc,3L} = \frac{V_{dc,tot}}{2 \cdot (N - z)} \quad (2.26)$$

The resulting required series-connection for a two-level and three-level converter are then given by equation (2.27) and equation (2.28) respectively. Numerical results to required IGBT module series-connection are found in chapter 4.2.

$$n_{series,2L} = \left\lceil \frac{V_{dr,2L}}{V_{CES}} \right\rceil = \left\lceil \frac{\frac{V_{dc,tot}}{N - z} \cdot \left(1 + \frac{y}{100}\right)}{V_{CES}} \right\rceil \quad (2.27)$$

$$n_{series,3L} = \left\lceil \frac{V_{dr,3L}}{V_{CES}} \right\rceil = \left\lceil \frac{\frac{V_{dc,tot}}{2 \cdot (N - z)} \cdot \left(1 + \frac{y}{100}\right)}{V_{CES}} \right\rceil \quad (2.28)$$

2.5 Wind turbine model

Wind turbine power curves are typically divided into four regions, as seen in Figure 2.13. The operational region is decided by the wind speed V_w .

- Region 1: Wind speed below turbine cut-in wind speed. $V_w < V_{w,in}$.
- Region 2: Wind speed greater than turbine cut-in wind speed and lower than turbine rated wind speed. $V_{w,in} \leq V_w < V_{w,r}$.
- Region 3: Wind speed greater than rated wind speed and lower than cut-out wind speed. $V_{w,r} \leq V_w < V_{w,out}$.
- Region 4: Wind speed greater than cut-out wind speed. $V_w \geq V_{w,out}$.

¹Accounting for converter operation with one or more converters out of service

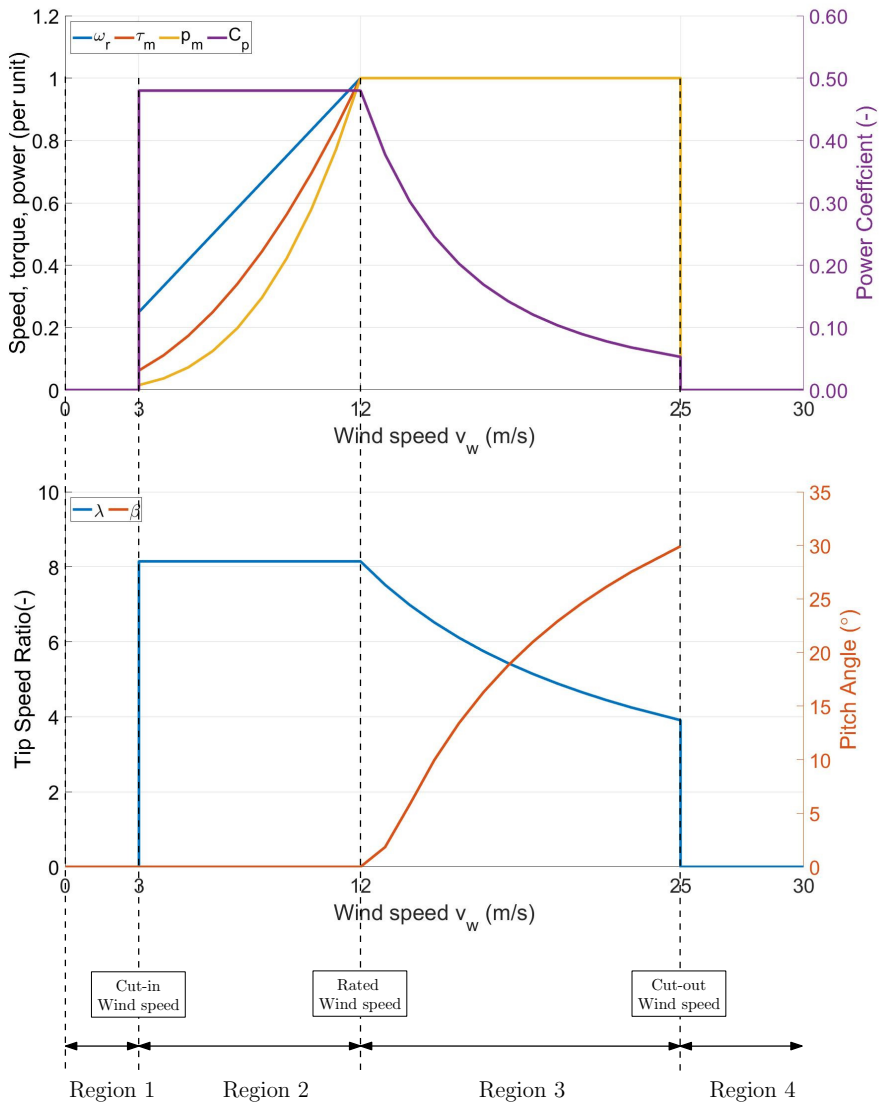


Figure 2.13: The four operational regions of a wind turbine. Inspired by [3].

When the wind speed exceeds turbine cut-in wind speed, the turbine starts power production. In this region the idealized power curve shows a cubed proportionality to wind speed ($P_m \propto V_w^3$). The region is upper limited by the turbine rated wind speed. In this region, the turbine can operate at maximum efficiency, i.e. the power coefficient C_p is maximized. However, this relies on rotational speed being proportional to the wind speed ($\Omega_r \propto V_w$) [3]. The proportionality might not hold for all wind speeds if the speed of rotation is bounded by upper and lower limits. In this model, these limits are ignored and

it is assumed that the the rotational speed is proportional to all wind speeds in region 2.

The other regions are characterized by lack of aerodynamic power (region 1) and excessive aerodynamic power (region 3 and 4). In region 1 the turbine does not produce power as wind speed is below turbine cut-in wind speed. In region 3 the power coefficient must be decreased to avoid mechanical and electrical overloading of turbine and generator. A modern and large wind turbine shed of aerodynamic power by pitching the rotor blade angle β , known as pitch angle control [25, p. 483]. It is typically only active in regions 3 and is a hydraulic and relatively slow system[25, p. 484]. In region 4, the turbine is at stand-still as the forces acting on the turbine might cause damage.

2.5.1 Turbine rotor model

Turbine mechanical power is given by equation (2.29) [25, p. 482]. This equation produces the idealized power curve seen in Figure 2.13. The idealization implies neglecting the effect of e.g. wind turbulence and other phenomena influence to the power curve. Numerous works exists to evaluate effect of these phenomena to the power curve [3], [30], [31]. Despite their non-negligible influence, the power curve are treated as ideal in this thesis. As equation (2.29) states, the power is a product of air density ρ , turbine swept area A_r , power coefficient $C_p(\lambda, \beta)$ and the wind speed V_w cubed.

$$P_m = \frac{1}{2}\rho A_r C_p(\lambda, \beta) V_w^3 \quad (2.29)$$

The most complex variable in equation (2.29) is the power coefficient. It is theoretically limited by Betz law of maximum conversion of kinetic energy in wind, i.e. numerical limitation of 0.593 [32, p. 325]. To obtain a detailed power coefficient for a turbine, experimental or numerical methods might be needed [3]. In this thesis, the numerical approximation applied in Simulink's built-in wind turbine model is used [33].

$$C_p(\lambda, \beta) = 0.5176 \left(\frac{116}{\lambda_i} - 0.4\beta - 5 \right) \exp \left(-\frac{21}{\lambda_i} \right) + 0.0068\lambda \quad (2.30)$$

The tip speed ratio (TSR) λ depends on turbine shaft speed $\Omega_{r,m}$, wind speed and rotor blade radius R_r . The variable λ_i is a function of TSR and pitch angle. For maximizing and controlling the power coefficient, a maximum power point tracker and speed controller is used.

$$\lambda = \frac{\Omega_{r,m} R_r}{V_w} \quad (2.31)$$

$$\lambda_i = \frac{(\lambda + 0.08\beta)(\beta^3 + 1)}{\beta^3 + 1 - 0.035(\lambda + 0.08\beta)} \quad (2.32)$$

2.5.2 Maximum power point tracking

With the chosen turbine model, the optimal TSR λ_{opt} in region 2 is 8.067 with an associated maximum power coefficient of 0.48. The speed controller in the control system

secures this operation, but requires a reference speed. The turbine maximum power point tracking (MPPT) provides this reference, see Figure 2.14.

Multiple MPPT control algorithm exist for wind turbines [18], where tip-speed-ratio control is used in this model. The method uses an anemometer to measure the wind speed and provides a reference shaft speed ($\Omega_{r,m}^*$).

$$\Omega_{r,m}^* = \frac{V_w \cdot \lambda_{opt}}{R_r} \quad (2.33)$$

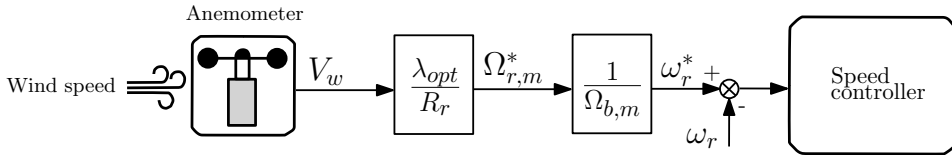


Figure 2.14: Principle sketch of the implemented TSR MPPT-strategy.

2.6 Wind speed model

The wind speed model serve two purposes:

1. Wind speed input to turbine in Simulink environment for dynamic analysis of the system seen in Figure 2.1.
2. Calculation of energy losses over a period, e.g. annually.

For the first purpose, the wind speed is modelled as laminar, height-independant without any turbulence or non-idealities. The wind speed is limited to turbine operational region 2 (3-12 m/s).

For the second purpose a wind speed distribution is needed. Wind turbines are designed based on classes given by the International Electrotechnical Commission's (IEC) standard 61400-1 [34, Tab. 1]. Wind turbine class I average wind speed $V_{w,avg}$ at 10 m/s is used as it poses the highest wind speed. The value are in line with annual 80 m height wind speed for the Norwegian continental shelf in the North Sea [35]. In accordance to [34, p. 22], the Rayleigh function is used. The Rayleigh distribution is a special case of a Weibull distribution, where the shape parameter k equals 2 [32, p. 343]. The corresponding scale parameter C are given by equation (2.34), while the probability and cumulative density function are given by equation (2.35) and (2.36).

$$C = \frac{2 \cdot V_{w,avg}}{\sqrt{\pi}} \quad (2.34)$$

$$f(V_w) = \frac{\pi \cdot V_w}{2 \cdot V_{w,avg}^2} \exp \left[-\frac{\pi}{4} \left(\frac{V_w}{V_{w,avg}} \right)^2 \right] \quad (2.35)$$

$$F(V_w \leq V_{w,avg}) = 1 - \exp \left[-\frac{\pi}{4} \left(\frac{V_w}{V_{w,avg}} \right)^2 \right] \quad (2.36)$$

The wind speed model characteristics are given by Table 2.3. A discretized probability density function are presented in Figure 2.15. This discretized model is used for purpose two.

Table 2.3: Wind model characteristics.

Annual mean wind speed ($V_{w,avg}$)	10 m/s
Weibull shape parameter (k)	2
Weibull scale parameter (C)	11.3

Table 2.4 is a tabular presentation of Figure 2.3. The table emphasises the intervals of wind speed in turbine operational region 1 (0-2 m/s), operational region 2 (3-12 m/s), operational region 3 (12-24 m/s) and operational region 4 (25-35 m/s).

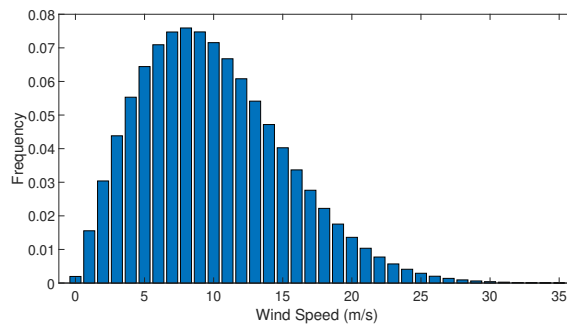


Figure 2.15: Discretized wind speed distribution.

Table 2.4: Wind speed distribution.

Wind speed (m/s)	0-2	3	4	5	6	7	8	9	10	11	12-24	25-35
Frequency (%)	4.8	4.4	5.5	6.4	7.1	7.5	7.6	7.5	7.2	6.7	34.5	0.9

2.7 Control system

The control system is presented in Figure 2.16. The system composes of a:

- Current controller
- Speed controller
- DC-bus voltage balancing controller
- Capacitor voltage balancing controller (only for 3L-NPC converter)

This chapter will give an introduction to each controller and its purpose. Tuning method and controller constants are given in appendix chapter A.2.4.

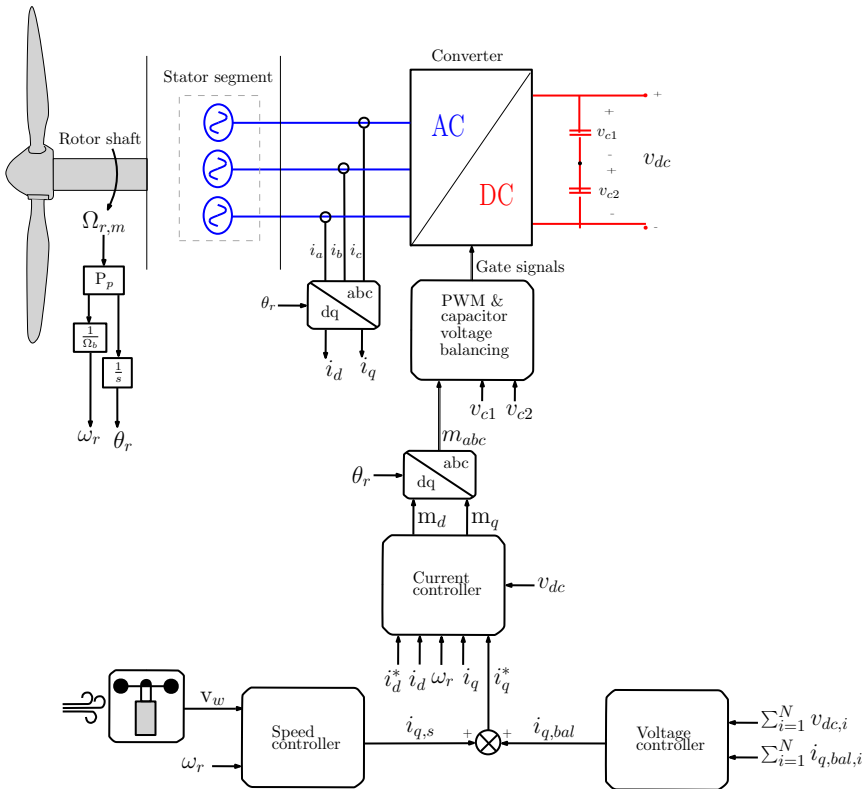


Figure 2.16: Control system.

Figure 2.17 show a conventional current controller with PI-controllers for a PMSG [36]. This controller controls the dq-axis current i_d and i_q for each generator/converter module. The q-axis current relates to torque, while d-axis current relates to magnetization of the machine. The former is controlled by the outer loop controllers, i.e. speed and DC-bus

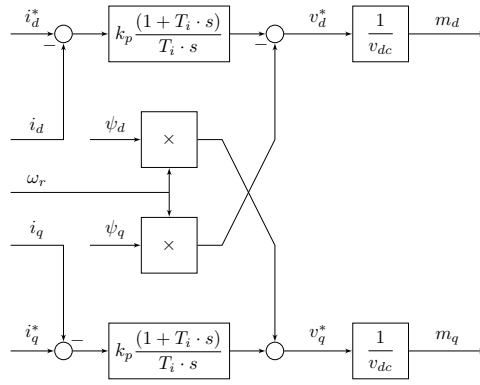


Figure 2.17: Current controller structure.

voltage controllers, while the d-axis current reference i_d^* is kept zero for all operation.

Speed controller structure is given by Figure 2.18. The wind speed is multiplied by a constant in order to obtain a shaft speed reference ω_r^* for securing maximum turbine performance coefficient. The controller outputs a reference q-axis current that is distributed with equal value to all converters.

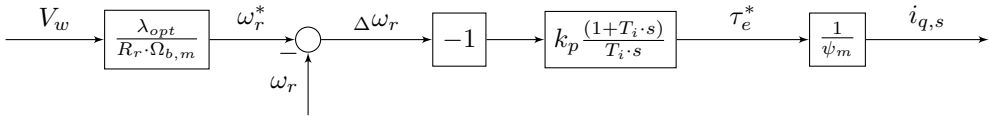


Figure 2.18: Speed controller structure.

The DC-bus voltage controller structure is seen in Figure 2.19 and is credited to [1, Ch. 4]. Ideally the speed controller q-axis current reference should be sufficient for the converter to have equal DC-bus voltages. However, if there are variations between generator/converter modules DC-side power, a corresponding voltage variation will arise. This controller balances DC-bus voltages by increasing/decreasing q-axis reference current to the current controller of each module. The constant K_δ is the droop constant of the controller. Droop control is implemented to overcome the problem of an overdetermined system and ensure minimal torque offset in steady state [1, Ch. 4].

The capacitor voltage balancing controller is built-in to the SPWM generator block in the simulation model. The PWM generator is a Simulink library block [37]. Modulation signals in abc-reference frame, DC-bus voltage and difference in capacitor voltages are input to the block. Proportional control is implemented and amplifies capacitor voltage error. The input signals are used to calculate gating times. If there is no capacitor voltage deviation, the gate signals are as given by the modulation signal. However, a voltage deviation alters the gating times in order to balance the capacitor voltages [37].

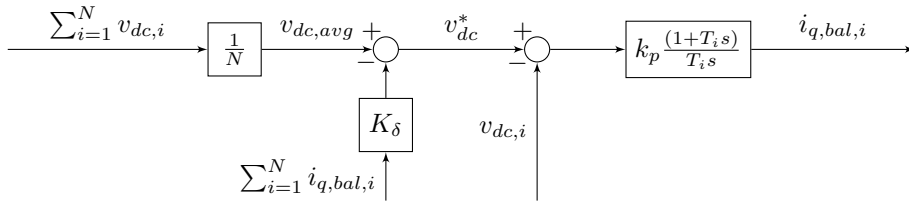


Figure 2.19: DC-bus voltage balancing controller structure.

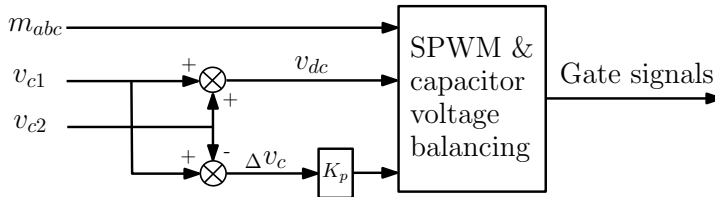


Figure 2.20: SPWM and capacitor voltage balancing controller structure.

2.8 HVDC grid

The modelling approach to the HVDC grid is presented in Figure 2.21. The cable connection to shore is modelled as a pure resistance. Onshore substation is assumed to be a large MMC that keeps constant 100 kV and is justified by time-scale separation, reduction of complexity and thesis emphasis. Cable modelling can be complex and cascaded pi-sections with multiple parallel branches might be required for accurate representation. A simple representation by a pure resistance might be better than insufficient cable models [38] and are therefore chosen, as accurate cable representation are out of scope for the thesis.

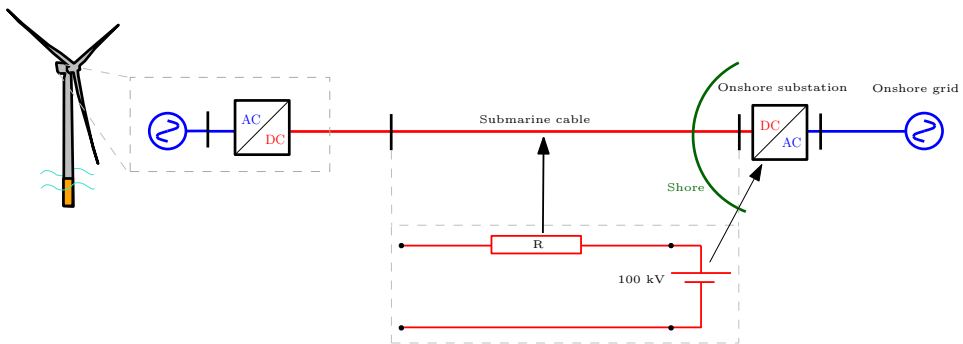


Figure 2.21: HVDC grid model.

DC-bus voltage controller analysis

The power converter DC-side series-connection couples each generator/converter module by a common DC-link current. This coupling and associated required control was studied in [1], but is revisited in order to further investigate control strategies for achieving balanced DC-bus voltages for a non-ideal system. The difference between generator/converter modules are studied by parameter variation in:

- Flux linkage $\psi_{m,i}$
- Stator resistance $r_{s,i}$
- Converter efficiency η_i

3.1 Steady state analysis

The following equations describes the steady state of the system. All derivatives in the equations in chapter 2.3.1 and d-axis current are zero.

$$v_{d,i} = \omega_r l_{s,i} \dot{i}_{q,i} \quad (3.1)$$

$$v_{q,i} = -r_{s,i} \dot{i}_{q,i} + \omega_r \psi_{m,i} \quad (3.2)$$

$$\tau_m = \sum_{i=1}^N \tau_{e,i} = \sum_{i=1}^N i_{q,i} \psi_{m,i} \quad (3.3)$$

$$\dot{i}_{dc,i} = \dot{i}_{dc-link} \quad (3.4)$$

$$\dot{i}_{d,i} = 0 \quad (3.5)$$

Based on equation (3.4), it is shown in equation (3.6) that the DC-bus voltage of each module is proportional to its share to total power [1]. To achieve balanced DC-bus voltages, the DC power must be balanced.

$$\begin{aligned}
i_{dc,i} &= \frac{p_{dc,i}}{v_{dc,i}} = \frac{p_{dc,tot}}{v_{dc,tot}} = i_{dc-link} \\
\frac{v_{dc,i}}{v_{dc,tot}} &= \frac{p_{dc,i}}{p_{dc,tot}}
\end{aligned} \tag{3.6}$$

The steady state DC-side power can be linked to the AC-side by the converter efficiency η_i and using equation (2.18) and equation (3.2).

$$\begin{aligned}
p_{dc,i} &= \eta_i p_{ac,i} = \eta_i v_{q,i} i_{q,i} \\
p_{dc,i} &= \eta_i (-r_{s,i} i_{q,i}^2 + \omega_r \psi_{m,i} i_{q,i})
\end{aligned} \tag{3.7}$$

The total DC-side power is:

$$p_{dc,tot} = \sum_{i=1}^N p_{dc,i} = \sum_{i=1}^N \eta_i (-r_{s,i} i_{q,i}^2 + \omega_r \psi_{m,i} i_{q,i}) \tag{3.8}$$

Inserting the power equations back into (3.6) and an expression for DC-bus voltage in relation to DC-link voltage are found and expressed by AC-side components.

$$\frac{v_{dc,i}}{v_{dc,tot}} = \frac{\eta_i (-r_{s,i} i_{q,i}^2 + \omega_r \psi_{m,i} i_{q,i})}{\sum_{j=1}^N \eta_j (-r_{s,j} i_{q,j}^2 + \omega_r \psi_{m,j} i_{q,j})} \tag{3.9}$$

Equation 3.9 can be divided by the number of modules N , such that each modules individual contribution to average bus voltage and DC-power are found. The benefit of using this measure is that an ideal system will have 1.0 as voltage and power relationship, which is an easy measure to interpret.

$$\frac{v_{dc,i}}{v_{dc,avg}} = \frac{p_{dc,i}}{p_{dc,avg}} \tag{3.10}$$

3.2 DC-bus voltage controller regulation capability and challenges

The steady state analysis show how DC-bus voltage may vary, depending on supplied DC-power. System components such as generator insulation system, converter semiconductors and DC-capacitors can be subjected to increased voltage stress in some modules if this is not controlled. DC-side voltage deviation might be corrected by changing each modules AC-side q-axis current $i_{q,i}$ and hence DC-side power. A current for obtaining voltage balance is introduced as $i_{q,bal,i}$. The total q-axis current is then a sum of two current references, speed controller q-axis current reference $i_{q,s}$ and $i_{q,bal,i}$ as illustrated in Figure 2.16. Speed controller reference current are common for all modules, while the balancing current is individual for each module.

$$i_{q,i} = i_{q,s} + i_{q,bal,i} \quad (3.11)$$

The q-axis current of each module might be limited from 0 to 1 pu. Less than 0 pu implies motor operation while more than 1.0 pu is assumed to be overloading of a module. Then, the total q-axis current is limited to:

$$0 \leq i_{q,s} + i_{q,bal,i} \leq 1 \quad (3.12)$$

Speed controller current reference is zero or positive and follow wind speed as a quadratic function. The balancing current can be theoretical limited as:

$$\begin{aligned} 0 &\leq i_{q,s} + i_{q,bal,i} \leq 1 \\ 0 &\leq \left(\frac{v_w}{12}\right)^2 + i_{q,bal,i} \leq 1 \\ -\left(\frac{v_w}{12}\right)^2 &\leq i_{q,bal,i} \leq 1 - \left(\frac{v_w}{12}\right)^2 \end{aligned} \quad (3.13)$$

The balancing current is also a quadratic function, but can take both positive and negative values. The feasible region for this current under given constrains is seen in Figure 3.1.

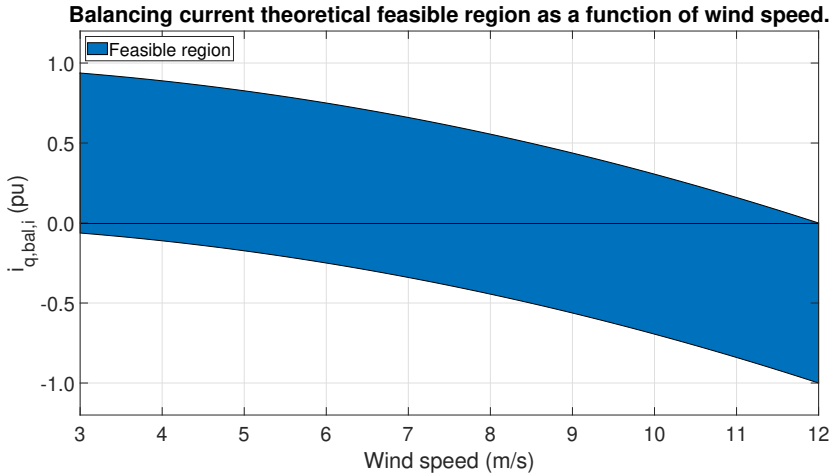


Figure 3.1: Feasible region of balancing current.

Voltage regulation by a positive balancing current is not possible at rated wind speed and above without overloading some modules. To achieve voltage balance in turbine region 3, DC-power of all modules must be decreased to the modules with lowest power output. This will lower the power delivered to the grid and is not desirable from an economic perspective and could be a liability for the ModHVDC generator. The concept claims benefit of increased system efficiency compared to convectional technologies, but this might not hold if turbine output power is reduced. However, an alternative is to increase the q-axis

current upper limit of 1.0 pu. In the following chapter, a case study is conducted where different control strategies and regulation capabilities are studied and how they affect the energy production of the system.

3.3 Case study

This case study involves eight ($N = 8$) modules with normal distributed parameters. The goal is to observe the effect in DC-bus voltage of multiple modules having parameter variation and the effect of two different control strategies. The resulting natural DC-bus voltages are presented in chapter 3.3.1. The first control strategy treats the q-axis current limit as a free variable, while strategy two constraint the current limit to 1.0 pu and lower power output. The results of these strategies are presented in chapter 3.3.2 and chapter 3.3.3 respectively.

The generator/converter modules parameters are normal distributed as according to equation the three equations below.

$$r_{s,i} \sim N(\mu_r, \sigma_r) \quad (3.14)$$

$$\eta_i \sim N(\mu_\eta, \sigma_\eta) \quad (3.15)$$

$$\psi_{m,i} \sim N(\mu_\psi, \sigma_\psi), \text{ where } \sum_{i=1}^8 \psi_{m,i} = 8 \text{ pu} \quad (3.16)$$

Expectation values (μ) and standard deviation (σ) are presented in Table 3.1. The values are chosen based two sources. The first is the experimental results in [1, p. 120]. The second is an article with a sensitivity analysis of numerous design variables influence on electrical parameters in a convectional interior magnet PMSM [39]. A prototype lab-scale machine used in the experimental result produced DC-bus voltage imbalance of 3.8 %. At this level, flux linkage and/or converter efficiency variation between modules are most likely present. DC-bus voltage imbalance is not that sensitive to stator resistance variation [1]. The article [39] show how numerous geometrical design variables can influence the electrical parameters. Additionally, [39] show how temperature influence both resistance and flux linkage. How the sum of these stochastic variables behaves dynamically and their actual standard deviation values remains to be investigated, but the presented values are considered reasonable for the purpose of this case study to simulate what a voltage variation.

Table 3.1: Parameter nominal/expected per unit values and standard deviation.

Parameter	Nom. val. (μ)	Std. dev. (σ)
$r_{s,i}$	0.02	0.005
η_i	0.98	0.010
$\psi_{m,i}$	1.00	0.025

Numerical values was generated by the pseudo-random number generator and the normal distribution-function in Excel. The modules are parameterized as seen in Table 3.2.

Table 3.2: Module parametrization with normal-distributed parameters.

Module	$r_{s,i}$	η_i	$\psi_{m,i}$
1	0.020	0.977	1.004
2	0.021	0.965	0.992
3	0.017	0.975	1.024
4	0.017	0.988	0.993
5	0.016	0.972	0.998
6	0.015	0.990	0.984
7	0.028	0.986	1.034
8	0.025	0.967	0.972

3.3.1 Voltage distribution without balancing current

Table 3.3 show DC-bus voltages when the generator/converter modules parameters are as given in Table 3.2. The extremes are found in module 7 and 8, where the voltage deviation are +4.1 % at cut-in wind speed and -4.5 % at rated wind speed respectively. As an numerical example, if the DC-link voltage is 100 kV, the percentage deviation are 0.52 kV for module 7 and -0.56 kV for module 8.

Table 3.3: Voltage distribution at various wind speeds when using normal distributed parameters.

Wind speed	$v_w = 3 \text{ m/s}$			$v_w = 9 \text{ m/s}$			$v_w = 12 \text{ m/s}$		
	$\frac{v_{dc,i}}{v_{dc,avg}}$	$\frac{v_{dc,i}}{v_{dc,avg}}$	dev.	$\frac{v_{dc,i}}{v_{dc,avg}}$	$\frac{v_{dc,i}}{v_{dc,avg}}$	dev.	$\frac{v_{dc,i}}{v_{dc,avg}}$	$\frac{v_{dc,i}}{v_{dc,avg}}$	dev.
1	1.003	0.3 %		1.003	0.3 %		1.003	0.3 %	
2	0.979	-2.1 %		0.978	-2.2 %		0.978	-2.2 %	
3	1.022	2.2 %		1.024	2.4 %		1.025	2.5 %	
4	1.004	0.4 %		1.005	0.5 %		1.006	0.6 %	
5	0.993	-0.7 %		0.995	-0.5 %		0.996	-0.4 %	
6	0.998	-0.2 %		1.000	0.0 %		1.001	0.1 %	
7	1.041	4.1 %		1.038	3.8 %		1.036	3.6 %	
8	0.960	-4.0 %		0.957	-4.3 %		0.955	-4.5 %	

3.3.2 Balancing current with no constraint and no power derating

This chapter presents the required balancing current for compensating the unbalanced voltage distribution in Table 3.3. The compensation should give symmetrical voltage distribution, i.e. all modules have equal voltage.

The required balancing current for achieving symmetrical voltage distribution are seen in Figure 3.2 and Table 3.4. The results show that the compensation current are greatest in module 7 and 8 as these modules have the largest positive and negative voltage deviation. The currents are -0.036 pu and +0.048 pu respectively.

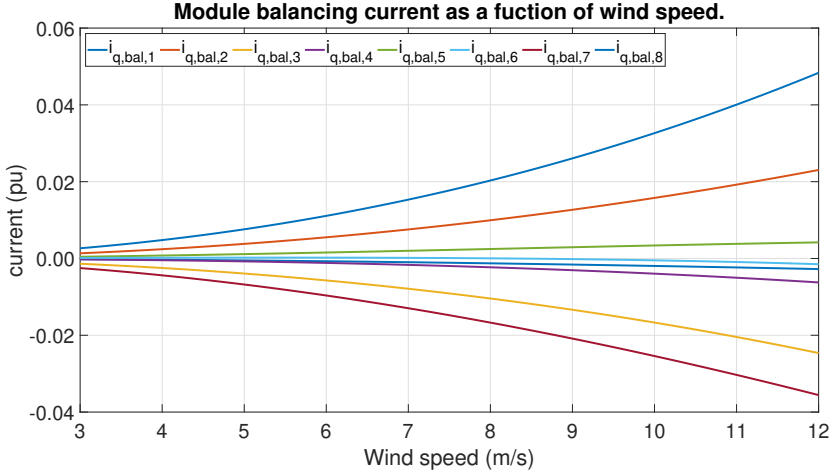


Figure 3.2: Balancing currents as a function of wind speed.

Table 3.4: Balancing current in per unit for achieving symmetrical voltage distribution.

Wind speed	$v_w=3$ m/s	$v_w=9$ m/s	$v_w=12$ m/s
Module	$i_{q,bal,i}$	$i_{q,bal,i}$	$i_{q,bal,i}$
1	0.000	-0.002	-0.003
2	0.001	0.013	0.023
3	-0.001	-0.013	-0.025
4	0.000	-0.003	-0.006
5	0.000	0.003	0.004
6	0.000	0.000	-0.002
7	-0.003	-0.021	-0.036
8	0.003	0.026	0.048

3.3.3 Balancing current with constraints and power derating

This analysis shall answer how much turbine derating is required to achieve symmetrical voltages and the corresponding balancing current in each module. Total q-axis current must be lower than or equal to 1.0 pu.

$$i_{q,i} = i_{q,s} + i_{q,bal,i} \leq 1 \quad (3.17)$$

Table 3.3 voltage distribution prove that module 8 provides the lowest DC-power. To

achieve equal DC-bus voltages, the average DC-power must be equal to the module with lowest DC-power (module 8).

$$\frac{p_{dc,i}}{p_{dc,avg}} = 1 \implies p_{dc,8} = p_{dc,avg} \quad (3.18)$$

Module 8 DC-power $p_{dc,8}$ equals 0.915 pu. To achieve the symmetrical voltage distribution, the balancing current for each module must be as seen in Table 3.5.

Table 3.5: Balancing currents for achieving symmetrical voltage distribution at rated wind speed and above.

Module	$i_{q,bal,i}$
1	-0.048
2	-0.024
3	-0.069
4	-0.052
5	-0.042
6	-0.047
7	-0.080
8	0.000

The DC-side power are now reduced. Average DC-side power can be seen in Table 3.6. The result show that the DC-side power are reduced by 0.043 pu and 4.5 % compared to the non-derated DC-side power.

Table 3.6: Power reduction to achieve symmetrical voltages.

Not derated $p_{dc,avg}$	Derated $p_{dc,avg}$	Difference
0.958 pu	0.915 pu	-0.043 pu

3.3.4 Comparison of annual energy output

By using the wind speed distribution from chapter 2.6, the reduced annual energy output by power derating modules can be calculated. The interval of interest is turbine operational region 3. The frequency of this region is 34.5 %. Table 3.6 show that the modules average DC-power output is 0.958 pu if no balancing current action is taken. If the voltage controller ensures equal DC-bus voltages for all modules, the average power reduces to 0.915 pu.

The annual energy production of a single turbine can be calculated by equation (3.19). Numerical results to annual energy production with and without voltage balancing are calculated.

$$E = p_{dc,avg} \cdot 10 \text{ MW} \cdot 34.5 \% \cdot 8760 \text{ h} \quad (3.19)$$

The result in Table 3.7 show that the power reduction leads to an annual energy reduction of 1300 MWh.

Table 3.7: Energy reduction to achieve symmetrical voltages.

Not derated E	Derated E	Difference
28953 MWh	27653 MWh	-1300 MWh

3.4 Outcome of case study

This case study uses normal-distributed parameters to eight generator/converter modules to investigate the effect of parameter variation between modules. Table 3.3 show how such a configuration can distribute DC-bus voltages for various wind speeds. The extremes of voltage deviation to average voltage was 4.1 % and -4.5 %, which corresponds to 0.52 and -0.56 kV.

The regulation capability and associated challenges was studied in chapter 3.2. The results showed that voltage deviation can be regulated freely in turbine operational region 2, but requires power derating in operation region 3. This is valid as long as overloading of the modules is not accepted.

Required current for equal DC-bus voltages when ignoring constraints was found in chapter 3.3.2. The current is quadratic and the maximum/minimum values are found at rated wind speed. For this case study, module 7 and 8 required most compensation. This was -0.036 pu and 0.048 pu balancing current respectively.

Chapter 3.3.3 showed how much power derating is required for having symmetrical voltages in turbine operational region 3. The result was a power reduction of 4.5 %. This reduction is in percentage identical to module 8 voltage deviation to average module voltage. The associated energy loss of power derating was calculated in chapter 3.3.4 to be 1.3 GWh/year.

The case study show that DC-bus voltage variation in the range of roughly ± 5 % might be expected. This is in-line with the experimental results in [1]. The following alternatives are proposed as feasible approaches to the problem of DC-bus voltage imbalance:

1. Accept module voltage imbalance. No voltage balancing measures taken.
2. Accept module voltage imbalance and/or overloading within a certain tolerance band. As an example, the voltage controller ensures that the DC-bus voltage of one or multiple modules are kept within the interval of ± 5 % to average DC-bus voltage.
3. Achieve voltage balance and accept current overloading of modules.
4. Achieve voltage balance by changing q-axis current and lower the modules DC-bus power such that the modules voltages are identical if required.

All alternatives have associated strength and weaknesses, but only alternative 4 includes lowering turbine DC-output power. Decreased power output is not a preferred choice

from an economic perspective. Required power decrease is in percentage equal to the percentage voltage deviation for the least stressed module. In the case study, this was module 8 with -4.5 % deviation. It might seem unreasonably conservative to lower turbine power output by 4.5 % for compensating a voltage difference of 4.5 %. If that is excluded, then the question arises of what is least stressful for the system; increased DC-bus voltage or increased q-axis current. A dedicated study is required to answer this question, as many aspects and system stress/aging factors should be accounted for. Additionally, how these control strategies influence the generator is also not considered. It is not the purpose of this study to provide a conclusion to the question of what strategy is to be implemented, but rather highlight the challenge and present plausible solutions.

Converter and IGBT module loss calculation

4.1 Introduction

The total semiconductor power losses can be divided into sub-categories as seen in Figure 4.1 [40, p. 274]. The figure identifies the IGBT module losses that are accounted for in this calculation.

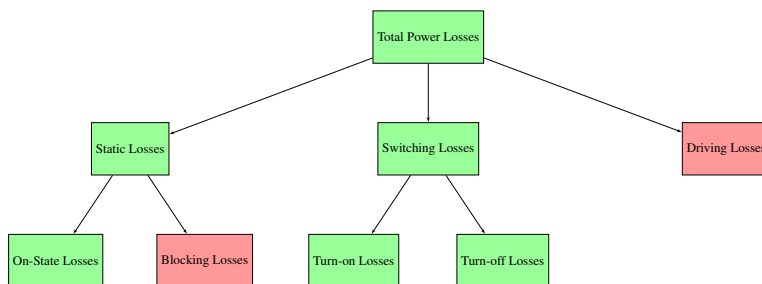


Figure 4.1: Classification of IGBT modules losses. Green boxes indicates considered losses, red indicate neglected losses.

An IGBT module consist of multiple IGBT and a diode dies, which forms one or multiple (n) equivalent IGBTs and diodes within a module. The dies dissipate power when conducting current and switching from one state to the other. A loss hierarchy for an IGBT module is seen in Figure 4.2. IGBT losses are conduction losses in addition to turn-on and turn-off switching losses. The diode losses are conduction and reverse recovery (turn-off) losses [41].

The analytical models in chapter 4.2.7 measure losses for a single equivalent IGBT and

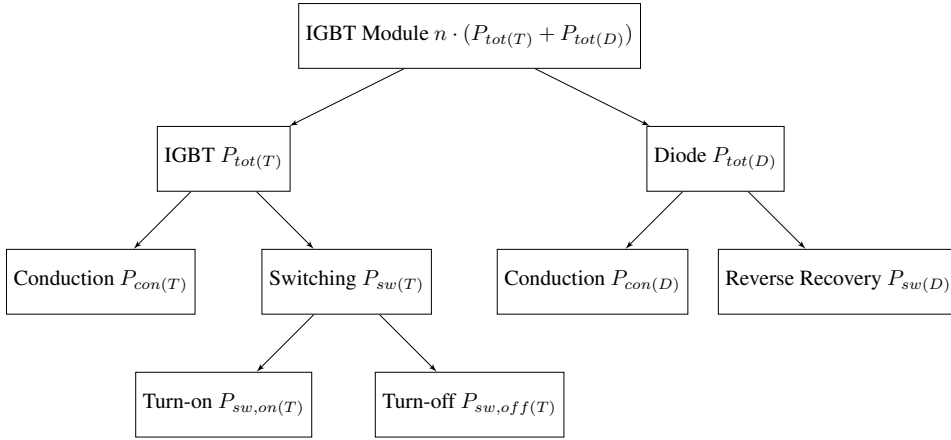


Figure 4.2: Hierarchy of power losses in an IGBT module.

diode within an IGBT module. As the considered modules in this calculation are single IGBTs ($n = 1$), module losses equals the sum of IGBT and diode losses. Series-connection of multiple modules must be accounted for in addition to number of converters when calculating total losses. The latter varies with number of segments, converter levels and design parameters. To calculate the total semiconductor losses for the system of converters, all these parameters must be accounted for. This is clarified in chapter 4.2.6 where measurement parameters are presented.

4.2 Method

In this section, the method and system set-up is presented. Selected IGBT modules, series-connection of semiconductors, switching frequency, semiconductor junction temperature, turbine operation and measurement parameters are all presented.

4.2.1 Power devices

Selection of IGBT modules are chosen from ABB's portfolio. Based on their selection of voltage classes: 3.3, 4.5 and 6.5 kV IGBT modules were investigated. Specific components are given in Table 4.1. For simplicity, the diodes within these IGBT modules are used as clamping diodes in the 3L-NPC converter.

Table 4.1: Studied IGBT modules.

Manufacturer	Model	V_{CES} (kV)	I_C (A)
ABB	5SNA 0400J650100	6.5	400
ABB	5SNA 0650J450300	4.5	650
ABB	5SNA 0800N330100	3.3	800

4.2.2 Series-connection

Table 4.2 and Table 4.3 presents required series connection of IGBTs and diodes for two and three level converters for 8 and 16 modules with 1 and 2 redundant modules respectively. A safety margin of $\gamma = 55$ was used in both calculations. The basis for the calculation is found in chapter 2.4.

Table 4.2: Required series-connection of devices with 8 segments ($N = 8$) and 1 redundant modules ($z = 1$).

V_{CES} IGBT (kV)	$n_{series,2L}$	$n_{series,3L}$
6.5	4	2
4.5	6	3
3.3	8	4

Table 4.3: Required series-connection of devices with 16 segments ($N = 16$) and 2 redundant modules ($z = 2$).

V_{CES} IGBT (kV)	$n_{series,2L}$	$n_{series,3L}$
6.5	2	1
4.5	3	2
3.3	4	2

4.2.3 Converter switching frequency

Switching frequency influence switching losses in IGBTs and diodes and should be studied for various values when comparing various voltage ratings of semiconductors. Based on the work of [42], a switching frequency range of 0.5-2.0 kHz is considered as feasible for the full-scale 10 MW ModHVDC application and is therefore studied.

4.2.4 IGBT and diode junction temperatures

Thermal stress is the main contributor to power electronic failures [19, Fig. 3.1]. For reliability considerations, device junction temperature should be limited to 70-80 % of maximum allowable junction temperature [43]. The average junction temperatures of devices are limited to 75 °C in this analysis. Junction temperatures for semiconductors in the 2L-VSC and 3L-NPC converter are given in Table 4.4 and Table 4.5.

Table 4.4: Junction temperatures in 2L-VSC loss analysis.

Device	T_j (°C)
IGBT	75
Diode	75

Table 4.5: Junction temperatures in 3L-NPC converter loss analysis.

Device	T_j (°C)
T1 and T4	60
T2 and T3	75
D5 and D6	60
D1 and D4	70
D2 and D3	65

4.2.5 Turbine operation

Turbine and generator operation are limited to nominal operation. The wind speed distribution in Figure 2.15 show that the turbine are in nominal operation for about 1/3 of a year. By multiplying power production and wind speed distribution it can be proven that roughly 2/3 of turbine annual energy production are at nominal operation. Therefore,

this operation point is of highest priority. An ideal mechanical system and generator are assumed. Rated converter AC-input power are therefor in total 10 MW.

4.2.6 Measurement parameters

The semiconductor losses of a full scale 10 MW configuration involves calculating IGBT and diode individual losses, then multiplying by the number of components in a base configuration, further multiply by number of series-connected devices and number of converters in the system.

The expression for total losses with the 2L-VSC are given by equation (4.1). The analytical expression for losses applies for a single IGBT and diode. There are six IGBTs and diodes in a two-level converter. Since a series-connection is required, number of series-connected devices $n_{\text{series},2L}$ must be multiplied into the equation. As seen in Table 4.2 and Table 4.3, number of series-connected devices depends on number of segments. Number of segments N must also be included.

$$P_{tot,2L} = N \cdot n_{\text{series},2L} \cdot 6 \cdot (P_{sw(T)} + P_{con(T)} + P_{sw(D)} + P_{con(D)}) \quad (4.1)$$

The 3L-NPC converter have an unequal loss distribution, but symmetrically placed devices have equal losses. In equation (4.2), this can be exemplified by the most upper (T1) and most lower IGBT (T4) switching losses $P_{sw(T1\&T4)}$. The term $P_{sw(T1\&T4)}$ is not the sum of T1 and T4 switching losses, but the individual switching loss for T1 and T4. As losses in symmetrically placed components are expressed by the same equation, a factor of two arises. Since there are three phase legs, the losses in a base configuration is multiplied by three. This leads to the constant 6 and forms the base configuration. Finally, number of series-connected devices and number of converters must be multiplied into the equation to obtain total losses.

$$\begin{aligned} P_{tot,3L} = N \cdot n_{\text{series},3L} \cdot 6 \cdot & (P_{sw(T1\&T4)} + P_{con(T1\&T4)} + P_{sw(T2\&T3)} + P_{con(T2\&T3)} \\ & + P_{sw(D1\&D4)} + P_{con(D1\&D4)} + P_{sw(D2\&D3)} + P_{con(D2\&D3)} \\ & + P_{sw(D5\&D6)} + P_{con(D5\&D6)}) \end{aligned} \quad (4.2)$$

The chosen turbine operation leads to a total of 10 MW as input power to the AC-side of the converters. Efficiency can be calculated for both converters as

$$\eta = \frac{10 \text{ MW} - P_{tot}}{10 \text{ MW}} \quad (4.3)$$

4.2.7 Analytical models

The models for semiconductor losses in a 2L-VSC and 3L-NPC converter are found in literature published by the German-based power semiconductor manufacturer Semikron. Data input to both models and list of symbols are found in appendix chapter A.3.1.

2L-VSC

The following analytical model estimates the power losses in a single IGBT (T) and diode (D) in a 2L-VSC with conventional sinusoidal pulse width modulation scheme. The model is originates from [40, p. 277-279]. Minor changes to that corresponds to the 3L-NPC loss model found in [17, p. 9] regarding the current are implemented.

$$P_{con(T)} = \left(\frac{1}{2\pi} + \frac{m_a \cos \phi}{8} \right) V_{CE0}(T_j) \cdot \hat{I} + \left(\frac{1}{8} + \frac{m_a \cos \phi}{3\pi} \right) R_{CE}(T_j) \cdot \hat{I}^2 \quad (4.4)$$

$$P_{con(D)} = \left(\frac{1}{2\pi} - \frac{m_a \cos \phi}{8} \right) V_{F0}(T_j) \cdot \hat{I} + \left(\frac{1}{8} - \frac{m_a \cos \phi}{3\pi} \right) R_F(T_j) \cdot \hat{I}^2 \quad (4.5)$$

$$P_{sw(T)} = f_{sw} \cdot E_{sw} \cdot \frac{1}{\pi} \left(\frac{\hat{I}}{I_{ref}} \right)^{K_i} \left(\frac{V_{cc}}{V_{ref}} \right)^{K_v} (1 + T_{E_{sw}}(T_j - T_{ref})) \quad (4.6)$$

$$P_{sw(D)} = f_{sw} \cdot E_{rr} \cdot \frac{1}{\pi} \left(\frac{\hat{I}}{I_{ref}} \right)^{K_i} \left(\frac{V_{cc}}{V_{ref}} \right)^{K_v} (1 + T_{E_{rr}}(T_j - T_{ref})) \quad (4.7)$$

Equation (4.4) and (4.5) is a linearized temperature-dependant model of IGBT on-state and diode forward characteristic to calculate conduction losses. An illustration of the linearization and how to obtain the variables is presented in Figure 4.3. Linear interpolation to an arbitrary junction temperature T_j is required, as the datasheet limits temperatures to 25 and 125 °C. The interpolation is given by equation (4.8) for X , which represent all four linearization constants.

$$X(T_j) = \frac{X^{125^\circ C} - X^{25^\circ C}}{100} \cdot (T_j - 25) + X^{25^\circ C} \quad (4.8)$$

The expression within the parentheses in equation (4.4) and (4.5) describes the sinusoidal dependency of duty cycles versus time. It is based on the assumption of linear modulation ($m_a \leq 1$), which is valid for all steady-state operation in this application.

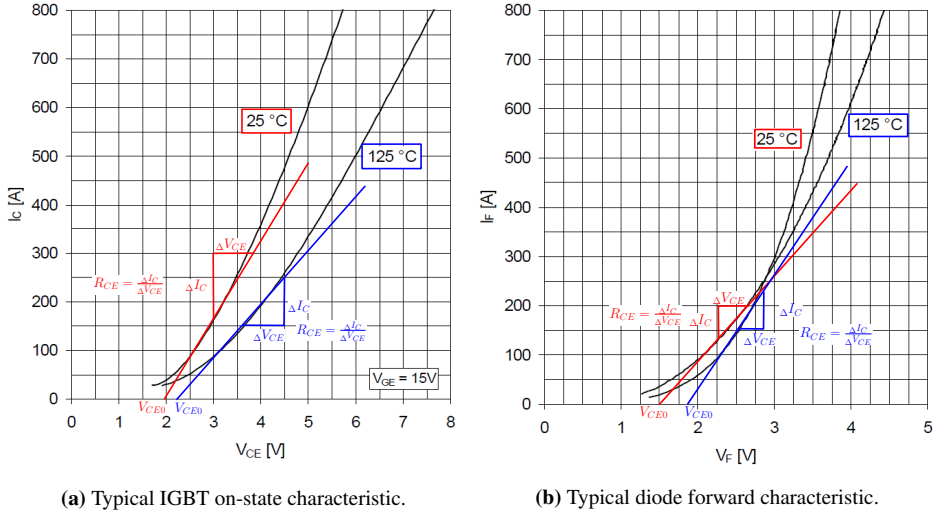


Figure 4.3: linearization of typical on-state output characteristic of IGBT and typical diode forward characteristic of ABB 5SNA 0400J650100 IGBT [4].

The switching losses are given by equation (4.6) and (4.7). Difference to datasheet current, voltage and temperature reference values are compensated by the correction factors. Exponents are used in current and voltage correction factors, while junction temperature correction is a linear function. The current exponent K_i for an IGBT are generally approximately 1.0 and in the range of 0.5...0.6 for a diode [40, p. 279]. For the specific IGBT modules, the exponents are chosen to 0.90 for the IGBT and 0.57 for the diode. The correction is implemented as the original exponents was a better fit for IGBT modules with current closer to reference value. Voltage correction factor exponents are chosen as 1.2 and 0.6 for the IGBT and diode. Lower interval value ($K_v = 1.2$) of IGBT voltage exponent given by [44, Eq. 4] is chosen. Other models [41],[45],[46] uses a linear relationship ($K_v = 1$) and the chosen value is therefor seen as a justifiable value for the voltage exponents. Junction temperature is modeled as an average value.

3L-NPC

The analytical models for IGBT and diodes switching and conduction losses in a 3L-NPC converter are based on [17]. The model for switching losses is modified by adding a correction factor to compensate for junction temperature difference to datasheet reference value. This is the same correction factor used in the analytical model for the 2L-VSC.

Conduction and switching losses for all devices are presented in the following equations. Unlike the 2L-VSC, the loss distribution is unequal. Therefor, losses for symmetric components are presented below. Explanation to component reference is given by Figure 2.5.

T1 and T4

$$P_{con} = \frac{m_a \hat{I}}{12\pi} \cdot (3V_{CE0}(T_j) \cdot ((\pi - \phi) \cdot \cos \phi + \sin \phi) + 2R_{CE}(T_j) \cdot \hat{I} \cdot (1 + \cos \phi)^2) \quad (4.9)$$

$$P_{sw} = f_{sw} \cdot E_{sw} \cdot \left(\frac{\hat{I}}{I_{ref}} \right)^{K_i} \left(\frac{V_{CC}}{V_{ref}} \right)^{K_v} \left(\frac{1 + \cos \phi}{2\pi} \right) (1 + T_{E_{sw}}(T_j - T_{ref})) \quad (4.10)$$

T2 and T3

$$P_{con} = \frac{\hat{I}}{12\pi} \cdot (V_{CE0}(T_j) \cdot (12 + 3m_a(\phi \cos \phi - \sin \phi) + R_{CE}(T_j) \cdot \hat{I} \cdot (3\pi - 2m_a(1 - \cos \phi)^2))) \quad (4.11)$$

$$P_{sw} = f_{sw} \cdot E_{sw} \cdot \left(\frac{\hat{I}}{I_{ref}} \right)^{K_i} \left(\frac{V_{CC}}{V_{ref}} \right)^{K_v} \left(\frac{1 - \cos \phi}{2\pi} \right) (1 + T_{E_{sw}}(T_j - T_{ref})) \quad (4.12)$$

D5 and D6

$$P_{con} = \frac{\hat{I}}{12\pi} \cdot (V_{F0}(T_j) \cdot (12 + 3m_a((2\phi - \pi) \cos \phi - 2 \sin \phi) + R_F(T_j) \cdot \hat{I} \cdot (3\pi - 4m_a(1 + \cos^2 \phi)))) \quad (4.13)$$

$$P_{sw} = f_{sw} \cdot E_{rec} \cdot \left(\frac{\hat{I}}{I_{ref}} \right)^{K_i} \left(\frac{V_{CC}}{V_{ref}} \right)^{K_v} \left(\frac{1 + \cos \phi}{2\pi} \right) (1 + T_{E_{sw}}(T_j - T_{ref})) \quad (4.14)$$

D1 and D4

$$P_{con} = \frac{m_a \hat{I}}{12\pi} \cdot (3V_{F0}(T_j) \cdot (-\phi \cos \phi + \sin \phi) + 2R_F(T_j) \cdot \hat{I} (1 - \cos \phi)^2) \quad (4.15)$$

$$P_{sw} = f_{sw} \cdot E_{rec} \cdot \left(\frac{\hat{I}}{I_{ref}} \right)^{K_i} \left(\frac{V_{CC}}{V_{ref}} \right)^{K_v} \left(\frac{1 - \cos \phi}{2\pi} \right) (1 + T_{E_{sw}}(T_j - T_{ref})) \quad (4.16)$$

D2 and D3

$$P_{con} = \frac{m_a \hat{I}}{12\pi} \cdot (3V_{F0}(T_j) \cdot (-\phi \cos \phi + \sin \phi) + 2R_F(T_j) \cdot \hat{I} (1 - \cos \phi)^2) \quad (4.17)$$

$$P_{sw} = 0 \quad (4.18)$$

4.3 Results

4.3.1 2L-VSC

Figure 4.4 show IGBT and diode switching losses as a function of switching frequency for the three modules. Table 4.6 show IGBT and diode the percentage share of total switching losses, which is independent of switching frequency. As IGBT module voltage rating increases, the losses increases and devices are more sensitive to increase in switching frequency.

Table 4.6: IGBT and diode percentage contribution to total switching losses.

IGBT module	P _{sw(T)}	P _{sw(D)}
6.5 kV	74 %	26 %
4.5 kV	66 %	34 %
3.3 kV	59 %	41 %

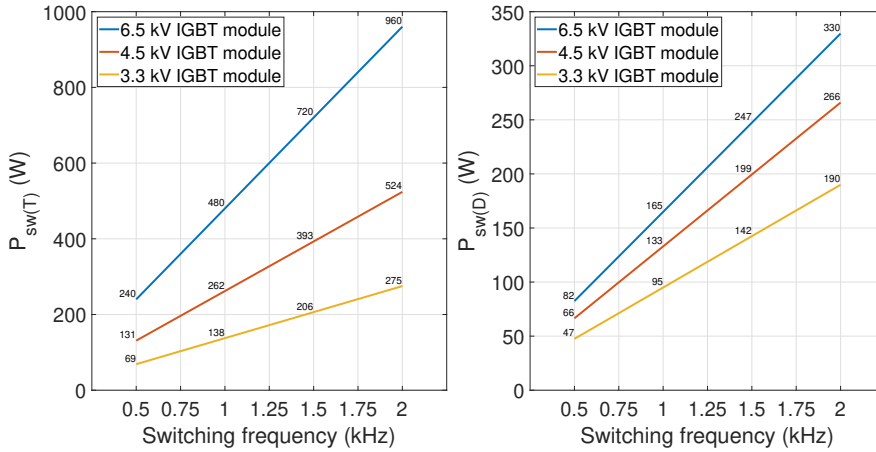


Figure 4.4: IGBT $P_{sw(T)}$ (left figure) and diode $P_{sw(D)}$ (right figure) switching losses for the IGBT modules as a function of frequency.

Figure 4.5 show conduction losses for the three IGBT modules. Table 4.7 presents IGBT and diode percentage contribution to total conduction losses. It becomes evident that IGBT conduction losses are negligible and switching losses are the main contributor to losses. As an example, at 1.0 kHz switching frequency, 85 % of total losses are related to switching losses for the 6.5 kV module.

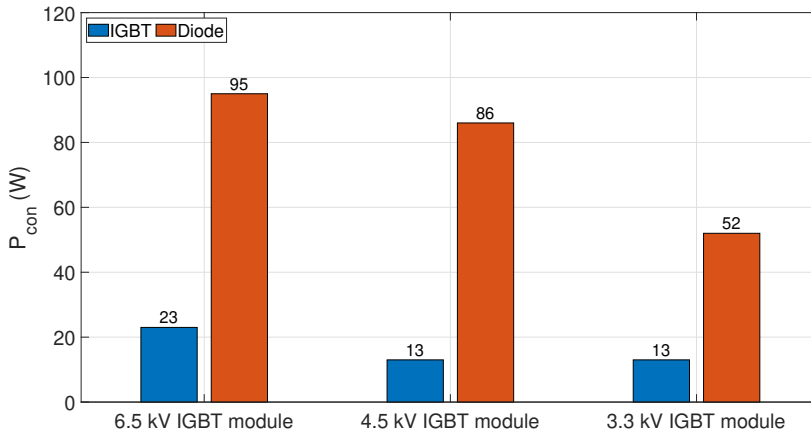


Figure 4.5: IGBT $P_{con(T)}$ and diode $P_{con(D)}$ conduction losses for the three modules.

Total losses and converter system efficiency are presented in Figure 4.6. Tabular result to efficiency is given by Table 4.8. The results show that the 3.3 kV module secures highest

Table 4.7: Conduction losses percentage distribution.

IGBT module	$P_{con(T)}$	$P_{con(D)}$
6.5 kV	20 %	80 %
4.5 kV	13 %	87 %
3.3 kV	20 %	80 %

efficiency. The 6.5 kV module is slightly more efficient than the 4.5 kV module at 0.5 kHz. However, due to switching losses sensitivity to switching frequency, the efficiency decreases faster compared to the other modules.

Table 4.8: Converter system efficiency η tabular results.

IGBT module	$f_{sw}=0.5$ kHz	$f_{sw}=1.0$ kHz	$f_{sw}=1.5$ kHz	$f_{sw}=2.0$ kHz
6.5 kV	99.2 %	98.5 %	97.9 %	97.3 %
4.5 kV	99.1 %	98.6 %	98.0 %	97.4 %
3.3 kV	99.3 %	98.9 %	98.4 %	98.0 %

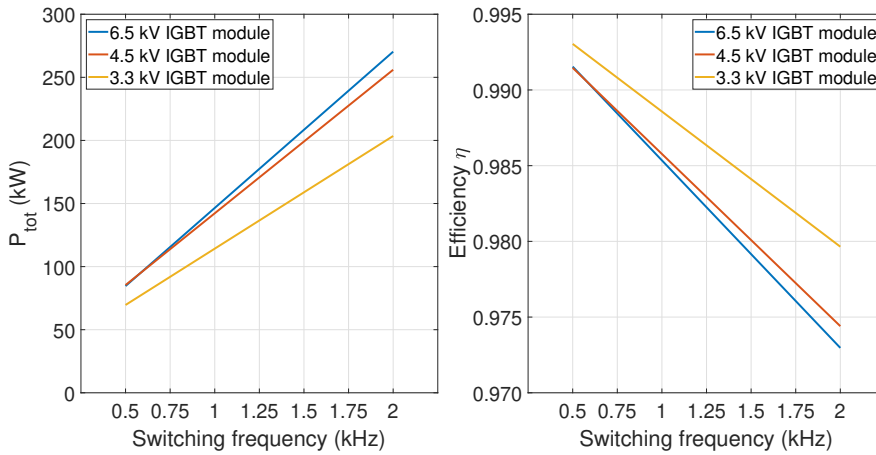


Figure 4.6: Total power losses $P_{tot,2L}$ (left figure) and efficiency η (right figure) as a function of switching frequency.

4.3.2 3L-NPC

Figure 4.7 presents switching losses for the various symmetrical devices in the converter. Table 4.9 show device percentage contribution to total switching losses. The result show that switching losses are related to IGBT T2 and T3 in addition to diode D1 and D4. These devices switching losses are close to 2L-VSC IGBT and diode switching losses, which coincide with the analytical models.

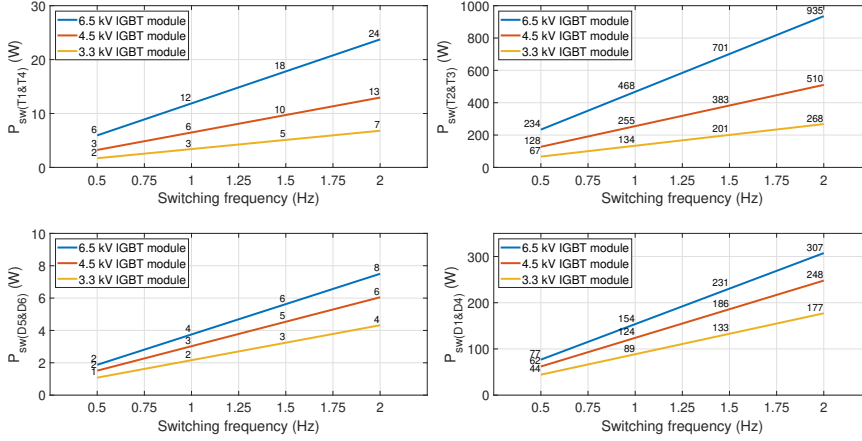


Figure 4.7: Switching losses for the various devices as a function of switching frequency.

Table 4.9: Device switching loss relative contribution to total switching losses.

IGBT Module	$P_{sw}(T1\&T4)$	$P_{sw}(T2\&T3)$	$P_{sw}(D5\&D6)$	$P_{sw}(D1\&D4)$	$P_{sw}(D2\&D3)$
6.5 kV	2 %	73 %	1 %	24 %	0 %
4.5 kV	2 %	66 %	1 %	32 %	0 %
3.3 kV	1 %	59 %	1 %	39 %	0 %

Conduction losses and device percentage contribution to total conduction losses are presented in Figure 4.8 and Table 4.10. Except for IGBT T1 and T4, conduction losses distributes differently than switching losses. As with the 2L-VSC, IGBT conduction losses are small compared to diode losses. Opposite to the 2L-VSC, conduction losses contribute more to total losses. For the 6.5 kV module at 1.0 kHz switching frequency, switching losses is 72 % of the total, compared to 85 % in the 2L-VSC.

Table 4.10: Conduction losses percentage distribution.

IGBT Module	$P_{con}(T1\&T4)$	$P_{con}(T2\&T3)$	$P_{con}(D5\&D6)$	$P_{con}(D1\&D4)$	$P_{con}(D2\&D3)$
6.5 kV	0 %	24 %	15 %	31 %	31 %
4.5 kV	0 %	13 %	17 %	35 %	35 %
3.3 kV	0 %	21 %	15 %	32 %	32 %

Total losses and efficiency as a function of switching frequency are presented in Figure 4.9. Efficiency tabular result is presented in Table 4.11. The results applies for eight modules ($N = 8$). The 6.5 and 3.3 kV module results are independent of the configurations with the chosen method in this calculation. The other configuration with 16 modules lead to a lower efficiency for the 4.5 kV module. The results with 16 modules are found in Table

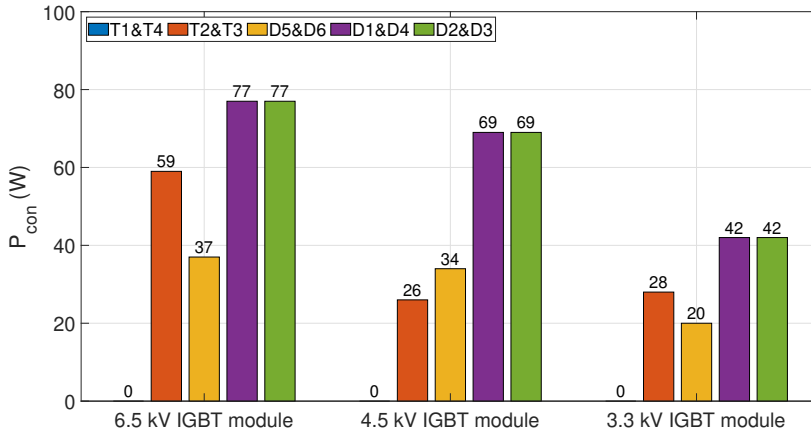


Figure 4.8: Conduction losses for the various devices.

A.13 in the appendix.

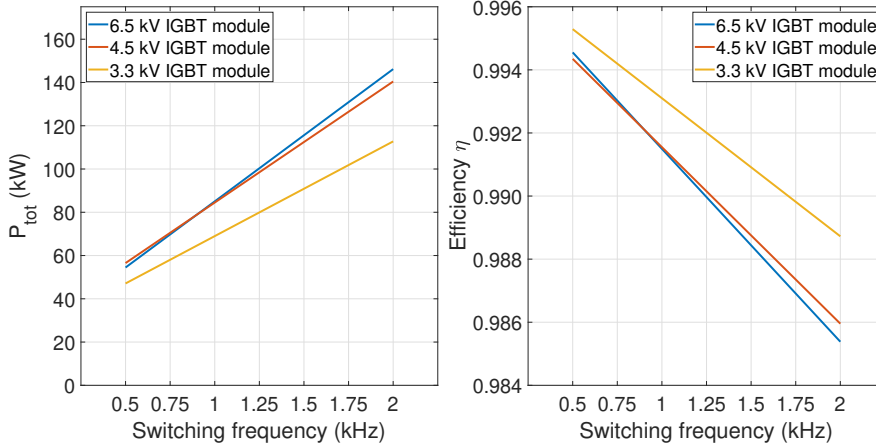


Figure 4.9: Total power losses $P_{\text{tot},3L}$ (left figure) and efficiency η (right figure) as a function of switching frequency.

As with the 2L-VSC the lowest voltage rated module leads to highest efficiency. However, the deviation between 6.5 kV module to the 3.3 kV module are lower than for the 2L-VSC. Additionally, the efficiency are higher for all modules and frequency. All modules provide efficiency over 99 % at 1.0 kHz or lower.

Table 4.11: Converter system efficiency η tabular results.

IGBT module	$f_{sw}=0.5$ kHz	$f_{sw}=1.0$ kHz	$f_{sw}=1.5$ kHz	$f_{sw}=2.0$ kHz
6.5 kV	99.5 %	99.1 %	98.8 %	98.5 %
4.5 kV	99.4 %	99.2 %	98.9 %	98.6 %
3.3 kV	99.5 %	99.3 %	99.1 %	98.9 %

4.4 Outcome of calculation

The results in chapter 4.3 show semiconductor losses in the 2L-VSC and 3L-NPC converter. The system set-up and method are presented in chapter 4.2 and the analytical models are seen in chapter 4.2.7.

For both converters, applying the 3.3 kV IGBT module leads to higher system efficiency than for higher voltage rated modules. This is in-line with other researchers results found in literature [27],[45].

The 3L-NPC converter has higher efficiency for all IGBT modules and all frequencies compared to the 2L-VSC. Numerical values are given in Table 4.8 and Table 4.11. That result also corresponds to other researchers results [45],[47]. The 3L-NPC converter can achieve above 99 % efficiency for all modules when switching frequency is limited to 1.0 kHz.

Based on the outcome of this calculation, relevant simulations in chapter 5 will be performed with a 3.3 kV IGBT module since this module features the lowest losses. Switching frequency will set to 1.0 kHz, where efficiency is kept at 98.9 % and 99.3 % for the 2L-VSC and 3L-NPC converter respectively in nominal operation. This is considered an acceptable efficiency and the frequency could be used in future research for converters for this 10 MW application [19, p. 107].

System simulation

5.1 Simulation setup

The simulation is conducted in Simulink. The number of generator/converter modules are limited to two ($N = 2$) in order to have multiple modules while at the same time minimize computational effort. The parameter values are based on an eight segment configuration where two modules are implemented, see Figure 5.1 for an illustration and appendix chapter A.4.1 for parameter values to various system components.

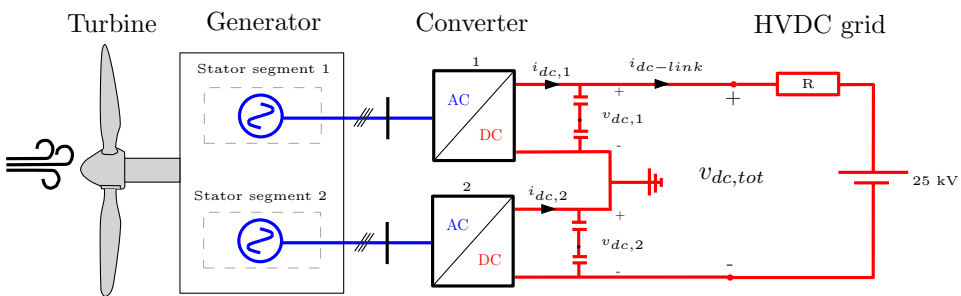


Figure 5.1: Simulation setup.

Wind speed: The wind speed input to the system is given by Figure 5.2.

This stair-case form will test the system for various wind speeds where both acceleration and deceleration occurs. Certain analyses such as power quality and converter losses will be evaluated discretely for each step, not as a continuous function.

Wind turbine: The turbine is Simulink's library wind turbine model [33]. As discussed in chapter 2.5, pitch angle are kept zero for all operation. Turbine parameter values are given in appendix in Table A.14.

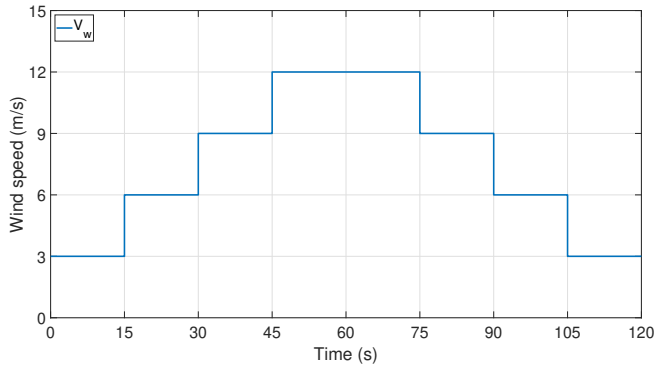


Figure 5.2: Wind speed input.

Segmented PMSG: The developed model of a segmented PMSG seen in appendix chapter A.2.3 will be used. Two segments are included in the simulation. Table A.15 provide numerical values to various parameters.

Power converters: Simulink power converter models [48][49] with parameter values given in Table A.16 are used in performance analysis. For simulating losses, a dedicated converter model is used, see appendix chapter A.4.2 for details on this model. The parametrization given in the mentioned table is equal in all cases.

Control system: System structure is presented in chapter 2.7 and associated tuning in appendix chapter A.2.4. To be noted is that the DC-bus voltage controller is inactive in all analysis that does not concern this directly.

HVDC grid: The HVDC grid is adapted to the mentioned configuration. This means that the stiff DC-voltage source is 25 kV. See Table A.17 for cable resistance.

Loss model: Description of the simulation model for simulating power losses are found in appendix chapter A.4.2. Based on the results in chapter 4, the converters are equipped with a 3.3 kV IGBT module. The module is a 250 A/3.3 kV half-bridge IGBT module from ABB [50]. It is used as Mathworks provide a library model of this module, such that required forward and switching characteristics are easily available. Comparison between module losses in the simulation model and the analytical models seen in chapter 4.2.7 are found in appendix chapter A.4.3.

Segmented PMSG parameter variation: Three DC-bus voltage controller strategies presented in chapter 3.4 are tested by enforcing a variation between the two segments. The flux linkage in segment one is 1.05 pu, while the other is 0.95 pu. The converters are ideal and stator resistance are equal for both segments. Expected voltage variation are presented in Table A.20. The 3L-NPC converter are used in the simulation.

5.2 Simulation results

5.2.1 Comparison of state variables

This chapter presents the state variables i_q , i_d , v_{c1} , v_{c2} for converter 1 and the common ω_r state variable when using a 3L-NPC converter and 2L-VSC. Figure 5.3 and Figure 5.4 show the respective results. The results show that the system is stable, as all state variables reaches a steady state value corresponding to the reference value for both converter types.

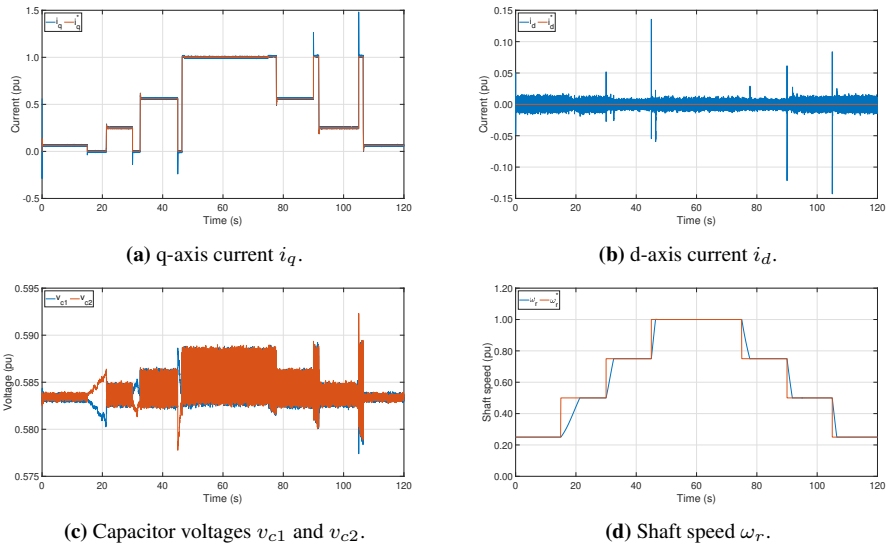


Figure 5.3: State variables with 3L-NPC converter.

Both the d and q-axis current show considerable oscillation during a step change, such as at 105 seconds. The peak value of the oscillation are greater in the 3L-NPC converter than in the 2L-VSC. The oscillation could be related to controller tuning method, but might also be coupled to other state variables. Revised tuning method and/or reduction of proportional constants can reduce the oscillations. However, the results is acceptable for the purpose of this investigation. The peak value difference between the converters might be due to the capacitor voltages and associated controller, but remains to be investigated. For the 3L-NPC converter, both capacitor voltages are kept within an acceptable deviation and neutral point drift is negligible. Capacitor voltages in the 2L-VSC are identical at all times as they operate effectively as a single capacitor that charges/discharges equally. Shaft speed dynamic are slower than the other state variables due to the system inertia.

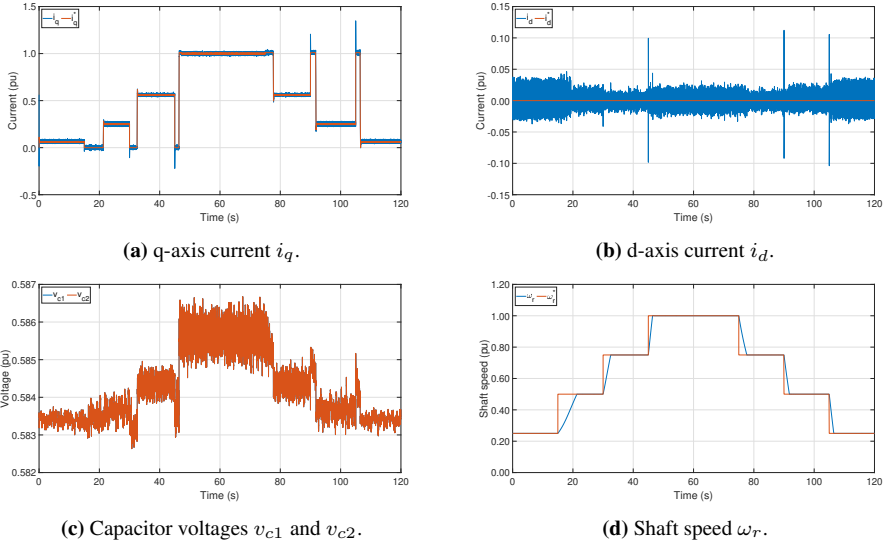


Figure 5.4: State variables with 2L-VSC.

5.2.2 Waveform comparison

Phase current

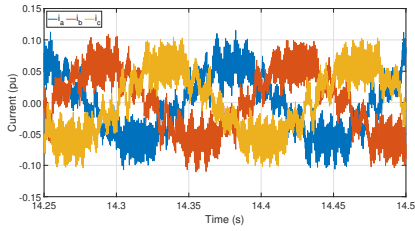
The 3L-NPC converter and 2L-VSC phase currents i_{abc} are presented in Figure 5.5 and Figure 5.6 respectively. These figures show steady state waveform of all three phase currents for all four wind speed steps.

For all wind speeds, the 3L-NPC converter waveforms are observably less distorted when compared to the 2L-VSC. This observation will be quantified in chapter 5.2.3, when the harmonic content of the currents will be measured. The 3L-NPC converter features a voltage balancing controller. This could potentially distort the phase currents in order to keep the neutral-point voltage from drifting. However, it can be observed that neither the neutral point is drifting in Figure 5.4c and the phase current seems marginally affected by the controller.

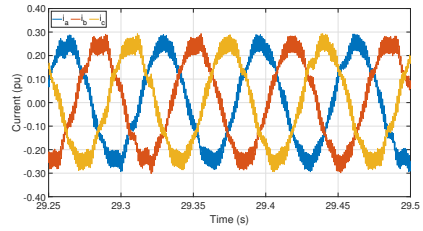
Line-to-line voltage

Figure 5.7 and Figure 5.8 show one (v_{ab}) of three line-to-line voltages for the 3L-NPC converter and 2L-VSC.

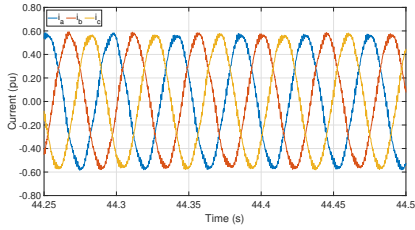
The 3L-NPC converter line-to-line voltage are considerably reduced at 3 and 6 m/s wind speed compared to 9 and 12 m/s. Both amplitude and number of levels are reduced. It indicated that the phase voltages v_a and v_b are modulated such that the states are not 1 and -1 simultaneously, which is required to obtain the shape seen in Figure 5.7c and Figure 5.7d. It might imply that the modulation index must reach a certain threshold for this to be



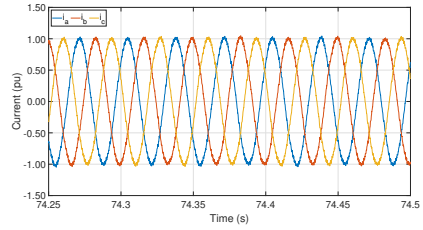
(a) i_{abc} at $V_w=3$ m/s.



(b) i_{abc} at $V_w=6$ m/s.

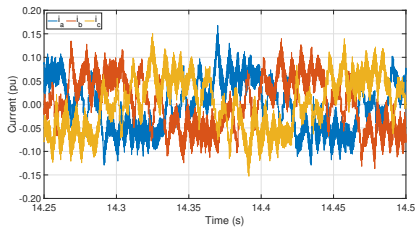


(c) i_{abc} at $V_w=9$ m/s.

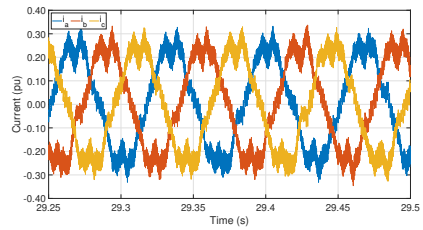


(d) i_{abc} at $V_w=12$ m/s.

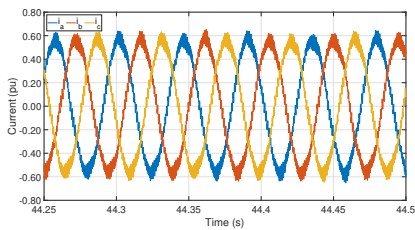
Figure 5.5: Steady state phase current i_{abc} with the 3L-NPC converter.



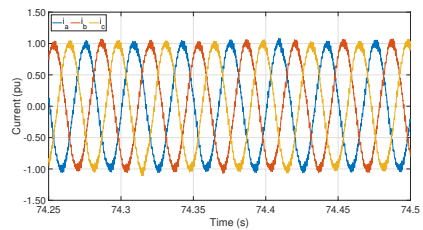
(a) i_{abc} at $V_w=3$ m/s.



(b) i_{abc} at $V_w=6$ m/s.



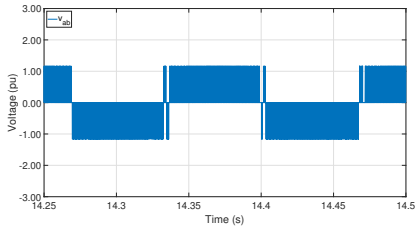
(c) i_{abc} at $V_w=9$ m/s.



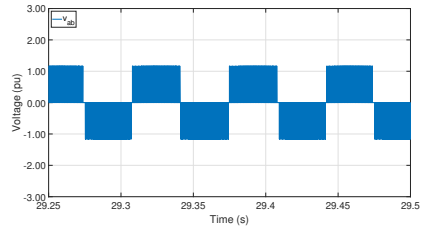
(d) i_{abc} at $V_w=12$ m/s.

Figure 5.6: Steady state phase current i_{abc} with the 2L-VSC.

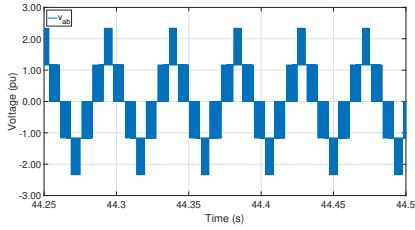
true. The 2L-VSC does not have this multilevel characteristic, and the line-to-line voltage are in amplitude and number of levels equal for all wind speed. In chapter 5.2.3, a power quality analysis of both line-to-line voltages are performed.



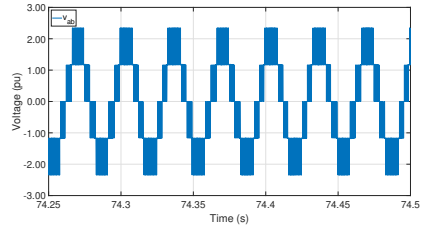
(a) v_{ab} at $V_w=3$ m/s.



(b) v_{ab} at $V_w=6$ m/s.

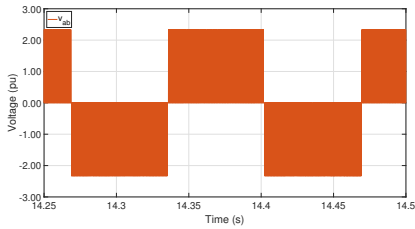


(c) v_{ab} at $V_w=9$ m/s.

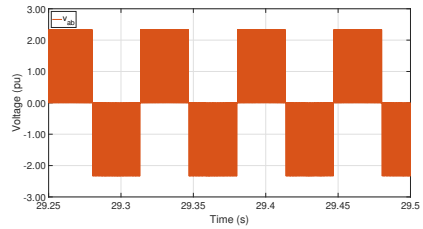


(d) v_{ab} at $V_w=12$ m/s.

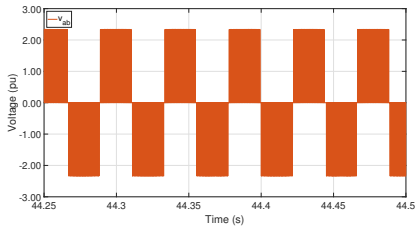
Figure 5.7: Steady state line-to-line voltage v_{ab} with the 3L-NPC converter.



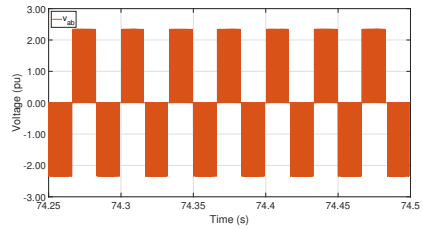
(a) v_{ab} at $V_w=3$ m/s.



(b) v_{ab} at $V_w=6$ m/s.



(c) v_{ab} at $V_w=9$ m/s.

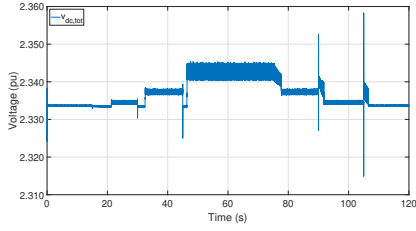


(d) v_{ab} at $V_w=12$ m/s.

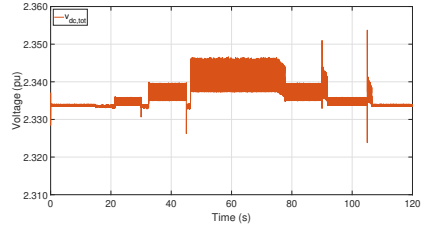
Figure 5.8: Steady state line-to-line voltage v_{ab} with the 2L-VSC.

DC-link voltage and current

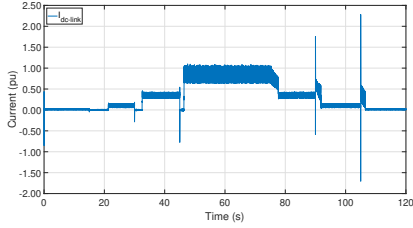
The DC-link voltage $v_{dc,tot}$ and current $i_{dc-link}$ are shown for both converters in Figure 5.9.



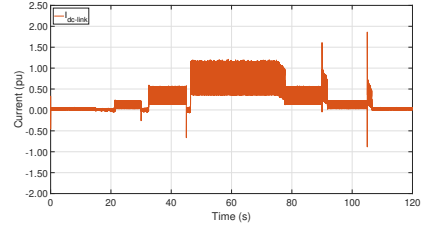
(a) $v_{dc,tot}$ with 3L-NPC converter.



(b) $v_{dc,tot}$ with 2L-VSC.



(c) $i_{dc-link}$ with 3L-NPC converter.



(d) $i_{dc-link}$ with 2L-VSC.

Figure 5.9: DC-link voltage and current for both converters. Full simulation course.

The results show that the ripple in DC-link current is considerably reduced with the 3L-NPC converter compared to the 2L-VSC. This propagates to the DC-link voltage due to the modelling of a constant DC-source and a resistor as HVDC grid. Table 5.1 show the ripple for both converters for all four wind speeds. The ripple $\Delta i_{dc-link}$ is calculated as the difference between the maximum and minimum value of the current over a 5 second period in steady state.

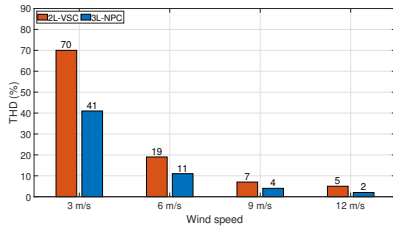
Table 5.1: DC-link current ripple $\Delta i_{dc-link}$ in per unit for all wind speeds and both converters.

V_w	2L-VSC	3L-NPC
3 m/s	0.059	0.034
6 m/s	0.197	0.103
9 m/s	0.439	0.158
12 m/s	0.843	0.434

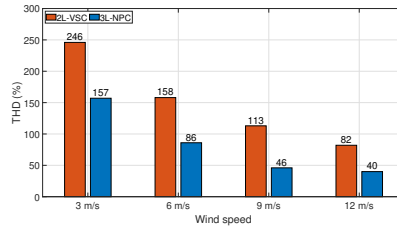
The observed dq-axis current oscillation right after a step change is also observable in the DC-link current and is greater for the 3L-NPC converter compared to the 2L-VSC.

5.2.3 Comparison of power quality

The power quality investigation is limited to measurement of total harmonic distortion (THD) in AC-side phase current and line-to-line voltage. This will quantify the observations made in the waveform analysis. The results are seen in Figure 5.10 where the THD is given in percentage.



(a) THD in i_{abc} .



(b) THD in v_{ab} .

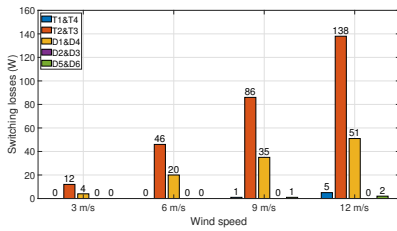
Figure 5.10: THD in phase current and line-to-line voltage for both converters and various wind speeds.

In accordance to the observations in Figure 5.5-5.8, the THD are greater for lower wind speeds for both current and voltage. Additionally the current is less distorted than the voltage and the 3L-NPC converter feature lower THD than the 2L-VSC. For both current and voltage, the THD are reduced in all cases.

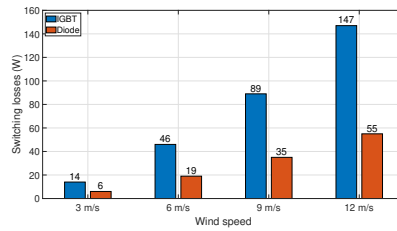
5.2.4 Converter loss comparison

Switching and conduction losses

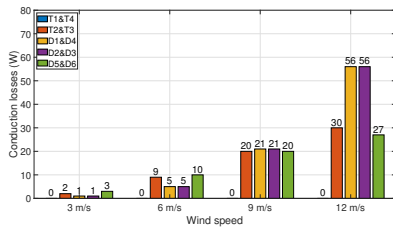
Figure 5.11 show switching and conduction losses with the two converters.



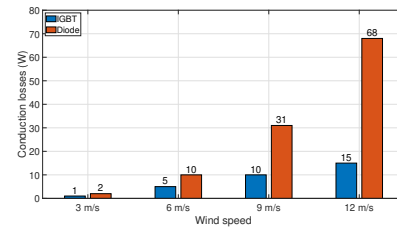
(a) Switching losses 3L-NPC.



(b) Switching losses 2L-VSC.



(c) Conduction losses 3L-NPC.



(d) Conduction losses 2L-VSC.

Figure 5.11: Switching and conduction losses in the 3L-NPC converter and 2L-VSC.

The 3L-NPC converter switching losses is approximately only related to IGBT T2 and T3 and diode D1 and D4. For the 2L-VSC, switching losses are dominated by the IGBT. For

both converters, IGBT and diode switching losses makes up roughly 70 % and 30 % of total switching losses for all wind speeds. The conduction losses takes up a greater share of total losses in the 3L-NPC converter compared to the 2L-VSC. Conduction losses share of total losses are 26 % and 46 % for at 3 and 12 m/s wind speed respectively with the 3L-NPC. This is reduced to 13 % and 29 % with the 2L-VSC.

Junction temperatures

The junction temperatures in the various semiconductor devices in both converters are presented in Figure 5.12. The results show how the uneven loss distribution in the 3L-NPC converter leads to a 20 °C difference between the hottest and coldest semiconductor junction. This is one of the disadvantages of this converter, as the converter and its associated cooling system must be rated for the maximum temperature in that single device. Temperature discrepancy between semiconductor die junctions are limited to 8 °C in the 2L-VSC, but the temperatures are higher in this converter. This is due to higher losses, while system set-up including cooling system are equal for both converters.

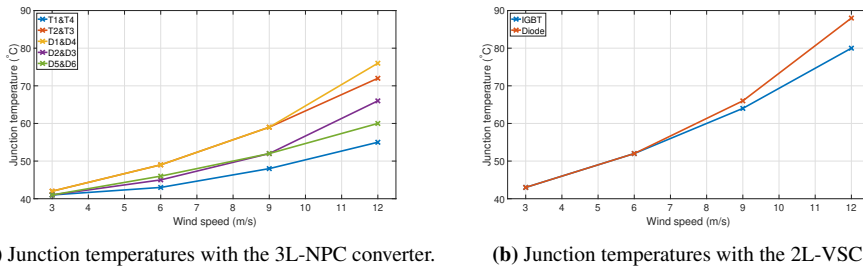


Figure 5.12: Semiconductor junction temperatures for both converters.

Efficiency

The total losses and efficiency for both converters are presented in Table 5.2. As in chapter 4, when calculating efficiency, an ideal power transfer is assumed. For this system, the input power to each converter is 1.25 MW. Total converter system AC-side input power is 2.5 MW at rated wind speed. Comparison to results in chapter 4 are possible by the relative measure of efficiency or by multiplying total power losses by 4. The cubed relationship between power and wind speed as given in chapter 2.5 is assumed to hold.

Table 5.2: Total losses and efficiency with both converters.

V_w	P_{tot} 3L-NPC	η 3L-NPC	P_{tot} 2L-VSC	η 2L-VSC
3 m/s	1.0 kW	97.4 %	2.2 kW	94.3 %
6 m/s	4.6 kW	98.5 %	7.7 kW	97.5 %
9 m/s	9.8 kW	99.1 %	15.8 kW	98.5 %
12 m/s	17.4 kW	99.3 %	27.4 kW	98.9 %

Based on the four data-points in Table 5.2, an approximation of the total losses can be performed. Equation (5.1) is used to estimate total power losses for all wind speeds in the range from 3 m/s to 12 m/s for both converters. Table 5.3 show the associated constants numerical value.

$$P_{tot} = a \cdot (V_w)^b \quad (5.1)$$

Table 5.3: Constants for approximation of total losses as a function of wind speed and associated coefficient of determination (R^2).

Constant	2L-VSC	3L-NPC
a	0.3009	0.1133
b	1.81	2.034
R^2	0.9992	0.9999

The efficiency of both converters as a function of wind speed can now be approximated by equation (5.2).

$$\eta = 1 - \frac{P_{tot}}{P_{in}} = 1 - \frac{a \cdot (V_w)^b}{2500 \cdot \left(\frac{V_w}{12}\right)^3} \quad (5.2)$$

The valid range of this formula can be extended from an upper limit of 12 to 24 m/s by assuming that the efficiency is constant in turbine operation region 3. Figure 5.13 show the efficiency for both converters as a function of wind speed in the range from 3 to 24 m/s.

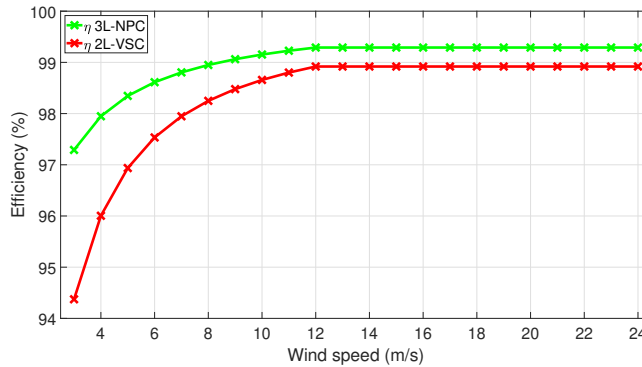


Figure 5.13: Efficiency as a function of wind speed for both converters.

The result show that the 3L-NPC converter have higher efficiency than the 2L-VSC for all wind speeds. Efficiency deviation is greatest at lowest wind speed and decreases as the wind speed increases. In order to describe the effect of this results, a weighted average efficiency $\bar{\eta}$ is introduced.

The weighted average efficiency is calculated by combining the wind speed distribution, AC-side input power and converter efficiency as a function of wind speeds in turbine operation region 2 and 3. The product of the wind speed distribution and the AC-side input

power are used as the weight. The combination of these are seen in Figure 5.14a. The combination of converter efficiency and the wind speed distribution are presented in Figure 5.14b.

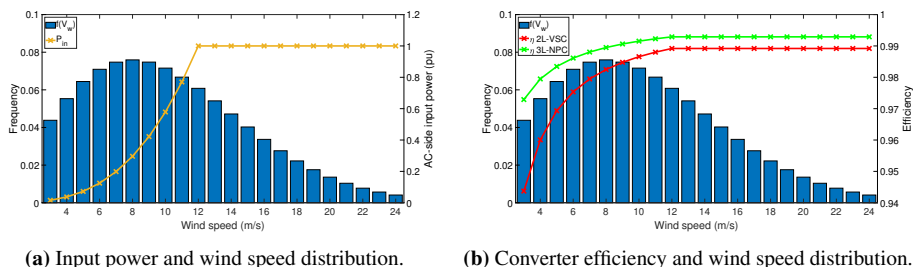


Figure 5.14: The AC-side input power, converter efficiency and the discretized wind speed distribution in turbine operation region 2 and 3.

Equation (5.3) show the mathematical expression for the weighted average efficiency and Table A.27 in appendix show the input data.

$$\bar{\eta} = \frac{\sum_{V_w=3}^{24} P_{in}(V_w) \cdot f(V_w) \cdot \eta(V_w)}{\sum_{V_w=3}^{24} P_{in}(V_w) \cdot f(V_w)} \quad (5.3)$$

The resulting weighted average values are given by Table 5.4. The result show that the 3L-NPC converter has a 0.5 % higher weighted average efficiency compared to the 2L-VSC. Set in context, for a 10 MW wind turbine as modelled in this thesis, 0.5 % weighted efficiency translates to 210 MWh/year. As a note, this is roughly one sixth of potential differences related to control methods seen in chapter 3.3.

Table 5.4: Resulting converter weighted average efficiency.

Converter	$\bar{\eta}$
2L-VSC	98.7 %
3L-NPC	99.2 %

The result in Table 5.4 show that studying efficiency for only nominal operation as conducted in chapter 4, is a good indicator of weighted average efficiency. The weighted average efficiency is 0.1 % lower for the 3L-NPC converter and 0.2 % lower for the 2L-VSC compared to efficiency at nominal wind speed.

5.2.5 DC-bus voltage controller strategies

Three of four DC-bus voltage controller strategies presented in chapter 3.4 are tested in this simulation. These are presented as three strategies; strategy 1 (Str 1), strategy 2 (Str

2) and strategy 3 (Str 3).

The first strategy excludes the DC-bus voltage controller and the DC-bus voltages are unregulated. The second strategy is controlling the DC-bus voltage to be equal for both converters without lowering power output. The third strategy is controlling the DC-bus voltage to be equal, but power is derated in order to avoid overloading of generator/converter module 2. Figure 5.15 show the resulting q-axis currents $i_{q,i}$, DC-bus voltage in relation to the average DC-bus voltage $\frac{v_{dc,i}}{v_{dc,avg}}$ and the DC-link power $p_{dc-link}$.

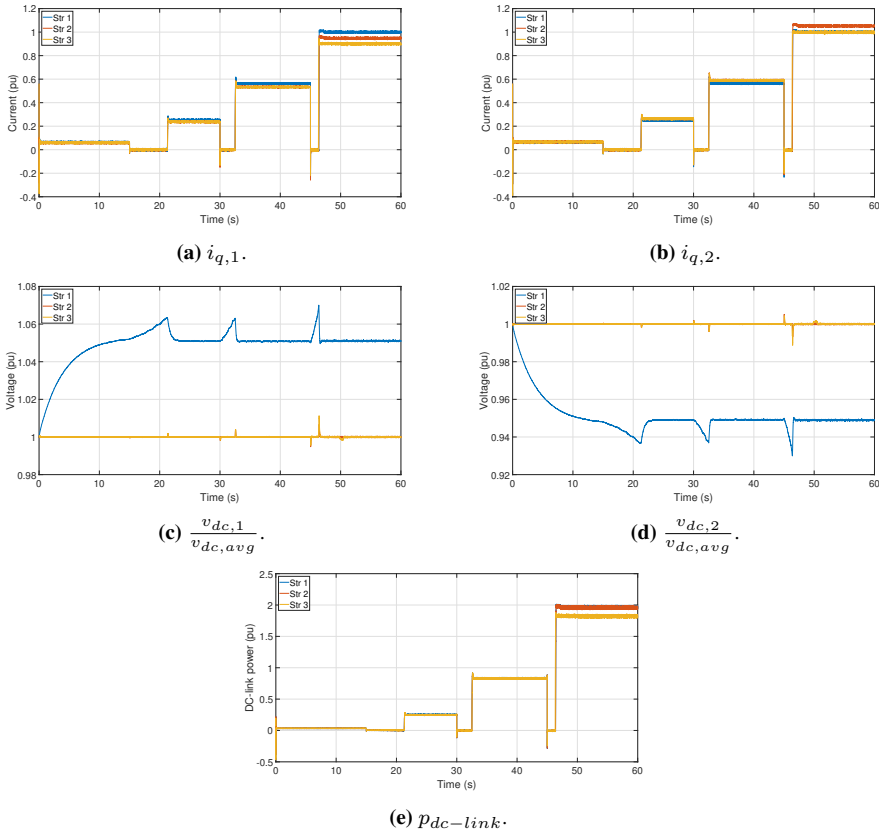


Figure 5.15: Q-axis currents, DC-bus voltages and DC-link power for three DC-bus voltage controller strategies.

With strategy one, both q-axis current are identical as if both generator/converter modules were equal. The difference are seen in DC-bus voltage. Module one DC-bus voltage deviates roughly 5 % to the average DC-bus voltage, while module two deviates by roughly -5 % in steady state. The observed oscillation during step changes can also be observed in the dc-bus voltages, the peak voltages are roughly 7 % and -7 %. The power however, are unaffected by the DC-bus voltage balancing.

Strategy two leads to balanced voltages, but as seen in Figure 5.15b, the q-axis current in module two is approximately 1.05 pu. In SI-units, this corresponds to 8 A overloading. The power remain approximately unaffected, but a slight reduction are observed. This could be due to stator losses quadratic relationship to current, but remains to be investigated.

The final strategy keeps the voltages balanced and avoids q-axis overloading, but the power is reduced at nominal operation. Table 5.5 show the mean value of DC-link power during steady state at nominal operation.

Table 5.5: Mean of DC-link power in time interval $50 \leq t \leq 60$.

Strategy	$p_{dc-link}$	$P_{dc-link}$
1	1.962 pu	2.453 MW
2	1.956 pu	2.445 MW
3	1.819 pu	2.274 MW

The result in Table 5.5 show that strategy one has the highest power output. The difference with respect to strategy two can be due to the increase in current leads to an increase in resistive losses in the PMSG segment, but remains to be investigated. Comparing strategy one and three, leads to a difference in 0.179 MW. As stated in chapter 3.4, the purpose of these results are not to conclude optimal DC-bus voltage controller strategy, but rather show difference and inspire future work.

5.3 Summary of simulation results

The results in Figure 5.3 and Figure 5.4 show that the system in question can be stabilized when using both the 2L-VSC and 3L-NPC converter. The results showed oscillation in dq-axis currents that might be related to controller tuning. Neutral point voltage showed no sign of drifting with the 3L-NPC converter, which could be a challenge with this converter. The 2L-VSC has self-balanced capacitors for this system. The shaft speed state variable showed a considerable slower behaviour than the other states. This is due to the mechanical time constant of this system, compared to the time constants related to the inductance and capacitance in dq-axis AC-side current and DC-side voltage.

The waveform comparison showed that the 3L-NPC converter phase currents was not distorted by adding the capacitor voltage balancing control. For all four wind speeds, the AC-side current was less distorted with a 3L-NPC converter than with a 2L-VSC. The 3L-NPC converter line-to-line voltage shows different behaviour compared to the 2L-VSC, due to the multilevel function. At lower wind speeds, the line-to-line voltage amplitude is reduced, but only two levels are active. When the wind speed increases, the three-level characteristic shape becomes visible. With the 2L-VSC, the line-to-line voltage are identical at all times, in terms of number of levels and amplitude. Finally, the DC-link voltage and current was studied. The results showed that the ripple in DC-link current was almost

reduced to half with the 3L-NPC compared to the 2L-VSC for all four wind speeds. The ripple increases as wind speed increases and its maximum occurs at nominal speed.

The power quality analysis showed that the current and line-to-line voltage THD are roughly reduced to half for all four studied wind speeds, when using the 3L-NPC converter compared to the 2L-VSC.

The converter loss comparison showed that the 3L-NPC converter switching losses are limited to IGBT T2&T3 and diode D1&D4. Conduction losses make up a greater share of total losses compared to the 2L-VSC and the losses are lower than with the 2L-VSC. The characteristic loss distribution in the 3L-NPC converter leads to a great variation in semiconductor junction temperature, as the difference between the diode D1&D4 junction temperature and IGBT T1&T4 junction temperature was 20 °C. This is limited to 8 °C in the 2L-VSC. At the same time, the maximum temperature was higher in the 2L-VSC (diode 88 °C), while diode D1&D4 was limited to 76 °C. An extensive calculation process led to the result of weighted average efficiency for both converters. The result showed that the 3L-NPC converter have a 0.5 % higher weighted average efficiency compared to the 2L-VSC.

Three different DC-bus voltage controller strategies were tested in chapter 5.2.5. The results show how these differs in q-axis current, DC-bus voltage and system output power. When the DC-bus voltage controller is inactive, the current remains as presented in the state analysis, but the DC-bus voltages starts deviating to the desired value. The deviation is compensated by increasing/decreasing the q-axis current freely in strategy two. This leads to overloading of module two in nominal operation, but the output power remains unaffected. Strategy three limits q-axis current to maximum 1.0 pu. This does not influence the system prior to nominal operation. However, at rated wind speed, the power output is decreased in order to keep module two from overloading.

Discussion

6.1 Selection of power converters

This thesis limited the scope of power converters to only study the 3L-NPC converter and use the 2L-VSC for comparison based on previous research in the specialization project [16]. The mentioned converters are well-known and commonly used in industry. However, many converters that might be interesting to study are overlooked. It is acknowledge that e.g. the five-level or even higher level MMC could be very suitable for this application as a multilevel converter. This is one option of converters to avoid series connection of 3.3 kV IGBT modules with the calculation method of series-connection requirements as given chapter 2.4. Additionally, power quality would be better with a higher level converter, such that filter requirements might be less restrictive. At the same time, such a converter might feature more complex circuitry and control compared to the two studied converters in this thesis. Additionally, the efficiency and reliability of such a system remains to be investigated.

A wide variety of three-level converters also exist. Of special interest could be the three-level active neutral point clamped (3L-ANPC) converter. This topology is derived from the 3L-NPC with the aim of lower or balance the losses more equally between components. It does so by replacing the clamping diodes by IGBTs and adding adequate switching strategies. The benefit of a better loss distribution is smaller differences between semiconductor junction temperatures as seen in Figure 5.12a. This could be beneficial in terms of converter reliability and lifetime [47, Tab. VIII]. This converter could have been included in this study, but at the same time, it might be too similar to the 3L-NPC. Study of 3L-ANPC and 5L-MMC or higher level MMC and how they compare to the results obtained in this thesis are recommended as future work.

6.2 DC-bus voltage controller analysis

The case study in chapter 3.3 parameterized eight modules by using normal distributed parameters. The validity of the parameters value and standard deviation in a real machine might be low. Coupled dependencies between variables, dynamic operation influence to the parameters such as temperature influence and positive/negative feedback effects and other aspects might be overlooked, such that the parameters are unrealistic. As shown in chapter 5.2, converter efficiency variation ranging from 96.5 % to 99 % as used in the case study, might not be true for two converters with approximately equal voltage and current and no faults. Therefore, the results and observation of expected steady state DC-bus voltage variation of ± 5 % might be conservative.

The evaluated strategies for compensating DC-bus voltage difference did only considered the converters electrical aspects of changing q-axis current and thus associated torque and power. Any effects of the control strategies to the generator are not considered. This might provide new insight that changes preconditions for the analysis, e.g. by mechanical aspects due to the segmented stator. Additionally, the losses in a stator segment was limited to the electrical losses by stator resistance. Also magnetic losses and stray losses could be accounted for in a more complete analysis [51, p. 34].

6.3 Converter and IGBT module loss calculation

In chapter 4 the two converters losses with three different IGBT modules were studied for switching frequency range 0.5-2.0 kHz. Losses were calculated by the aid of analytical models detailed in chapter 4.2.7.

The potential power semiconductor technologies to be used in wind power applications are typically IGBT modules, IGBT press-pack packages and Integrated Gate Commutated Thyristor (IGCT) press-pack packages [19, p. 26]. In this calculation, the selection was limited to IGBT modules. Unforeseen benefits with IGBT and IGCT press-pack packages for this application might be overlooked and could be studied further. However, at least for ABBs portfolio, the current ratings of the IGBT and IGCT press-pack packages might be too extensive to for this application, as the current are limited to only 110 A RMS. Semiconductor manufacturer selection might not be limited to ABB in future work. Multiple options exist, such as Infineon, Mitsubishi and Hitachi products could be alternatives to the modules presented. ABB was chosen based on their selection of components, industrial status and for ease of comparison between various modules. Comparing modules between manufacturers might introduce additional uncertainty as their tests methods for obtaining datasheet values might vary [44]. Experimental results with a dedicated lab setup might be required for comparing modules.

The analytical models uses compensation factors for current, voltage and temperature difference to reference values. There are numerous associated uncertainties, such as the value of current, voltage and temperature compensation factors constants. Additionally, the models might represent experimental results better for certain intervals of current and

voltage. As an example, the peak value of current in this application is only 39 %, 24 % and 20 % of the 6.5, 4.5 and 3.3 kV IGBT modules reference current respectively. If the analytical calculation models are a good representation for this discrepancy between actual and reference current remains to be investigated. It could be that the 3.3 kV proves more efficient, since the difference between reference and actual current are greater compared to the 4.5 and 6.5 kV module. However, analytical model and simulation model results for the 250 A/3.3 kV IGBT module used in chapter 5 gave results that corresponds well, see appendix chapter A.4.3. At the same time, this is a 250 A IGBT module, where the reference current is closer to the peak value application current. Future work could be to further investigate differences between various IGBT modules.

Comparing IGBT modules based on their datasheet values can introduce extra uncertainty. As an example, application specific values such as stray inductance and gate resistance might influence reference switching losses. The studied IGBT modules have all different stray inductance, gate resistance and the 4.5 kV module uses a gate-emitter capacitor. These are all factors that contribute to uncertainties, when comparing the devices based on datasheet values.

Potential risks of extensive series-connections of semiconductors, possible extra control and hardware additions such as delay functions and snubber circuits are overlooked. It might be that using a 6.5 kV module is more convenient and maybe even more efficient in a 16 segment configuration than using 3.3 kV modules in e.g. an 8 segment configuration. The former avoids series-connection of devices in a 3L-NPC converter while the latter would lead to four devices in series. More insight to the challenge of series-connecting IGBT modules might be required for future design choices if three-level converters are still to be evaluated.

6.4 System simulation

In chapter 5, simulation results were obtained for comparing performance of a 2L-VSC and 3L-NPC converter in a ModHVDC application with two generator/converter modules.

The selection of two modules was chosen in order to minimize computational efforts, reduce simulation time and at the same time, multiple modules are studied. Including more modules might introduce new results that are not observable with only two modules. Additionally, the wind speed input to the system is without any gusts or stochastic behaviour. System performance might be different with other wind speed input. The inclusion of wind turbine operation region three and a pitch angle controller could also be a reasonable future extension. Moreover, further model advancements could be an improved DC-grid model. This could extend the proposed feasibility of the ModHVDC generator with a 3L-NPC converter in a 10 MW wind turbine application. However, for the purpose of this project the simplified system representation was adequate.

The simulation model for obtaining losses and calculating efficiency is limited. An extension could be considering losses in time instead of an average value. This means that

thermal impedance could be used instead of thermal resistance for thermal models. Further, this may allow for studying e.g. thermal cycling, which could be interesting for investigating reliability and availability of converters. This could be another factor that influence performance in a comparison of the converters. The presented model can include this extension by minor changes.

Conclusion

This thesis had four research objectives and two research questions. The four objectives were all achieved and their associated results are the basis for answering the research questions.

The first objective of developing an adequate system model was achieved by the system modelling described in chapter 2, with its proof of concept in chapter 5. One of the contributions from this thesis is the model development and validation of a stator segmented PMSG as a Simulink model. The characteristic stator segments that are magnetically isolated and mechanically coupled was successfully developed and validated, see chapter 2.4 and appendix chapter A.2.3.

Objective two was accomplished in chapter 3. The steady state analysis presented the problem of DC-bus voltage control with series-connected converters. The following subchapter presented control methods and related challenges. A case study of eight generator/converter modules with normal distributed parameters was used in order to simulate what could be expected as DC-bus voltage variation between modules. The research question associated with the objective was:

What are the alternatives for balancing the DC-bus voltages and what are their consequences?

The case study result in Table 3.3 shows that a steady state voltage deviation of roughly $\pm 4.5\%$ might be expected. The results in Figure 5.15c show that transient overshoot might occur, so further voltage stress to certain modules should be accounted for in future designs. The alternative for keeping all DC-bus voltages equal are changing the q-axis current. By changing the current, some modules might be overloaded in turbine operational region 3. The alternatives are either to accept overloading or to lower the power output of all converters to the generator/converter module with lowest output power. For the case study, this meant that one module -4.5% voltage deviation to average voltage was compensated by reducing total DC-power output by 4.5% . This would lead to a loss of

1.3 GWh/year for a 10 MW turbine. This could potentially be a weak-point with the Mod-HVDC concept, as such losses are not acceptable from an economic perspective. Future work is recommended to study this further.

The third objective was studied in chapter 4. Three different voltage rated industrially available IGBT modules from ABB were compared in terms of losses when used in both a 2L-VSC and 3L-NPC converter. A required series-connection was established, evaluated switching frequency range was 0.5-2.0 kHz, the junction temperatures was limited to 75 °C, the turbine operation was set to nominal operation and measurement parameters were defined in chapter 4.2. By using the analytical models presented in chapter 4.2.7 for calculating losses, the results in chapter 4.3 showed that the 3.3 kV IGBT had the lowest losses for all considered IGBT modules. Additionally, the 3L-NPC converter proved more efficient than the 2L-VSC. The latter was supported by the simulation results in chapter 5.2.

Finally, the fourth objective was to investigate the performance of a 3L-NPC converter and compare to a 2L-VSC. This was conducted in chapter 5. Performance was evaluated by comparing state variables, AC and DC-side waveforms, power quality, losses and efficiency for the two converters. The loss results were obtained with a 3.3 kV IGBT module. The results from investigating the state variables proved the feasibility of the 3L-NPC converter in the ModHVDC application as the system was stable and operating as desired. The waveform comparison showed that both AC-side phase current, line-to-line voltage and DC-side current were considerably less distorted for a 3L-NPC converter compared to a 2L-VSC. The power quality of the AC-side current and line-to-line voltage showed significant improvement with a 3L-NPC converter compared to a 2L-VSC. THD in both current and voltage was considerably reduced for all wind speeds. Finally, the losses and efficiency were treated as continuous functions for turbine operation region 2 and 3. Turbine power production, the discretized wind speed distribution and efficiency were combined in order to calculate a weighted average efficiency of both converters. The results was that the 3L-NPC converter had 0.5 % higher efficiency compared to a 2L-VSC, as evidenced by its efficiency of 99.2 % compared to 98.7 % for 1.0 kHz converter switching frequency. This helps answering the research questions of:

How does the 3L-NPC converter compare to a conventional 2L-VSC in terms of performance and losses in the ModHVDC application and is it a suitable converter?

The 3L-NPC converter can perform in a stable manner and therefore offer a secure operation. It has better AC-side power quality in both current and line-to-line voltage, DC-side current ripple is reduced, it is not negatively affected by the capacitor voltage balancing control-addition, the losses are lower and the weighted average efficiency is higher than in the 2L-VSC. Based on these findings, it can be concluded that the 3L-NPC converter out-performs the 2L-VSC and is a suitable converter for use and future research as power converter for the ModHVDC generator.

Future work

The selection of power converters was limited to the 3L-NPC converter and 2L-VSC. One future extension could be to study and compare a 3L-ANPC converter and/or a five or higher-level half or full-bridge MMC to the results obtained in this thesis. Based on ABB's selection of power converter in their simulation tool SEMIS [52], this might be the most relevant converters for future study due to their industrial prevalence.

Another relevant extension for future work would be to further study and compare IGBT modules, where other manufactures than ABB are included. Accounting for datasheet difference such as gate resistance variation and compensate these differences in order to conduct a more accurate comparison are proposed as future work.

Conventional SPWM was used as modulation technique for both converters. Recommended for future work is to study other modulation strategies, e.g. space vector modulation (SVM) and compare difference. SVM can extend the linear modulation range [53] of converters, such that the voltage and current ratings might also be revised. Additionally, a dedicated study of voltage balancing techniques should also be seen in light of the various modulation strategies.

It would be interesting in future work to combine the three previous recommendations by comparing converters, IGBT modules and modulation strategies. The results might limit the region of selection and certain converters, IGBT modules and modulation strategies to be even further studied. This could be done by studying switching frequency and DC-capacitor requirements and AC/DC-side filter requirements and treat it as an optimization problem. The objective could be to minimize losses, mass and volume of the various converter configurations. This would give deep insight to future design and selection of converters.

A laboratory set-up, obtaining experimental results and validating the results in this thesis, e.g. the analytical and simulation model for losses, would be valuable. This thesis

have contributed with insight that can be used when setting up a lab-scale realization of a ModHVDC generator. At a time, it was a goal of this thesis to obtaining experimental results, but the consequences of the world wide virus outbreak COVID-19 did not allow for this to be conducted. Therefor, when the laboratory is again open, experimental results to validate the simulation results with the 3L-NPC converter would be of great interest. This might also introduce new issues that are ignored in this thesis that might be important and overlooked. This might be related to the IGBT modules rating, control system implementation and more.

Bibliography

- [1] Sverre Gjerde. *Analysis and Control of a Modular Series Connected Converter for a Transformerless Offshore Wind Turbine*. PhD thesis, Norwegian University of Science and Technology, 2013.
- [2] U.S. Department of Energy's Office of Energy Efficiency and Renewable Energy. Advanced wind turbine drivetrain trends and opportunities. <https://www.energy.gov/eere/articles/advanced-wind-turbine-drivetrain-trends-and-opportunities>, 2019. [Online; accessed 27-Feb-2020].
- [3] Yves-Marie Saint-Drenan, Romain Besseau, Malte Jansen, Iain Staffell, Alberto Troccoli, Laurent Dubus, Johannes Schmidt, Katharina Gruber, Sofia Simões, and Siegfried Heier. A parametric model for wind turbine power curves incorporating environmental conditions. *arXiv.org*, 2019.
- [4] ABB. Abb hipak igbt module 5sna 0400j650100. <https://search-ext.abb.com/library/Download.aspx?DocumentID=5SYA%201592-03LanguageCode=enDocumentPartId=Action=Launch>. [Online; accessed 09-April-2020].
- [5] Ruifang Liu, Xin Ma, Xuejiao Ren, Junci Cao, and Shuangxia Niu. Comparative analysis of bearing current in wind turbine generators. *Energies*, 11:1305, 05 2018.
- [6] C-M. Ong. *Dynamic Simulation of Electric Machinery using Matlab/Simulink*. Prentice-Hall PTR, Upper Saddle River, NJ 07458, 1998.
- [7] IEA. Sustainable development scenario. <https://www.iea.org/reports/world-energy-model/sustainable-development-scenario>. [Online; accessed 24-April-2020].
- [8] IEA. Offshore wind outlook 2019: World energy outlook special report. <https://www.iea.org/reports/offshore-wind-outlook-2019>. [Online; accessed 24-April-2020].
- [9] IEA. Tracking power 2019: Offshore wind power. <https://www.iea.org/reports/tracking-power-2019/offshore-wind>. [Online; accessed 24-April-2020].

-
- [10] IEA. Innovation gaps: Renewable power. <https://www.iea.org/reports/innovation-gaps/renewable-power>. [Online; accessed 24-April-2020].
- [11] V. Yaramasu, B. Wu, P. C. Sen, S. Kouro, and M. Narimani. High-power wind energy conversion systems: State-of-the-art and emerging technologies. *Proceedings of the IEEE*, 103(5):740–788, May 2015.
- [12] Kamran Sharifabadi, Lennart Harnfors, H.-P Nee, Staffan Norrga, and Teodorescu. *Design, control and application of modular multilevel converters for HVDC transmission systems*. 09 2016.
- [13] P. K. Olsen, S. Gjerde, R. M. Nilssen, J. Hoelto, and S. Hvidsten. A transformerless generator-converter concept making feasible a 100 kv light weight offshore wind turbine: Part i - the generator. pages 247–252, Sep. 2012.
- [14] S. S. Gjerde, P. K. Olsen, and T. M. Undeland. A transformerless generator-converter concept making feasible a 100 kv low weight offshore wind turbine part ii - the converter. pages 253–260, Sep. 2012.
- [15] P.K. Olsen. Modular high voltage direct current generator for onshore wind. Proposal submission form, August 2018.
- [16] H.A. Faraasen. Power electronic topologies and control for a modular hvdc generator. Specialization report, December 2019.
- [17] Semikron International GmbH. 3l npc tnpc topology. <https://www.semikron.com/service-support/downloads/detail/semikron-application-note-3l-npc-tnpc-topology-en-2015-10-12-rev-05.html>. [Online; accessed 02-April-2020].
- [18] S.M. Tripathi, A.N. Tiwari, and Deependra Singh. Grid-integrated permanent magnet synchronous generator based wind energy conversion systems: A technology review. *Renewable and Sustainable Energy Reviews*, 51:1288 – 1305, 2015.
- [19] Ke Ma. *Power Electronics for the Next Generation Wind Turbine System*, volume 5 of *Research Topics in Wind Energy*. Springer International Publishing, Cham, 2015.
- [20] T. M. Undeland N. Mohan and W. P. Robbins. *Power Electronics. Converters, applications and design*. John Wiley and Sons, inc, 3th edition, 2003.
- [21] A. Nabae, I. Takahashi, and H. Akagi. A new neutral-point-clamped pwm inverter. *IEEE Transactions on Industry Applications*, IA-17(5):518–523, 1981.
- [22] J. Pou, J. Zaragoza, S. Ceballos, M. Saeedifard, and D. Boroyevich. A carrier-based pwm strategy with zero-sequence voltage injection for a three-level neutral-point-clamped converter. *IEEE Transactions on Power Electronics*, 27(2):642–651, 2012.
- [23] J. Pou, J. Zaragoza, P. Rodriguez, S. Ceballos, V. M. Sala, R. P. Burgos, and D. Boroyevich. Fast-processing modulation strategy for the neutral-point-clamped converter with total elimination of low-frequency voltage oscillations in the neutral point. *IEEE Transactions on Industrial Electronics*, 54(4):2288–2294, 2007.

-
- [24] R. Berntsen. *Servosystemer med permanentmagnet synkronmotor*. Tapir Akademisk Forlag, 7005, Trondheim, 2002.
- [25] Machowski Jan, Bialek Janusz, and Bumby Jim. *Power system dynamics stability and control*. John Wiley & Sons, 2011.
- [26] Mathworks. Documentation: Permanent magnet synchronous machine. <https://se.mathworks.com/help/physmod/sps/powersys/ref/permanentmagnetsynchronousmachine.html>, 2019. [Online; accessed 06-December-2019].
- [27] P. Roshanfekar, T. Thiringer, S. Lundmark, and M. Alatalo. Selecting igbt module for a high voltage 5 mw wind turbine pmsg-equipped generating system. In *2012 IEEE Power Electronics and Machines in Wind Applications*, pages 1–6, 2012.
- [28] ABB. Insulated gate bipolar transistor (igbt) and diode modules with spt and spt+ chips. <https://new.abb.com/semiconductors/igbt-and-diode-modules>. [Online; accessed 16-March-2020].
- [29] ABB. Voltage ratings of high power semiconductors. <https://search-ext.abb.com/library/Download.aspx?DocumentID=5SYA2051&LanguageCode=en&DocumentPartId=&Action=Launch>. [Online; accessed 19-March-2020].
- [30] Lars Morten Bardal and Lars Roar Sætran. Influence of turbulence intensity on wind turbine power curves. *Energy Procedia*, 137:553 – 558, 2017. 14th Deep Sea Off-shore Wind RD Conference, EERA DeepWind’2017.
- [31] A Clifton and Rozenn Wagner. Accounting for the effect of turbulence on wind turbine power curves. *Journal of Physics: Conference Series*, 524:012109, jun 2014.
- [32] Gilbert M Masters. *Renewable and efficient electric power systems*, 2013.
- [33] Mathworks. Documentation: Wind turbine. <https://se.mathworks.com/help/physmod/sps/powersys/ref/windturbine.html>, 2019. [Online; accessed 26-Feb-2020].
- [34] Wind energy generation systems. Part 1: Design requirements. Standard, International Electrotechnical Commission, Geneva, Switzerland, February 2019.
- [35] Norges vassdrags-og energidirektorat. Vindkart for norge. kartbok 3a: Årsmiddelvind i 80m høyde. https://www.nve.no/media/2462/vind_80m_kartbok1a_4140.pdf, 2009. [Online; accessed 23-Feb-2020].
- [36] J.A. Suul. Modelling and control of synchronous machines. Norwegian University of Science and Technology, August 2019.
- [37] Mathworks. Pwm generator (three-phase, three-level). <https://se.mathworks.com/help/physmod/sps/ref/pwmgeneratorthreephasethreelevel.html>. [Online; accessed 30-April-2020].

-
- [38] J. Beerten, S. D'Arco, and J. A. Suul. Cable model order reduction for hvdc systems interoperability analysis. In *11th IET International Conference on AC and DC Power Transmission*, pages 1–10, 2015.
- [39] H. Khreis, A. Deflorio, K. Voelz, and B. Schmuelling. Sensitivity analysis on electrical parameters for permanent magnet synchronous machine manufacturing tolerances in ev and hev. In *2016 IEEE Transportation Electrification Conference and Expo (ITEC)*, pages 1–5, 2016.
- [40] W. Tursky T.Reimann A.Wintrich, U. Nicolai. *Application Manual Power Semiconductors*. SEMIKRON International GmbH, Werner-von-Siemens-Strasse 16, D-98693 Ilmenau, Germany, 2 edition, 2015.
- [41] D. Chamund N. Rao. *Calculating power losses of an IGBT module*. Dynex Semiconductor, Doddington Road, Lincoln, LN6 3LF, United Kingdom, 9 2014. Application Note.
- [42] R. Barrera-Cardenas and M. Molinas. Comparative study of wind turbine power converters based on medium-frequency ac-link for offshore dc-grids. *IEEE Journal of Emerging and Selected Topics in Power Electronics*, 3(2):525–541, June 2015.
- [43] Mitsubishi Electric Corporation. *Power Module Reliability*, 12 2019. Application note.
- [44] Semikron International GmbH. Determining switching losses of semikron igbt modules. <https://www.semikron.com/service-support/downloads/detail/semikron-application-note-determining-switching-losses-of-semikron-igbt-modules-en-2014-08-19-rev-00.html>. [Online; accessed 11-March-2020].
- [45] S. Dieckerhoff, S. Bernet, and D. Krug. Power loss-oriented evaluation of high voltage igbts and multilevel converters in transformerless traction applications. *IEEE Transactions on Power Electronics*, 20(6):1328–1336, 2005.
- [46] ABB. Applying igbts. https://library.e.abb.com/public/ab119704d4797bc283257cd3002ac5e0/Applying%20IGBTs_5SYA%202053-04.pdf. [Online; accessed 16-March-2020].
- [47] U. Shipurkar, E. Lyrakis, K. Ma, H. Polinder, and J. A. Ferreira. Lifetime comparison of power semiconductors in three-level converters for 10-mw wind turbine systems. *IEEE Journal of Emerging and Selected Topics in Power Electronics*, 6(3):1366–1377, 2018.
- [48] Mathworks. Two-level converter. <https://se.mathworks.com/help/phymod/sps/powersys/ref/twolevelconverter.html>. [Online; accessed 06-May-2020].
- [49] Mathworks. Three-level npc converter. <https://se.mathworks.com/help/phymod/sps/powersys/ref/threelevelnpcconverter.html>. [Online; accessed 06-May-2020].
- [50] ABB. *ABB HiPak IGBT Module 5SNG 0250P330300*, 8 2010. Datasheet.

-
- [51] S.M. Mueeen. *Wind Energy Conversion Systems: Technology and Trends*. Springer-Verlag London Limited, 2012.
- [52] ABB. Semis. <https://new.abb.com/semiconductors/semis>. [Online; accessed 15-May-2020].
- [53] Mathworks. Pwm generator (3-level). <https://se.mathworks.com/help/physmod/sps/powersys/ref/pwmgenerator3level.html>. [Online; accessed 30-April-2020].
- [54] V. Yaramasu, A. Dekka, M. J. Durán, S. Kouro, and B. Wu. Pmsg-based wind energy conversion systems: survey on power converters and controls. *IET Electric Power Applications*, 11(6):956–968, 2017.
- [55] C.M Ong. *Dynamic simulation of electric machinery using Matlab/Simulink*. Prentice Hall PTR, Upper Saddle River, NJ 07458, 1998.
- [56] ABB. Permanent magnet generators. <https://new.abb.com/motors-generators/generators/generators-for-wind-turbines/permanent-magnet-generators>, 2018. [Online; accessed 28-Feb-2020].
- [57] Ion Boldea. *Electric Generators Handbook - Two Volume Set*. CRC Press, 2015.
- [58] Mathworks. Documentation: Pmsm. <https://se.mathworks.com/help/physmod/sps/ref/pmsm.html>, 2020. [Online; accessed 3-Mar-2020].
- [59] P. Kundur. *Power system stability and control*. McGraw-Hill, New York, 1994.
- [60] J. A. Suul. Introduction to marine power systems and control of power electronic converters. Presentation in lecture for TTK 24 Control of Marine Power Conversion Systems, 2019.
- [61] R. Nilsen. *Electric Drives*. Norwegian University of Science and Technology. Department of Electric Power Engineering, 2018.
- [62] Mathworks. Documentation: Loss calculation in a three-phase 3-level inverter. <https://se.mathworks.com/help/physmod/sps/examples/loss-calculation-in-a-three-phase-3-level-inverter.html>, 2020. [Online; accessed 6-March-2020].
- [63] Mathworks. Igbt/diode. <https://se.mathworks.com/help/physmod/sps/powersys/ref/igbt/diode.html>. [Online; accessed 13-April-2020].
- [64] Semikron International GmbH. Skiip 3614 gb17e4-6duw v2. <https://www.semikron.com/products/product-classes/ipm/detail/skiip-3614-gb17e4-6duw-v2-20603238.html>. [Online; accessed 10-March-2020].

Appendix **A**

Appendix

A.1 Per unit system

A.1.1 Base values

Table A.1: Per unit system: AC quantities

Quantity	Expression	Value	Unit
Voltage	$V_b = \sqrt{\frac{2}{3}} V_{ac}$	5.36	kV
Current	$I_b = \sqrt{2} I_{ac}$	155.6	A
Apparent power	$S_b = \frac{3}{2} I_b V_b$	$\frac{10}{8} \cdot N$	MVA
Active power	$P_b = S_b$	$\frac{10}{8} \cdot N$	MW
Reactive power	$Q_b = S_b$	$\frac{10}{8} \cdot N$	MVA _r
Angular frequency	$\Omega_b = 2\pi f_b$	188.3	rad/s
Impedance	$Z_b = \frac{V_b}{I_b}$	34.4	Ω
Capacitance	$C_b = \frac{1}{\Omega_b Z_b}$	1.54e-4	F
Inductance	$L_b = \frac{Z_b}{\Omega_b}$	0.1828	H
Flux linkage	$\Psi_b = \frac{V_b}{\Omega_b}$	28.44	Wb

Table A.2: Per unit system: DC quantities

Quantity	Expression	Unit	
Voltage	$V_{b,dc} = 2V_b$	10.7	kV
Current	$I_{b,dc} = \frac{3}{4}I_b$	116.7	A
Power	$P_{b,dc} = S_b$	$\frac{10}{8} \cdot N$	MW
Resistance	$R_{b,dc} = \frac{8}{3}Z_b$	91.8	Ω
Capacitance	$C_{b,dc} = \frac{3}{8}C_b$	5.78e-5	F

Table A.3: Per unit system: Mechanical quantities

Quantity	Expression	Unit	
Angular speed	$\Omega_{b,m} = \frac{\Omega_b}{P_p}$	2.4458	rad/s
Torque	$T_b = P_p \frac{P_b}{\Omega_b}$	1.02e6	Nm

A.1.2 Per unit values

Per unit values of an arbitrary unit X is defined as:

$$x_{pu} = \frac{X_{real}}{X_{base}} \tag{A.1}$$

A.2 Chapter 2

A.2.1 PMSG

The permanent magnet synchronous generator (PMSG) are at present the most popular generator for high-power wind energy conversion system [54]. Use of permanent magnets instead of rotor windings, means that the generator needs no external excitation and enables a more efficient, reliable and more compact generator compared to competing technologies [55, p. 310][56].

The two main types of rotor designs for a PMSG are:[57, p. 20]

1. With surface mounted magnets - non-salient pole rotor
2. With interior mounted magnets - salient pole rotor

An illustration of the difference are seen in Figure A.1. The first type uses special adhesives and resilient coating to mount the magnets to the rotor surface. The round rotor construction leads to an isotropic machine, i.e. equal direct (d) and quadrature (q) axis inductance. This is however an approximation, as the minor contribution of magnet recoil permeability temperature dependency is neglected [57, p. 21]. Surface mounted magnets are typically used in direct driven PMSG in wind turbines [5] and is therefore chosen for machine modeling.

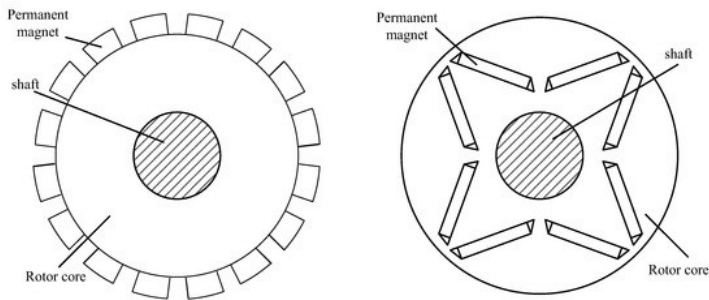


Figure A.1: Left: surface mounted magnets. Right: built-in magnets [5].

Theoretical background for single segment PMSG

Figure A.2a show a cross-section of a 2-pole round rotor machine. The illustration and stator schematic in Figure A.2b are used as a reference for modeling in both abc and dq-reference frame. The derivation used in this chapter is fundamental to the modeling of the machine with segmented stator in chapter 2.3.1.

Representation in abc-reference frame

The voltage balance equation for a synchronous machine with generator reference can be expressed by equation (A.2) [25, p. 440].

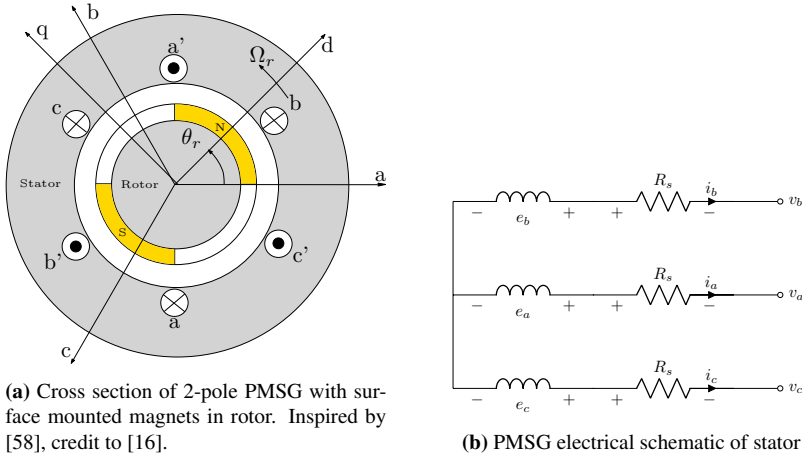


Figure A.2: Illustration of a round rotor PMSM showing the dq axis in a rotating reference frame

$$\vec{V}_{abc} = -R_s \vec{I}_{abc} + \vec{E}_{abc} = -R_s \vec{I}_{abc} + \frac{d\vec{\Psi}_{abc}}{dt} \quad (\text{A.2})$$

Unlike the wound rotor synchronous machine, the flux linkage can be expressed without coupled stator-rotor flux linkage due to the permanent magnets. Summing stator $\vec{\Psi}_{abc}^s$ and rotor-side $\vec{\Psi}_{abc}^r$ flux linkage are therefore possible [24, p. 22]. Rotor-side flux linkage amplitude Ψ_m is constant as the magnets produce a constant flux. By using the stator-side inductance \mathbf{L}_{abc}^s matrix and currents, the stator-side flux linkage contribution to total stator-side flux linkage $\vec{\Psi}_{abc}$ are found.

$$\vec{\Psi}_{abc} = \vec{\Psi}_{abc}^r - \vec{\Psi}_{abc}^s \quad (\text{A.3})$$

$$\vec{\Psi}_{abc}^s = \mathbf{L}_{abc}^s \vec{I}_{abc} = \begin{bmatrix} L_{aa} & L_{ab} & L_{ac} \\ L_{ba} & L_{bb} & L_{bc} \\ L_{ca} & L_{cb} & L_{cc} \end{bmatrix} \begin{bmatrix} i_a \\ i_b \\ i_c \end{bmatrix} \quad (\text{A.4})$$

$$\vec{\Psi}_{abc}^r = \Psi_m \begin{bmatrix} \cos(\theta_r) \\ \cos(\theta_r - \frac{2}{3}\pi) \\ \cos(\theta_r + \frac{2}{3}\pi) \end{bmatrix} \quad (\text{A.5})$$

The self-inductance due to air-gap flux L_{g0} of a round rotor machine are constant as there is no saliency [59, p. 62]. This simplifies the expression for total self inductance of the phases to the aforementioned and leakage inductance $L_{\sigma s}$, which are both constant.

$$L_{aa} = L_{bb} = L_{cc} = L_{\sigma s} + L_{g0} \quad (\text{A.6})$$

By evaluating the air-gap flux that links the different phases, it can be shown that the mutual inductance is also constant due to the round rotor [59, p. 64].

$$L_{ij} = -\frac{L_{g0}}{2}, \quad i \neq j \quad (\text{A.7})$$

Stator inductance matrix becomes:

$$\mathbf{L}_{\text{abc}}^s = \begin{bmatrix} L_{\sigma s} + L_{g0} & -\frac{L_{g0}}{2} & -\frac{L_{g0}}{2} \\ -\frac{L_{g0}}{2} & L_{\sigma s} + L_{g0} & -\frac{L_{g0}}{2} \\ -\frac{L_{g0}}{2} & -\frac{L_{g0}}{2} & L_{\sigma s} + L_{g0} \end{bmatrix} \quad (\text{A.8})$$

Representation in dq0-reference frame

The stationary abc reference frame time varying coefficients introduces considerable complexity in solving machine and power system problems. To obtain time-invariant expressions and ease computations, the Park transform can be applied with rotors synchronously rotating reference frame. Numerous transformations exist and are dependant on the dq-axis orientation and reference angle to the magnetic a-axis. The chosen orientation in this thesis are widely used and in line with IEEE standard definition [59, p.53], see Figure A.3. It is also chosen to use the amplitude invariant transformation, i.e. value of dq-component equals peak-value of abc-component. The transformation matrices are:

$$\mathbf{P}_{\text{dq0}} = \frac{2}{3} \begin{bmatrix} \cos(\theta_r) & \cos(\theta_r - \frac{2}{3}\pi) & \cos(\theta_r + \frac{2}{3}\pi) \\ -\sin(\theta_r) & -\sin(\theta_r - \frac{2}{3}\pi) & -\sin(\theta_r + \frac{2}{3}\pi) \\ \frac{1}{2} & \frac{1}{2} & \frac{1}{2} \end{bmatrix} \quad (\text{A.9})$$

$$\mathbf{P}_{\text{dq0}}^{-1} = \begin{bmatrix} \cos(\theta_r) & -\sin(\theta_r) & 1 \\ \cos(\theta_r - \frac{2}{3}\pi) & -\sin(\theta_r - \frac{2}{3}\pi) & 1 \\ \cos(\theta_r + \frac{2}{3}\pi) & -\sin(\theta_r + \frac{2}{3}\pi) & 1 \end{bmatrix} \quad (\text{A.10})$$

A general transformation from to abc to dq0 reference frame and reverse:

$$\vec{f}_{dq0} = \mathbf{P}_{\text{dq0}} \vec{f}_{abc} \quad (\text{A.11})$$

$$\vec{f}_{abc} = \mathbf{P}_{\text{dq0}}^{-1} \vec{f}_{dq0} \quad (\text{A.12})$$

Flux linkage in dq0 reference frame

The stator flux linkage are found in dq0-components by using the Park transform to equation (A.4).

$$\vec{\Psi}_{dq0}^s = \mathbf{P}_{\text{dq0}} \mathbf{L}_{\text{abc}}^s \mathbf{P}_{\text{dq0}}^{-1} \vec{I}_{dq0} = \begin{bmatrix} L_{\sigma s} + \frac{3L_{g0}}{2} & 0 & 0 \\ 0 & L_{\sigma s} + \frac{3L_{g0}}{2} & 0 \\ 0 & 0 & L_{\sigma s} \end{bmatrix} \begin{bmatrix} I_d \\ I_q \\ I_0 \end{bmatrix} \quad (\text{A.13})$$

Defining the dq0-inductances as:

$$\begin{aligned} L_d = L_q &= L_{\sigma s} + \frac{3L_{g0}}{2} \\ L_0 &= L_{\sigma s} \end{aligned} \quad (\text{A.14})$$

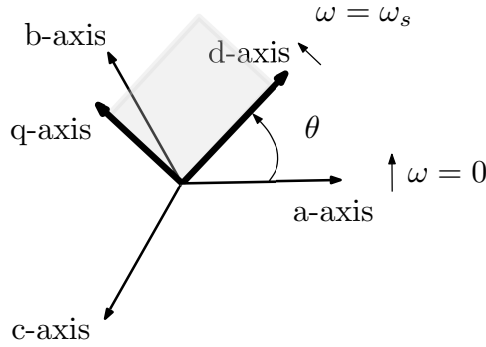


Figure A.3: Park transform. Stationary abc-reference frame converted to synchronously rotating dq-reference frame. Inspired by [6, p. 143].

And the following expression are valid for stator-side flux linkage:

$$\begin{aligned}\Psi_d^s &= L_d I_d \\ \Psi_q^s &= L_q I_q \\ \Psi_0^s &= L_0 I_0\end{aligned}\tag{A.15}$$

The rotor-side flux linkage are found by applying the Park transform to equation (A.5). As seen in Figure A.2a, the d-axis is oriented with respect to the magnetic north pole. As a consequence, rotor-side flux linkage is constant in the d-axis and zero i q-axis as it is orthogonal to the flux.

$$\vec{\Psi}_{dq0}^r = \mathbf{P}_{dq0} \Psi_m \begin{bmatrix} \cos(\theta_r) \\ \cos(\theta_r - \frac{2}{3}\pi) \\ \cos(\theta_r + \frac{2}{3}\pi) \end{bmatrix} = \begin{bmatrix} \Psi_m \\ 0 \\ 0 \end{bmatrix}\tag{A.16}$$

Total flux linkage in dq0 reference frame is:

$$\begin{aligned}\Psi_d &= \Psi_m - L_d I_d \\ \Psi_q &= -L_q I_q \\ \Psi_0 &= -L_0 I_0\end{aligned}\tag{A.17}$$

Stator voltage in dq0 reference frame

The starting point of the derivation is the basic phase voltage, equation (A.2). The results of applying the Park transform is:

$$\begin{aligned}\vec{V}_{dq0} \mathbf{P}_{dq0}^{-1} &= -R_s \mathbf{P}_{dq0}^{-1} \vec{I}_{dq0} + \frac{d}{dt} \left(\mathbf{P}_{dq0}^{-1} \vec{\Psi}_{dq0} \right) \\ \vec{V}_{dq0} &= -\mathbf{P}_{dq0} R_s \mathbf{P}_{dq0}^{-1} \vec{I}_{dq0} + \mathbf{P}_{dq0} \frac{d}{dt} \left(\mathbf{P}_{dq0}^{-1} \vec{\Psi}_{dq0} \right)\end{aligned}\tag{A.18}$$

The resistive voltage drop simplifies due to the matrix multiplication derivation:

$$- \mathbf{P}_{dq0} R_s \mathbf{P}_{dq0}^{-1} \vec{I}_{dq0} = -R_s \vec{I}_{dq0} \quad (\text{A.19})$$

The term involving the total flux linkage requires using the product rule of derivation:

$$\mathbf{P}_{dq0} \frac{d}{dt} \left(\mathbf{P}_{dq0}^{-1} \vec{\Psi}_{dq0} \right) = \mathbf{P}_{dq0} \left(\frac{d\mathbf{P}_{dq0}^{-1}}{dt} \vec{\Psi}_{dq0} + \mathbf{P}_{dq0}^{-1} \frac{d\vec{\Psi}_{dq0}}{dt} \right) \quad (\text{A.20})$$

The derivative of electrical rotor angle θ_r equals angular frequency:

$$\frac{d\theta_r}{dt} = \Omega_r \implies \theta_r = \Omega_r t \quad (\text{A.21})$$

By using this equality, it can be shown that the first term in equation A.20 that gives the cross coupling can be written as:

$$\mathbf{P}_{dq0} \frac{d\mathbf{P}_{dq0}^{-1}}{dt} \vec{\Psi}_{dq0} = \Omega_r \begin{bmatrix} 0 & -1 & 0 \\ 1 & 0 & 0 \\ 0 & 0 & 0 \end{bmatrix} \vec{\Psi}_{dq0} \quad (\text{A.22})$$

The second term in equation (A.20) simplifies due to the matrix multiplication.

$$\mathbf{P}_{dq0} \mathbf{P}_{dq0}^{-1} \frac{d\vec{\Psi}_{dq0}}{dt} = \frac{d\vec{\Psi}_{dq0}}{dt} \quad (\text{A.23})$$

By using the forgoing derivation and the flux linkage expression from chapter A.2.1, the resulting dq0-reference frame generator terminal voltages in SI-units are:

$$\begin{aligned} V_d &= -R_s I_d + \frac{d\Psi_d}{dt} - \Omega_r \frac{d\Psi_q}{dt} = -R_s I_d - L_d \frac{dI_d}{dt} + \Omega_r L_q I_q \\ V_q &= -R_s I_q + \frac{d\Psi_q}{dt} + \Omega_r \frac{d\Psi_d}{dt} = -R_s I_d - L_q \frac{dI_q}{dt} - \Omega_r L_d I_d + \Omega_r \Psi_m \\ V_0 &= -R_s I_0 + \frac{d\Psi_0}{dt} = -R_s I_0 - L_0 \frac{dI_0}{dt} \end{aligned} \quad (\text{A.24})$$

Expression for power

In this section, analytical expressions in SI-units for active and reactive power in any system is developed. Based on the amplitude invariant Park-transform seen in Figure A.3 and described analytically in Equation (A.9), the apparent power of a balanced 3-phase system is [6, p. 277]:

$$\begin{aligned} S &= P + jQ \\ S &= \frac{3}{2} (V_d + jV_q)(I_d + jI_q)^* \\ P &= \frac{3}{2} (V_d I_d + V_q I_q) \\ Q &= \frac{3}{2} (V_q I_d - V_d I_q) \end{aligned} \quad (\text{A.25})$$

The constant of 1.5 are relates to the three-phases, hence the numerator (3), and the use amplitude invariant Park-transform. The dq-components of current and voltage equals the peak value of the abc-components and must be corrected to RMS values in the expression for power. The product of that correction to voltage and current gives the denominator (2).

Note that if the zero sequence component was non-zero, the contribution would be observed in active power [6, p.271]

$$P = \frac{3}{2}(V_d I_d + V_q I_q) + 3V_0 I_0 \quad (\text{A.26})$$

Expression for torque

Active power in a PMSG P_e can be separated to electric losses P_{cu} , magnetic losses P_{dW} and developed electromechanical power P_{em} [24, p. 26][6, p. 272].

$$\begin{aligned} P_e &= \frac{3}{2}(V_q I_q + V_d I_d) = P_{em} - P_{cu} - P_{dW} \\ P_{em} &= \frac{3}{2}\Omega_r (\Psi_d I_q - \Psi_q I_d) \\ P_{cu} &= \frac{3}{2}R_s(I_q^2 + I_d^2) \\ P_{dW} &= \frac{3}{2}\left(I_q \frac{d\Psi_q}{dt} + I_d \frac{d\Psi_d}{dt}\right) \end{aligned} \quad (\text{A.27})$$

The electrical angular frequency of a machine can be linked to the mechanical angular speed $\Omega_{r,m}$ by the number of pole pairs in the machine P_p .

$$\Omega_r = P_p \Omega_{r,m} \quad (\text{A.28})$$

Inserting this relationship into equation (A.27) and explicit form of dq-axis flux linkages gives developed electromechanical power:

$$P_{em} = \frac{3}{2}P_p \Omega_{r,m} (\Psi_m I_q + (L_d - L_q)I_d I_q) \quad (\text{A.29})$$

Dividing by mechanical angular speed, the developed torque can be found:

$$T_e = \frac{P_{em}}{\Omega_{r,m}} = \frac{3}{2}P_p \Psi_m I_q + \frac{3}{2}P_p (L_d - L_q)I_d I_q \quad (\text{A.30})$$

The contribution from difference in dq-axis flux gives the developed reluctance torque [24, p. 27]. As this is a round rotor machine and there is no saliency $L_d = L_q$, the reluctance torque is zero and the expression for developed torque simplifies to:

$$T_e = \frac{3}{2}P_p \Psi_m I_q = k_T I_q \quad (\text{A.31})$$

The torque constant of the machine is given by k_T [24].

Mechanical system

The generator shaft is directly connected to wind turbine rotor shaft as seen in chapter 2.3.1. Mechanical system dynamics are described by the same equations as in that chapter with $N = 1$.

A.2.2 PMSG voltage equations in per unit

The proof for transformation of the PMSG dq voltage equations to per units values are seen in the following derivation. For d-axis voltage:

$$\begin{aligned}\frac{V_d}{V_b} &= \frac{-R_s I_d}{V_b} - \frac{L_s \frac{dI_d}{dt}}{V_b} + \frac{\Omega_r L_s I_q}{V_b} \\ \frac{V_d}{V_b} &= \frac{-R_s I_d}{I_b Z_b} - \frac{L_s \frac{dI_d}{dt}}{I_b \Omega_b L_b} + \frac{\Omega_r L_s I_q}{I_b \Omega_b L_b} \\ v_d &= -r_s i_d - \frac{l_s}{\Omega_b} \frac{di_d}{dt} + \omega_r l_s i_q\end{aligned}\tag{A.32}$$

For q-axis voltage:

$$\begin{aligned}\frac{V_q}{V_b} &= \frac{-R_s I_q}{V_b} - \frac{L_s \frac{dI_q}{dt}}{V_b} - \frac{\Omega_r L_s I_d}{V_b} + \frac{\Omega_r \Psi_m}{V_b} \\ \frac{V_q}{V_b} &= \frac{-R_s I_q}{I_b Z_b} - \frac{L_s \frac{dI_q}{dt}}{I_b \Omega_b L_b} - \frac{\Omega_r L_s I_d}{I_b \Omega_b L_b} + \frac{\Omega_r \Psi_m}{\Omega_b \Psi_b} \\ v_q &= -r_s i_q - \frac{l_s}{\Omega_b} \frac{di_q}{dt} - \omega_r l_s i_d + \omega_r \psi_m\end{aligned}\tag{A.33}$$

A.2.3 Segmented PMSG Simulink model

MathWorks MATLAB-based graphical modeling software Simulink is used throughout this thesis to perform required system modeling, simulation and analysis. As the software does not provide a built-in model of a segmented PMSG, development of a custom made model was required.

The developed model can be broken down into an electrical and a mechanical model. These are described in chapter A.2.3 and A.2.3 respectively. The description is for a single segment. Modularity is a requirement as different analysis requires different number of segments. This is achieved, as the electrical models are identical for all segments and share the same mechanical inputs. Their electrical torque are summed and used as input to the mechanical model. In chapter A.2.3 the model is validated by comparing the model to Simulink's library model of a PMSM in generator operation.

Electrical model

The electrical model block in Simulink is presented in Figure A.4. The input to this block are phase voltages V_{abc} , rotor electrical angle θ and rotor speed Ω_r . Phase voltage is an external measurement and individual for each segment. The other inputs are common for all segments and are outputs from the mechanical model.

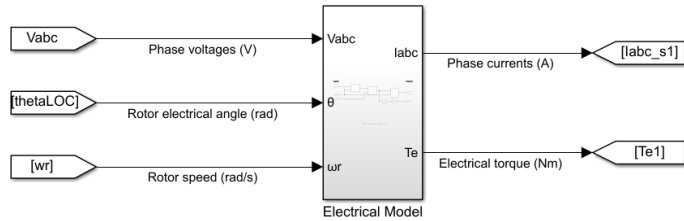


Figure A.4: Electrical model block.

Inside the block, the input voltages are transformed to dq0-reference frame and used as input to the current dynamics block.

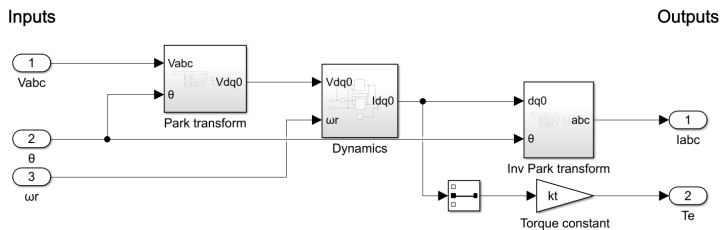


Figure A.5: Content of electrical model.

The dynamics block in Figure A.6 is a graphical model of equation (2.8) and equation (2.9). The output is current in dq0-components, where the zero-component is forced to zero. Note that the use of variable L_s represent the common dq-axis inductance as they are equal.

Current q-axis component is used to calculate the electromechanical torque as given in equation (2.10). Finally, the dq0-components are transformed back to abc-reference frame and used as signal input to current sources that interfaces the signal system and physical component system. These current sources are the AC-side input to the power converter. The ports ABC in Figure A.7 represent the connection. The parallel resistance across the current sources are required for avoiding errors with Simulink compiler. Numerical values to the resistances are investigated in chapter A.2.3.

Mechanical model

The mechanical model is presented Figure A.8. The three inputs are electrical torque, mechanical torque and initialization of the rotor mechanical speed $\Omega_{r,m}$. The electrical

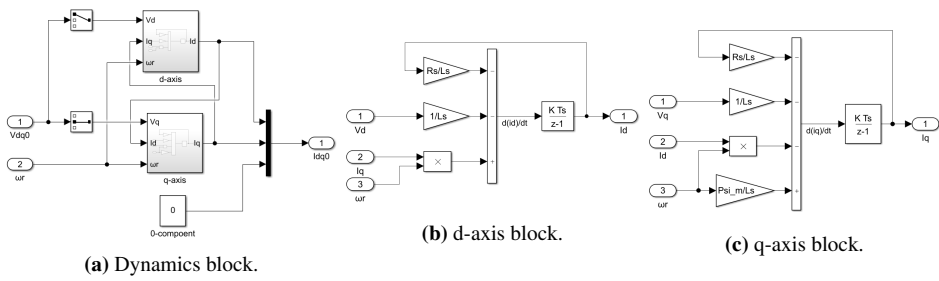


Figure A.6: Dynamics block and content.

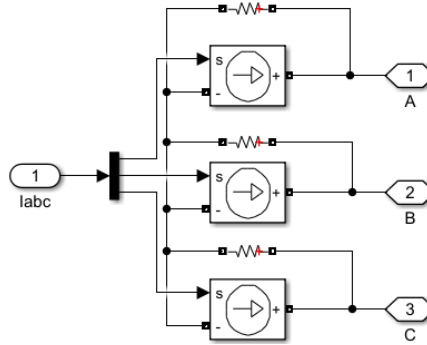


Figure A.7: PMSG segment physical model that is connected to the power converter.

torque input are presented as a single input, but could be the sum of all segments developed torque $\sum_{i=1}^N T_{e,i}$. The mechanical torque is the developed torque by the wind turbine. Output variables are rotor electrical speed ω_r and angle θ . Figure A.9 show the content of the mechanical model block.

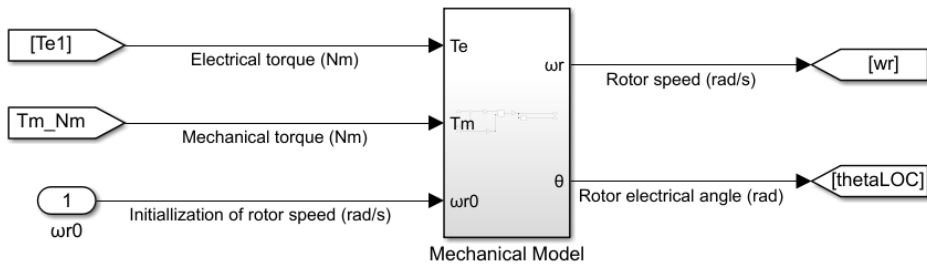


Figure A.8: Mechanical model block.

Figure A.9 show a graphical model representation of equation (2.11). The output variable from the centrally placed integrator block is mechanical shaft speed. The integrator block is initialized to a value such that the speed is within operational region 2 of the wind turbine. Mechanical speed is multiplied by number of pole pairs P_p to obtain electrical

speed. The second integrator gives the rotor electrical angle.

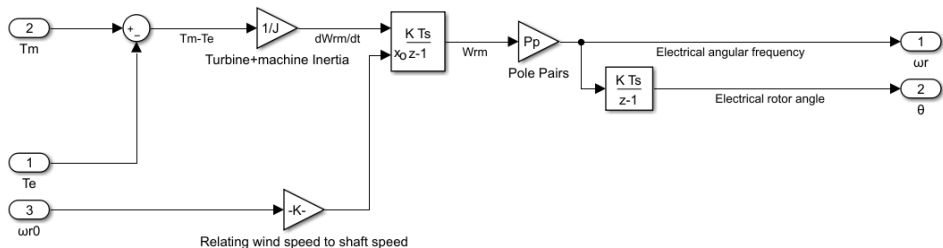


Figure A.9: Mechanical model block.

Model validation

A comparison to Simulink’s PMSM library component [26] operating as a generator was conducted in order to validate the presented model for a single segment. Due to the models modularity, it is assumed that if the model is valid for a single segment, it is valid for multiple segments as they are identical. Comparison was performed by analyzing the state variables i_d , i_q and ω_r . Both machines was identically parameterized and wind speed model, wind turbine model, control system, power converter (2L-VSC) and DC-grid was equally modelled as well. The parallel resistance seen in Figure A.7 is set to 1 TΩ. Justification to that value is given in Table A.4.

Reference current

A positive and negative step in both d and q-axis reference current was included. It allows for observing response in a state when the state itself is changed and its response to cross-coupling effects. The reference currents are shown in Figure A.10. First, a positive step in d-axis reference current occurs. A second later an equal negative step is applied. After three seconds a negative step in q-axis current leads to an acceleration of the machine and changes in rotor speed. The acceleration is stopped a second later as the q-axis current has a positive step of magnitude 1.0 pu. The step-size in q-axis current are greater than the d-axis current. It is justified by that i_d is normally zero in this model.

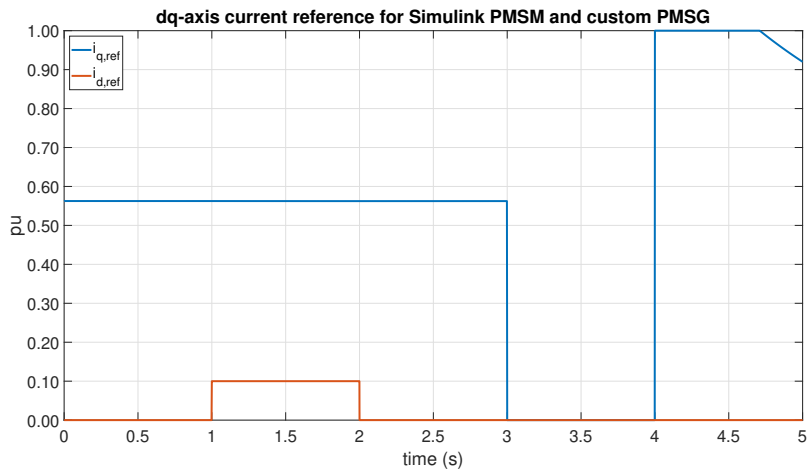


Figure A.10: Current references.

q-axis current

Response in q-axis current are presented in Figure A.12. The result show limited deviation between the machines. Numerical values to deviation are given in Table A.4. When zooming in on the response for step in i_d , some deviation and partially counter-phase behaviour can be observed. However, when the step is applied, the behaviour is identical. Response to step-change in i_q is very close to being identical.

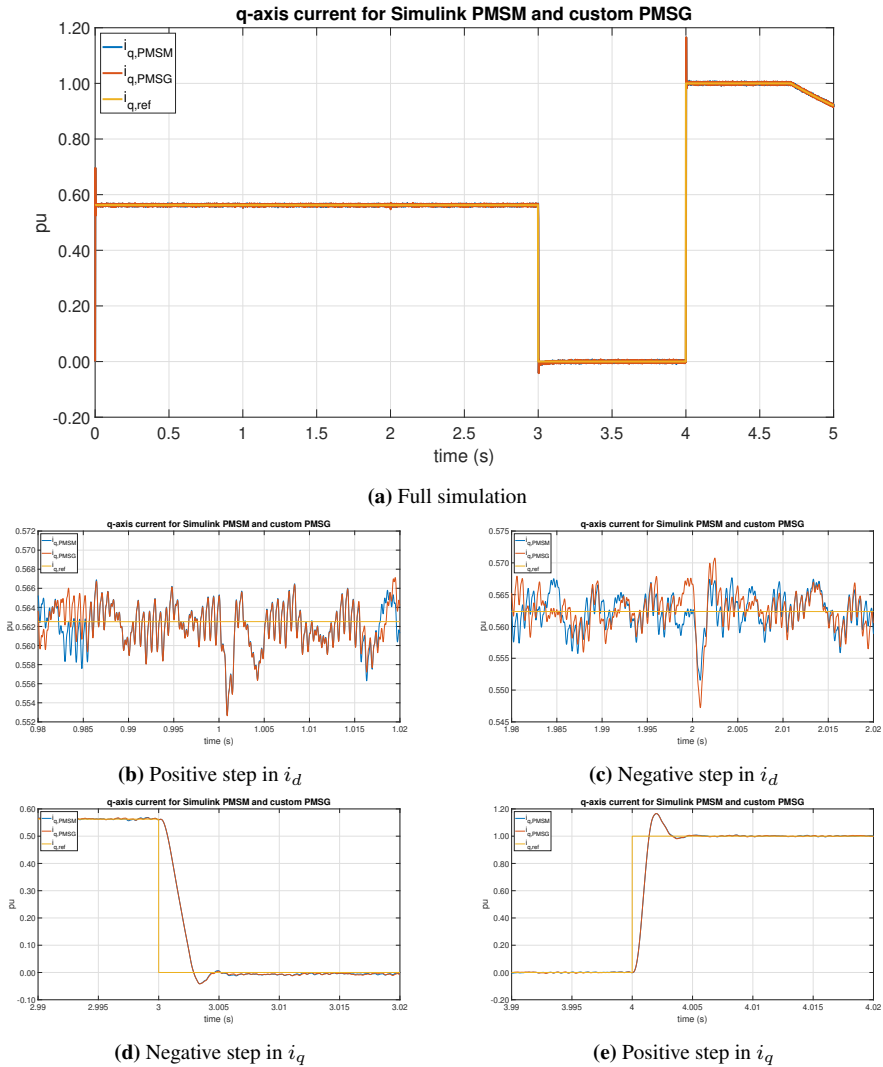


Figure A.11: q-axis current for custom made PMSG compared to Simulink's original model of a PMSM.

d-axis current

Figure A.12 show the response in d-axis current. Also this state variable show marginal difference, but identical response during steps in all variables.

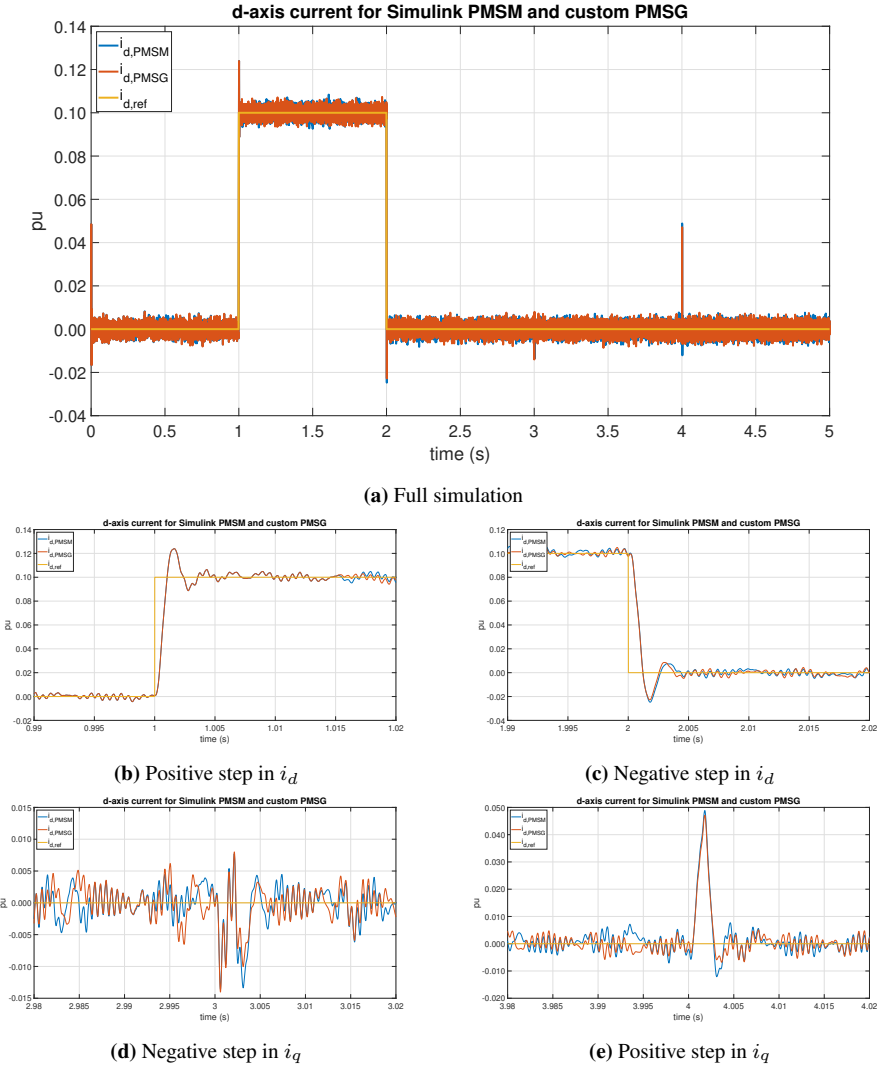


Figure A.12: d-axis current for custom made PMSG compared to Simulink's original model of a PMSG.

Shaft speed

Shaft speed ω_r are presented in Figure A.13. The deviation between the machines are presented in Figure A.13b and the difference is non-existent.

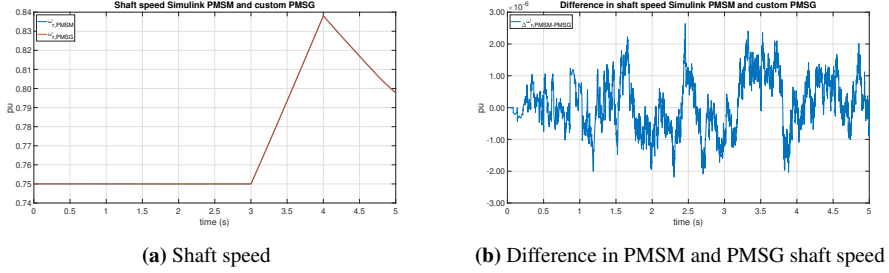


Figure A.13: Shaft speed ω_r for custom made PMSG compared to Simulink's original model of a PMSM.

Measured deviation and effect of parallel resistance

Table A.4 shows the numeric difference in dq-axis current from Simulink's PMSM to the proposed model of a segmented PMSG. The result shows maximum, minimum and average deviation between the PMSM and segmented PMSG as calculated in equation (A.34). The calculation is treated element-wise for all data-points in the simulation, which generates a set. The maximum and minimum of that set are presented as $\Delta i_{d/q,max}$ and $\Delta i_{d/q,min}$. The average deviation is calculated as the average of the absolute value difference between each element of the set.

$$\Delta i = i_{PMSM} - i_{PMSG} \quad (A.34)$$

The result also highlights how the parallel resistance influences the result. It is shown that that 1 terra ohm resistance provides the smallest average deviation and are therefore chosen. Numeric values in Table A.4 are derived from per unit values where 0.01 pu = 1 %.

Table A.4: Difference in dq-axis current from Simulink's PMSM to segmented PMSG.

R	$\Delta i_{q,max}$	$\Delta i_{q,min}$	mean(abs(Δi_q))	$\Delta i_{d,max}$	$\Delta i_{d,min}$	mean(abs(Δi_d))
1 M Ω	0.86 %	-1.00 %	0.14 %	0.90 %	-0.81 %	0.15 %
1 G Ω	1.01 %	-0.96 %	0.14 %	0.96 %	-0.87 %	0.14 %
1 T Ω	0.97 %	-0.93 %	0.13 %	0.77 %	-0.86 %	0.13 %
1 P Ω	0.86 %	-0.82 %	0.15 %	0.85 %	-0.81 %	0.15 %

The results show marginal deviation, but the difference between the machines are limited to below 1 % for all studied operation. Therefore, the model is considered to be validated.

A.2.4 Tuning of controllers

Current controller

Figure A.14 show the current controller, PWM gain and delay in addition to PMSG response. Low pass filters are included in the simulation model, but are not accounted for when tuning.

The PI controllers sets the required voltage at the converters terminals for a given current reference. Voltage set-point v_d^* and v_q^* is a sum of the PI-controller and the cross-coupling terms $\psi_d \cdot \omega_r$ and $\psi_q \cdot \omega_r$. The reference dq-axis voltage are then divided by the per unit DC-bus voltage v_{dc} in order to cancel the associated PWM gain of $\frac{V_{dc}}{2}$ and linearize the system [60]. The division forms the d and q-axis modulation indices m_d and m_q . The delay-effect in the PWM T_e is assumed to be half the switching frequency period $\frac{T_{sw}}{2}$. Plant response relates to the dq-axis resistance r_s and inductance l_s of the round rotor PMSG. The response is a first order RL-response.

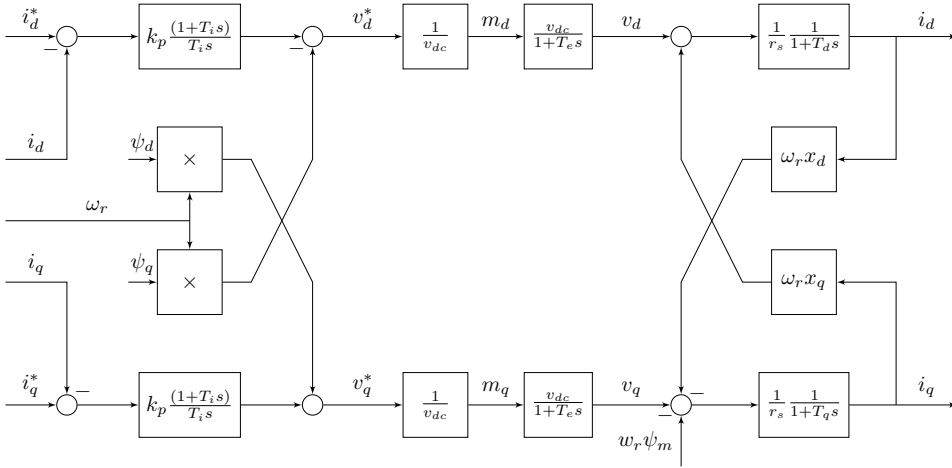


Figure A.14: Current controller, PWM and plant response.

The tuning is conducted by using pole-zero cancellation and modulus optimum [61]. Both dq-axis are identical as the PMSG are equal in these axes. PI time constant T_i is given by equation (A.35), proportional constant K_p is given by equation (A.36) and the integrator constant K_i is given by equation (A.37).

$$T_i = T_d = T_q = \frac{l_s}{r_s \cdot \Omega_b} \quad (\text{A.35})$$

$$k_p = \frac{l_s}{2 \cdot T_e \cdot \Omega_b} \quad (\text{A.36})$$

$$k_i = \frac{k_p}{T_i} = \frac{r_s}{2 \cdot T_e} \quad (\text{A.37})$$

Table A.5: Current controller PI-controller constants.

Constant	Value
K_p	1.75
K_i	20
T_i	0.0876

Speed controller

For tuning, the system can be seen as in Figure A.15. The output of the speed controller enters the current controller. In this analysis, a time scale separation is assumed due to the bandwidth of this outer loop controller and the inner loop current controller. The response of the current controller is approximated to be a first order response with time constant $T_{eq,cc}$. The q-axis current are then multiplied by ψ_m in order to obtain the electrical torque. Plant response are then given by equation 2.21.

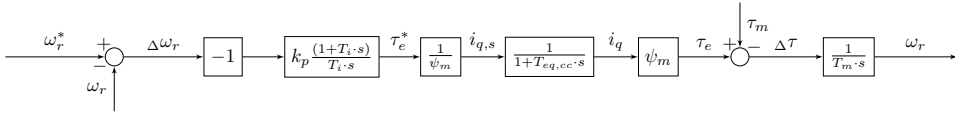


Figure A.15: Speed controller system for tuning.

The PI-controller constants are given in the equations below, where the constant β is initially set to 4 [61, p. 252]. The constant might be increased if the cross-over frequency of the outer loop $\omega_{c,sc}$ is higher than the one tenth of current controller cross over frequency $\omega_{c,cc}$. Symmetrical optimum is used in order to obtain the constants. Table A.6 presents the PI-controller constants.

$$K_p = \frac{T_m}{\sqrt{\beta} \cdot T_{eq,cc}} \quad (\text{A.38})$$

$$T_i = \beta \cdot T_{eq,cc} \quad (\text{A.39})$$

$$\omega_{c,sc} = \frac{1}{\sqrt{\beta} \cdot T_{eq,cc}} \quad (\text{A.40})$$

Table A.6: Speed controller PI-controller constants.

Constant	Value
K_p	187
K_i	2909
T_i	0.0642

DC-bus voltage controller

Tuning of the voltage controller is identical to tuning of the speed controller. The plant equation is given by equation 2.23. The following equations give PI-controller constants and their numerical value are given in Table A.7.

$$K_p = \frac{c}{\Omega_b \cdot \sqrt{\beta} \cdot T_{eq,cc}} \quad (\text{A.41})$$

$$T_i = \Omega_b \cdot \beta \cdot T_{eq,cc} \quad (\text{A.42})$$

$$K_i = \frac{K_p}{T_i} \quad (\text{A.43})$$

Table A.7: DC-bus voltage controller PI-controller constants.

Constant	Value
K_p	2.86
K_i	44.5
T_i	0.0642

Capacitor voltage balancing controller

The proportional constant is equal to DC-bus voltage controller proportional constant based on empirical tuning.

A.3 Chapter 4

A.3.1 Analytical calculation models

Table A.8 is a table of symbols with associated description for the symbols used in the analytical calculation models for losses in a 2L-VSC and 3L-NPC converter.

Table A.8: Table of symbols.

Symbol	Meaning
$\cos \phi$	Power factor. When operating the converter as rectifier, $\cos \phi \leq 0$
E_{rr}	Reference reverse recovery loss measurement taken from datasheet
E_{sw}	Reference IGBT switching loss measurement taken from datasheet.
f_{sw}	Converter switching frequency.
\hat{I}	Peak RMS value of phase current supplied to the converter
$I_{ref}, V_{ref}, T_{ref}$	Reference values for switching loss measurement taken from datasheet
K_i	Current dependency of switching loss. IGBT ≈ 1 ; Diode $\approx 0.5...0.6$
K_v	Voltage dependency of switching loss. IGBT $\approx 1.2...1.4$; Diode ≈ 0.6
m_a	PWM modulation amplitude index
$R_{CE}(T_j)$	Temperature-dependent bulk resistance of IGBT on-state characteristic
$R_F(T_j)$	Temperature-dependent bulk resistance of diode on-state characteristic
$T_{E_{rr}}$	Temperature coefficients of the reverse recovery loss $\approx 0.005...0.006$ 1/K.
$T_{E_{sw}}$	Temperature coefficients of the switching loss ≈ 0.003 1/K.
T_j	Device junction temperature
V_{CC}	IGBT/diode steady state blocking voltage
$V_{CE0}(T_j)$	Temperature-dependent threshold voltage of IGBT on-state characteristic
$V_{F0}(T_j)$	Temperature-dependent threshold voltage of Diode on-state characteristic

Table A.9 show the variables that are common for all IGBT modules in the analytical models. The modulation index is calculated by using the system steady state equation.

$$m_a = \frac{\sqrt{v_d^2 + v_q^2}}{v_{dc}} \quad (\text{A.44})$$

The power factor are calculated by using analysing the system in steady state and applying the power equations given in chapter 2.3.1. The analytical models require that the power factor is negative as the converters operates as rectifiers.

$$\cos \phi = -\frac{p_i}{\sqrt{p_i^2 + q_i^2}} \quad (\text{A.45})$$

Table A.9: Input data to analytical models.

Symbol	Description	Value	Unit
m_a	Amplitude modulation index	0.89	
\hat{I}	Peak RMS AC-side current	156	A
ϕ	Power factor angle	2.82	rad
$\cos \phi$	Power factor	-0.95	
f_{sw}	Switching frequency	0.5-2.0	kHz
K_i (IGBT)	Current dependency of switching loss	0.9	
K_v (IGBT)	Voltage dependency of switching loss	1.2	
K_i (Diode)	Current dependency of switching loss	0.57	
K_v (Diode)	Voltage dependency of switching loss	0.6	
$T_{E_{sw}}$	Temperature coefficients of the switching loss	0.003	1/K
$T_{E_{rr}}$	Temperature coefficients of the reverse recovery loss	0.006	1/K

Table A.10 show the IGBT module specific input data to the analytical models.

Table A.10: IGBT module specific input data to analytical model.

Manufacturer	ABB	ABB	ABB
Model	5SNA 0400J650100	5SNA 0650J450300	5SNA 0800N330100
V_{CES} (kV)	6.5	4.5	3.3
I_c (A)	400	650	800
Module type	Single IGBT	Single IGBT	Single IGBT
I_{ref} (A)	400	650	800
V_{ref} (kV)	3.6	2.8	1.8
T_{ref} (°C)	125	125	125
E_{sw} (J)	4.92	5	2.63
E_{rr} (J)	1.38	1.61	1.18
R_{CE} 25 °C (Ω)	0.0071	0.0037	0.0030
R_{CE} 125 °C (Ω)	0.0097	0.0055	0.0046
V_{CE0} 25 °C (V)	1.79	1.06	1.20
V_{CE0} 125 °C (V)	1.95	1.01	1.17
R_F 25 °C (Ω)	0.0043	0.0028	0.0020
R_F 125 °C (Ω)	0.0059	0.0040	0.0029
V_{F0} 25 °C (V)	1.87	1.84	1.14
V_{F0} 125 °C (V)	1.47	1.50	0.76

Table A.11 and Table A.12 show the device voltage V_{cc} for the various presented configurations in chapter 4.2. In this calculation, the redundant modules presented in mentioned in chapter 2.4 are neglected. The V_{cc} voltage for the 2L-VSC and 3L-NPC converter are given by equation (A.46) and (A.47) respectively.

$$V_{cc} = \frac{100}{N \cdot n_{\text{series},2L}} \text{ kV} \quad (\text{A.46})$$

$$V_{cc} = \frac{100}{2 \cdot N \cdot n_{\text{series},3L}} \text{ kV} \quad (\text{A.47})$$

Table A.11: IGBT modules series-connection and device voltage for $N = 8$ segments.

V_{CES} (kV)	$n_{\text{series},2L}$	V_{cc} (kV)	$n_{\text{series},3L}$	V_{cc} (kV)
6.5	4	3.13	2	3.13
4.5	6	2.08	3	2.08
3.3	8	1.56	4	1.56

Table A.12: IGBT modules series-connection and device voltage for $N = 16$ segments.

V_{CES} (kV)	$n_{\text{series},2L}$	V_{cc} (kV)	$n_{\text{series},3L}$	V_{cc} (kV)
6.5	2	3.13	1	3.13
4.5	3	2.08	2	1.56
3.3	4	1.56	2	1.56

A.3.2 Total losses and system efficiency with 16 segments

Table ?? show the resulting converter system efficiency when having 16 segments ($N = 16$). This results was left out of chapter 5.2. Justification to the exclusion are given in the same chapter.

Table A.13: Resulting efficiency with 16 segments.

IGBT module	$f_{\text{sw}}=0.5$ kHz	$f_{\text{sw}}=1.0$ kHz	$f_{\text{sw}}=1.5$ kHz	$f_{\text{sw}}=2.0$ kHz
6.5 kV	99.5 %	99.1 %	98.8 %	98.5 %
4.5 kV	99.3 %	99.1 %	98.8 %	98.5 %
3.3 kV	99.5 %	99.3 %	99.1 %	98.9 %

A.4 Chapter 5

A.4.1 Simulation setup

Table A.14: Wind turbine model parameters.

Parameter	Value	Unit
Nominal mechanical output power	2.5	MW
Base power of the electrical generator	2.5	MW
Base wind speed	12	m/s
Maximum power at base wind speed	1	pu
Base rotational speed (p.u. of base generator speed)	1	pu
Cut-in wind speed	3	m/s
Rated wind speed	12	m/s

Table A.15: Generator segment parameters.

Symbol	Parameter	Value	Unit
r_s	Stator resistance	0.02	pu
x_s	Synchronous reactance ($x_s=I_s$ in pu)	0.33	pu
V_{ll}	Nominal line-to-line voltage	6.6	kV
I_{nom}	Nominal AC-side current (RMS)	110	A
Ω_r	Nominal angular frequency	188.3	rad/s
f_r	Nominal frequency	30	Hz
P_p	Number of pole pairs	77	
Ψ_m	Magnet flux linkage	28.44	Wb
k_t	Torque constant (each segment)	3253	Nm/Apeak

Table A.16: Converter parameters.

Symbol	Parameter	Value	Unit
C	DC-bus capacitance	1.0	mF
f_{sw}	Switching frequency	1.0	kHz
	Device on-state resistance	1.0	m Ω
	Snubber resistance	1.0	M Ω
	Snubber capacitance	inf	F
	Model Type	Switching device	

Table A.17: HVDC grid parameters.

Symbol	Parameter	Value	Unit
V_{dc}	Onshore converter station stiff DC-source	25	kV
R	Transmission cable resistance	1.0	Ω

Table A.18: Mechanical time constant.

Symbol	Parameter	Value	Unit
T_m	Mechanical time constant	6	s

Table A.19: Simulation and solver parameters.

Symbol	Parameter	Value	Unit
	Simulation type	Discrete	
T_s	Sample time	25	μs
	Discrete solver	Tustin/Backward Euler	

Table A.20: Expected voltages for various wind speeds with $psi_1 = 1.05$ and $psi_2 = 0.95$.

V_w	$V_{dc,1}$	$V_{dc,2}$
3	1.054	0.946
4	1.053	0.947
5	1.053	0.947
6	1.052	0.948
7	1.052	0.948
8	1.052	0.948
9	1.051	0.949
10	1.051	0.949
11	1.051	0.949
12	1.051	0.949

A.4.2 Simulation model

This Simulink simulation model for calculating semiconductor losses in various converters are inspired by [62]. The model is implemented for both a 2L-VSC and 3L-NPC converter in a ModHVDC application as presented in chapter 5.1. The simulation model implements an IGBT module with a loss calculation model and associated thermal model. This module is implemented for the minimum required number of devices. This is T1D1, T2D2 and D5 in the 3L-NPC converter and T1D1 in the 2L-VSC. References corresponds to what is given in Figure 2.5 and 2.2. Figure A.16 show the model implemented in phase-leg A of a 3L-NPC converter.

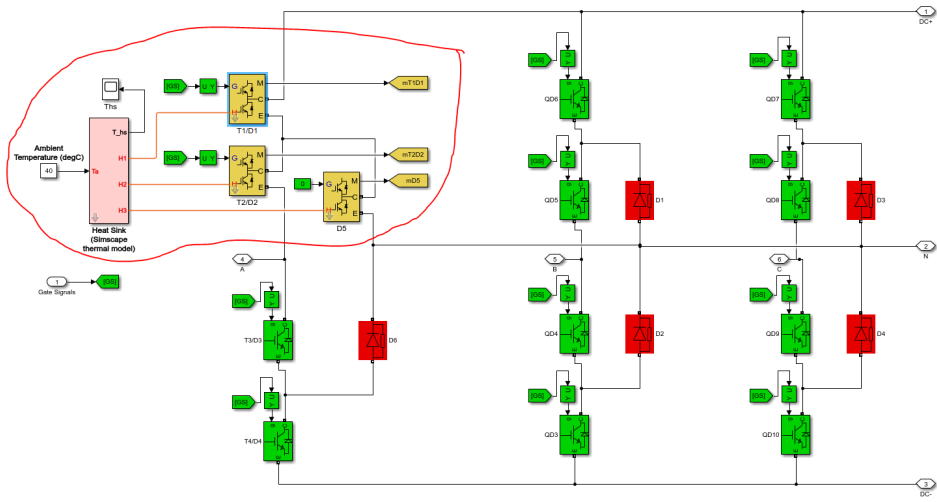


Figure A.16: Simulation model implemented in phase-leg A of a 3L-NPC converter.

Inside the golden colored half-bridge IGBT modules seen in Figure A.16, the loss calculation unit is found. The unit receives input data from the measurement port of Simulink's IGBT/diode [63] model. This is illustrated in Figure A.17. As seen, the equivalent module seen in Figure A.16 consist internally of two modules, which again internally consist of two equivalent IGBTs, as it is a half-bridge configuration. As seen, only one module (Module 2) IGBT and diode V/I measurements are used as input to the loss calculation unit. The outputs are switching and conduction losses of a single IGBT and diode (e.g. $P_{sw}(T1\&T4)$ and $P_{sw}(D1\&D4)$) in addition to the total heat development within Module 2. Adequate measures are taken to compensate for reduced number of measurements.

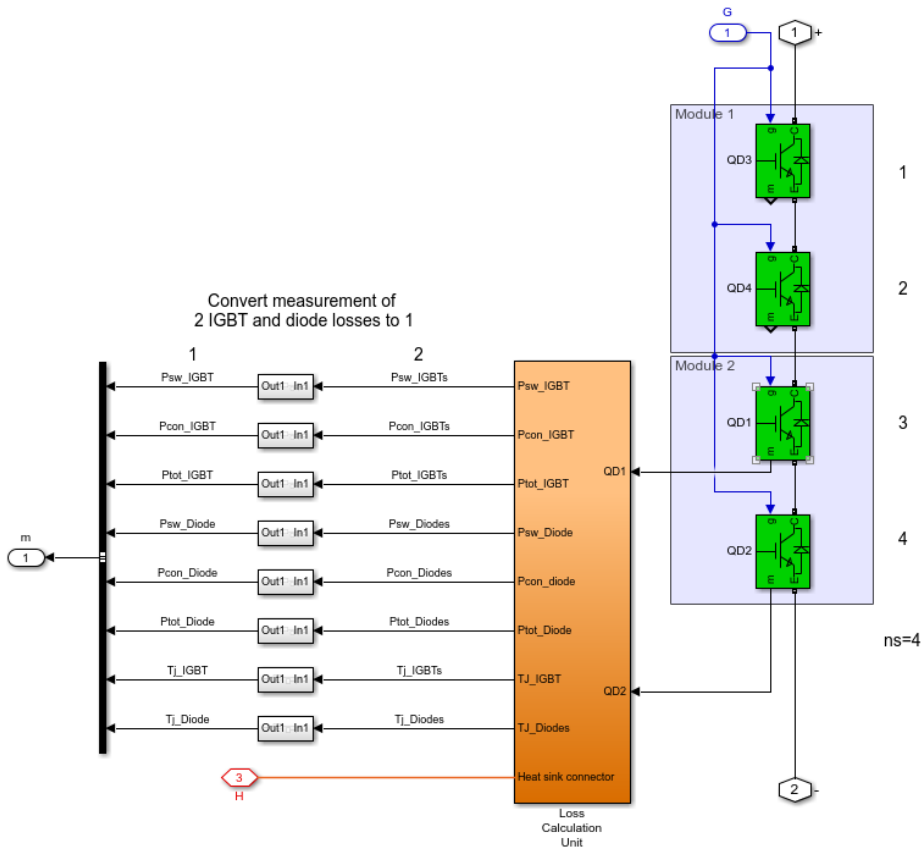


Figure A.17: IGBT module-model block content.

The loss calculation unit consist internally of a signal demux block for separating IGBT and diode measurement signals, a loss calculation for the IGBT and diode within the module and the modules thermal models. The thermal models are separated into a junction-case thermal model and case-heat sink model. Figure A.18 presents the loss calculation unit.

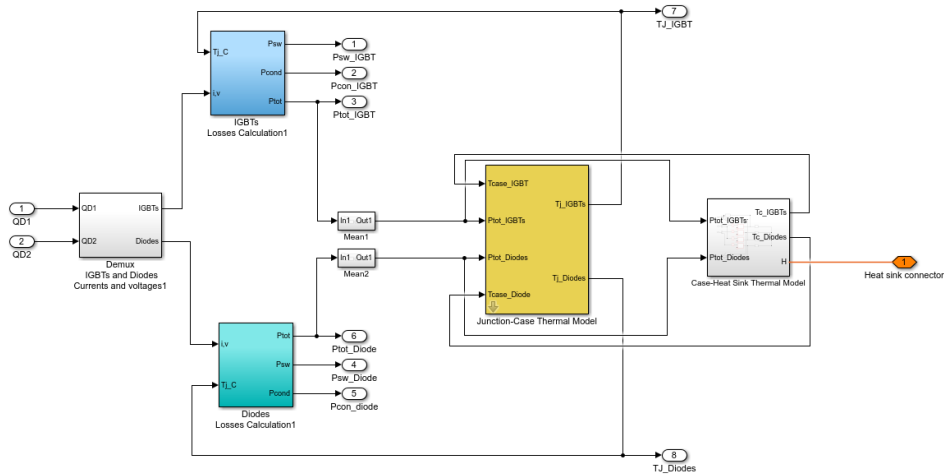
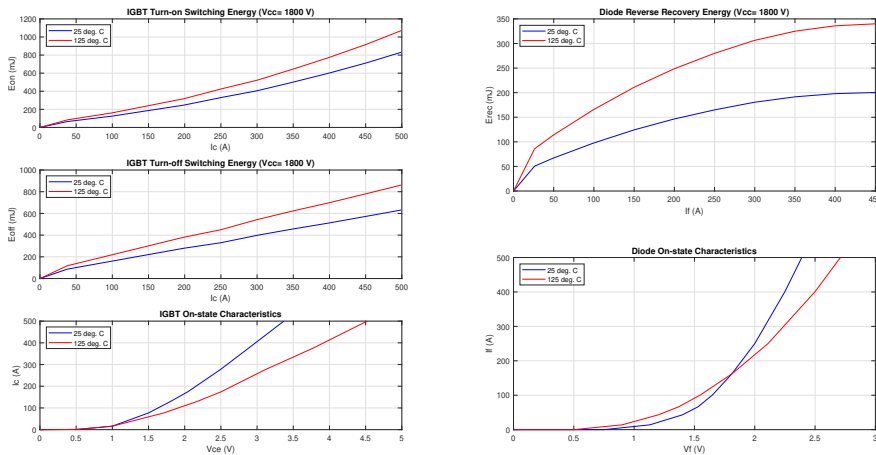


Figure A.18: Internal content of the loss calculation unit.

IGBT and diode loss calculation blocks uses look-up tables for calculating the switching, conduction and total losses of the respective device. Dynamic input values to these tables are junction temperature, device current and device voltage. The lookup inter- and extrapolation method are both linear methods. Static input values to the tables are IGBT and diode switching and forward characteristic for 25 and 125 °C junction temperatures. Figure A.19 illustrate the static input values to the tables.



(a) IGBT switching and forward characteristic.

(b) Diode switching and forward characteristic.

Figure A.19: Semiconductor junction temperatures for both converters.

Time-dependant total losses are then transformed to its mean value and used as input

to the thermal models. This is a simplification, but lowers simulation time, especially with a large heat sink, as steady state are reached much faster. By implementing this mean-value analysis, the IGBT and diode thermal resistance can be used instead of their thermal impedance [40]. Figure A.20 show the thermal equivalent circuit that is the basis for the thermal model. The model is inspired by [46, Fig. 27], where diode and IGBT junction-case thermal resistance have separated paths and no cross-talk. Numerical values to thermal resistances are found in IGBT module [50] and heat sink data sheet [64].

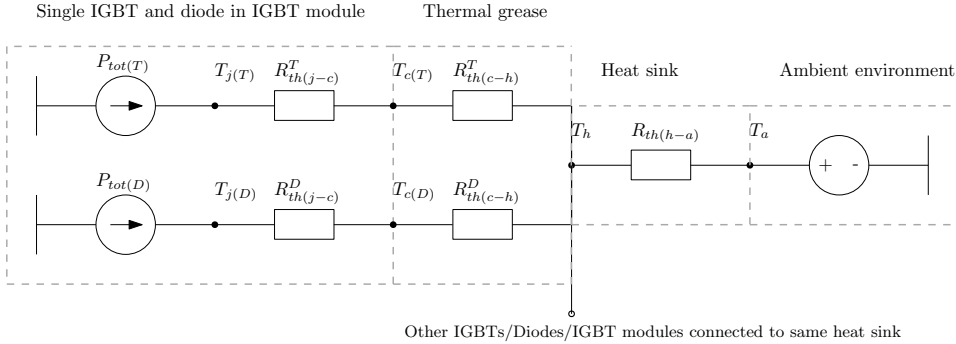


Figure A.20: Thermal equivalent circuit.

The junction-case and case-heat sink thermal model block content is presented in Figure A.21. As the connections indicates, there is an iterative calculation process concerning device temperatures and losses.

The heat sink block is shown in Figure A.22. All modules in one phase-leg share a common heat sink, where the heat sink is modelled as a pure resistor. Ambient temperature is set to 40 °C as shown in Figure A.16.

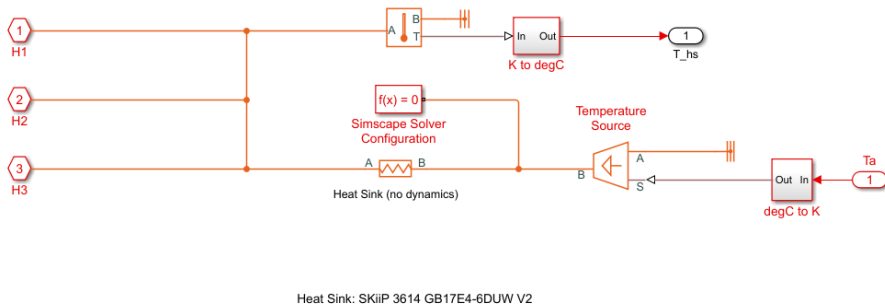
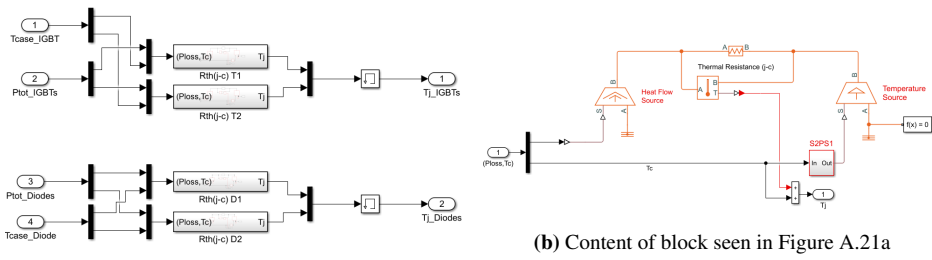
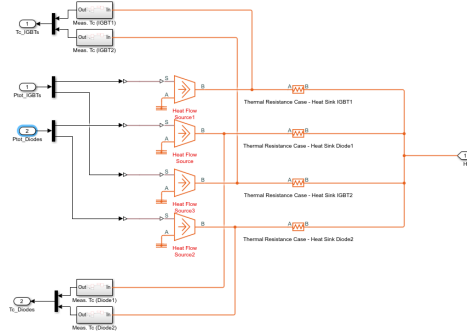


Figure A.22: Heat sink block.

Finally, and recapturing back to Figure A.16, the measurement ports are observed by scopes as seen in Figure A.23.



(a) Junction-case thermal model block.



(c) Case-heat sink thermal model.

Figure A.21: Semiconductor junction temperatures for both converters.

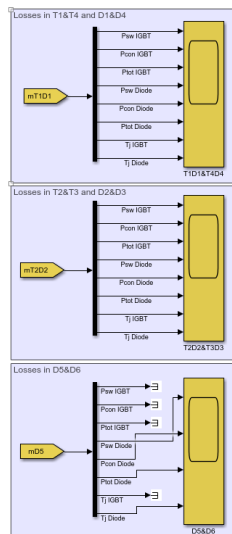


Figure A.23: Heat sink block.

A.4.3 Comparison of analytical and simulation model results

The following sub-chapters are dedicated to comparing losses when using the analytical model presented in chapter 4.2.7 and the simulation model in chapter A.4.2. The comparison are limited to nominal operation, i.e. wind speed at 12 m/s and the switching frequency is 1.0 kHz. Junction temperatures are found in chapter 5.2.4. An eight-segment configuration are assumed. When calculating total losses and efficiency, the all these eight segments are accounted for, as in the analytical model.

Reference components

Comparison is conducted with ABB HiPak IGBT Module 5SNG 0250P330300. The device model is used for all IGBTs and diode in both converters. Required input data to the analytical model are found in Table A.21.

Table A.21: IGBT module 5SNG 0250P330300 input data to analytical model.

Manufacturer	ABB
Model	5SNG 0250P330300
V_{CES} (kV)	3.3
I_c (A)	250
Module type	Half-bridge
I_{ref} (A)	250
V_{ref} (kV)	1.8
T_{ref} (°C)	125
E_{sw} (J)	0.875
E_{rr} (J)	0.28
R_{CE} 25 °C (Ω)	0.0061
R_{CE} 125 °C (Ω)	0.0082
V_{CE0} 25 °C (V)	0.9900
V_{CE0} 125 °C (V)	1.13
R_F 25 °C (Ω)	0.0033
R_F 125 °C (Ω)	0.0050
V_{F0} 25 °C (V)	1.27
V_{F0} 125 °C (V)	1.06

2L-VSC

The results show that the analytical model presents lower switching losses than the simulation model. The conduction losses are as good as equal. The resulting deviation in switching losses leads to a difference in 7.3 kW in total losses, which again leads to a difference in efficiency. The accumulated error seen in total losses are limited to roughly 7 % and is acceptable.

Table A.22: Comparison of switching and conduction losses with the analytical and simulation model when using a 2L-VSC.

Model	$P_{sw(T)}$	$P_{con(T)}$	$P_{sw(D)}$	$P_{con(D)}$
Analytical	133	15	49	69
Simulation	147	15	55	68
Deviation	14	0	7	-1

Table A.23: Comparison of total losses and efficiency with the analytical and simulation model when using a 2L-VSC.

Model	P_{tot} (kW)	η
Analytical	102.1	99.0 %
Simulation	109.4	98.9 %
Deviation	7.3	-0.1 %

3L-NPC

The results for the 3L-NPC converter coincides with the 2L-VSC as the switching losses show highest deviation. The largest error is IGBT T2 and T3 switching losses. However, as seen in chapter 4, conduction losses takes up a greater share of total losses in a 3L-NPC converter compared to a 2L-VSC. Therefor the deviation in total losses are reduced with this converter as conduction losses have close to no error.

Table A.24: Comparison of switching losses with the analytical and simulation model when using a 3L-NPC converter.

Model	$P_{sw(T1\&T4)}$	$P_{sw(T2\&T3)}$	$P_{sw(D1\&D4)}$	$P_{sw(T2\&T3)}$	$P_{sw(D5\&D6)}$
Analytical	3	126	43	1	1
Simulation	5	138	51	0	2
Deviation	2	12	8	-1	1

Table A.25: Comparison of conduction losses with the analytical and simulation model when using a 3L-NPC converter.

Model	$P_{con(T1\&T4)}$	$P_{con(T2\&T3)}$	$P_{con(D1\&D4)}$	$P_{con(T2\&T3)}$	$P_{con(D5\&D6)}$
Analytical	0	31	56	56	27
Simulation	0	30	56	56	27
Deviation	0	-1	-1	0	0

Table A.26: Comparison of total losses and efficiency with the analytical and simulation model when using a 3L-NPC converter.

Model	P_{tot} (kW)	η
Analytical	65.9	99.3 %
Simulation	69.8	99.3 %
Deviation	3.8	0.0 %

A.4.4 Results

Table A.27 show the input data for calculating the average efficiency of the 2L-VSC and 3L-NPC.

Table A.27: Data input for calculation of average efficiency.

Vw	2L-VSC	3L-NPC	f(Vw)	Pin
3	94.4 %	97.3 %	4.4 %	0.016
4	96.0 %	97.9 %	5.5 %	0.037
5	96.9 %	98.3 %	6.4 %	0.072
6	97.5 %	98.6 %	7.1 %	0.125
7	97.9 %	98.8 %	7.5 %	0.198
8	98.2 %	98.9 %	7.6 %	0.296
9	98.5 %	99.1 %	7.5 %	0.422
10	98.7 %	99.2 %	7.2 %	0.579
11	98.8 %	99.2 %	6.7 %	0.770
12	98.9 %	99.3 %	6.1 %	1.000
13	98.9 %	99.3 %	5.4 %	1.000
14	98.9 %	99.3 %	4.7 %	1.000
15	98.9 %	99.3 %	4.0 %	1.000
16	98.9 %	99.3 %	3.4 %	1.000
17	98.9 %	99.3 %	2.8 %	1.000
18	98.9 %	99.3 %	2.2 %	1.000
19	98.9 %	99.3 %	1.8 %	1.000
20	98.9 %	99.3 %	1.4 %	1.000
21	98.9 %	99.3 %	1.0 %	1.000
22	98.9 %	99.3 %	0.8 %	1.000
23	98.9 %	99.3 %	0.6 %	1.000
24	98.9 %	99.3 %	0.4 %	1.000

